Chair of Turbomachinery and Flight Propulsion
Department of Aerospace and Geodesy
Technical University of Munich

Mechanical Predesign of High Performant Heat Exchangers in Novel Aero Engines

Professor: Univ.-Prof. Dr.-Ing. Volker Gümmer
Chair of Turbomachinery and Flight Propulsion

Supervised by: Patrick Bachmann, M.Sc
Chair of Turbomachinery and Flight Propulsion

Author: Philipp Koch
Boltzmannstraße 15
85748 Garching b. München

Date: 30. November 2024

Master Thesis
30. November 2024

Abstract

Keywords: Heat Exchanger, Aero Engine, Gas Turbine, Structural-Mechanics, Predesign, Failure Modes

The usage of heat exchangers in aero engines can contribute to a higher fuel efficiency and a lower climate impact. While the thermo- and fluid dynamics of heat exchangers have been extensively studied, there is a lack of comprehensive structural-mechanic assessment methods for these components. This thesis aims to close this gap by deriving simplified methods applicable in the preliminary design process to assess the most important failure modes of two heat exchanger types, the Plate-Fin Heat Exchanger and the Tube Bundle Heat Exchanger. The plausibility of the results created with these methods is assessed.

The methods applied to the Tube Bundle Heat Exchanger yield a satisfactory overall structural-mechanic assessment. The methods employed for the Plate-Fin Heat Exchanger can, in general, assess its structural integrity. However, the influence of thermal stresses can not be evaluated satisfactorily.

The influence of operational and geometrical parameters on the failure modes has been investigated. Corrosion leads to significant required augmentation in the heat exchangers' mass and hence has to be avoided to keep the component reasonably lightweight. The design driving failure modes for both types of heat exchangers depend on the operational conditions. To enhance structural integrity in a mass-efficient manner, it is recommended to increase the plate and tube thickness for each respective heat exchanger type. However, after reaching a certain plate thickness, the stresses of the Plate-Fin Heat Exchanger increase with increasing plate thickness due to the thermal stresses dominating the pressure stresses.

The methods developed in this thesis can serve as a foundation for the structural-mechanic assessment of heat exchangers.

Kurzfassung

Schlüsselwörter: Wärmetauscher, Flugantrieb, Gasturbine, Strukturmechanik, Vorauslegung, Schadensmechanismus

Der Einsatz von Wärmetauschern in Flugantrieben kann zu einer verbesserten Brennstoffeffizienz und einer geringeren Klimabelastung beitragen. Die thermo- und fluiddynamischen Eigenschaften von Wärmetauschern wurden bereits ausgiebig untersucht. Es fehlt jedoch an umfassenden strukturmechanischen Bewertungsmethoden für derartige Komponenten. Die vorliegende Arbeit soll diese Lücke schließen, indem vereinfachte, im Vorauslegungsprozess anwendbare Methoden zur Bewertung der wichtigsten Versagensarten von zwei Wärmetauschertypen, dem Lamellenwärmetauscher und dem Rohrbündelwärmetauscher, abgeleitet werden. Die mit diesen Methoden erzielten Ergebnisse werden auf ihre Plausibilität hin überprüft.

Die für den Rohrbündelwärmetauscher angewandten Methoden ermöglichen eine präzise strukturmechanische Gesamtbewertung. Die für den Lamellenwärmetauscher angewandten Methoden können grundsätzlich zur Bewertung der strukturellen Integrität genutzt werden. Thermalspannungen können jedoch nicht mit ausreichender Genauigkeit bewertet werden.

Zusätzlich wurde der Einfluss von Geometrie- und Betriebsparametern auf die Schadensmechanismen untersucht. Korrosion führt zu einer erheblichen Erhöhung der Masse des Wärmetauschers und muss daher vermieden werden, um das Bauteil möglichst leicht zu halten. Die für die Konstruktion maßgeblichen Versagensarten hängen bei beiden Arten von Wärmetauschern von den Betriebsbedingungen ab. Um die strukturelle Integrität auf masseneffiziente Weise zu verbessern, wird grundsätzlich empfohlen, die Platten- und Rohrdicke für den jeweiligen Wärmetauschertyp zu erhöhen. Ab einer bestimmten Plattendicke allerdings steigen die Spannungen im Lamellenwärmetauscher mit zunehmender Plattendicke wieder. Die thermischen Spannungen nehmen in diesem Fall stärker zu als die Druckspannungen sich durch die zusätzliche Dicke reduzieren.

Die in dieser Arbeit entwickelten Methoden können als Grundlage für die strukturmechanische Bewertung von Wärmetauschern dienen.

Declaration of Authorship

I hereby declare that this thesis is my own work prepared without the help of a third party. No other than the listed literature and resources have been used. All sources transferred literally or analogously to this work have been labeled accordingly.

Additionally, I hereby certify that this thesis has not been underlain in any other examination procedure up to the present.

Garching bei München, 30. November 2024

Acknowledgments

I would like to express my deepest appreciation to my supervisors at MTU, Samuel Fuhrmann and Dr. Marvin Nahrmann, for their unwavering support and invaluable suggestions. Without you, this thesis would not have been possible. Your expertise and willingness to help have truly made a difference. I would like to extend my sincere gratitude to Patrick Bachmann for his support and guidance on the structure of this thesis. His expertise and constructive advice have been instrumental in shaping the writing process. I would also like to express my gratitude to my colleagues at MTU for their contributions to the success of this thesis. Your quick responses, estimations, and guidance have been invaluable throughout this journey.

Ultimately, I want to extend my heartfelt appreciation to my family and my girlfriend. Your unwavering support, encouragement, and belief in my work have been a constant source of motivation. Your understanding during the long hours spent studying and working on this thesis has meant the world to me. I am truly fortunate to have such a loving and supportive network.

List of Symbols

Latin Symbols

a	[m]	Larger Dimension used for Bending Calculation
b	[m]	Smaller Dimension used for Bending Calculation
c	[m]	Corrosion Allowance
$\mathrm{CO_2}$	[-]	Carbon Dioxide
CR	[mm/y]	Corrosion Rate in mm per year
d	[m]	Diameter
D	[-]	Damage
E	[Pa]	E-Modulus (Young's Modulus of Elasticity)
f	[Pa]	Acting Stress
f_d	[Pa]	Design Condition
f_{nc}	[Pa]	Allowable Stress
F	[N]	Force
FD	[1/m]	Fin Density
g	[m/s^2]	Gravitational Acceleration
h	[m]	Height
$\mathrm{H_2}$	[-]	Hydrogen
I	[m^4]	Area Moment of Inertia
K	[-]	Buckling Coefficient
k_h	[-]	Form Factor
k_i	[-]	Stress Intensification Factor
k_T	[-]	Temperature Correction Factor
k_z	[-]	Welding Factor
$\mathrm{K_2SO_4}$	[-]	Potassium Sulfate
l	[m]	Length
LMP	[-]	Larson-Miller Parameter
LT	[h]	Lifetime (in hours)

MCA	[mg/cm^2]	Corrosive Mass
n	[-]	Number of
N	[-]	Allowable Number of Cycles
Na_2SO_4	[-]	Sodium Sulfate
NO_x	[-]	Nitrogen Oxide
p	[Pa]	Pressure
q_{load}	[Pa]	Uniformly Distributed Load
r	[m]	Radius
R	[-]	Stress Ratio in Cyclic Loading
$R_{m/T/t}$	[Pa]	Rupture Strength for given Temperature and Time
$R_{p,0.2}$	[Pa]	Yield Strength at 0.2 % Offset
$R_{p1,0/T/t}$	[Pa]	Yield Strength at 1 % Offset for given Temp. and Time
S_e	[Pa]	Stress at Endurance Limit
SL	[m]	Vertical Distance between Adjacent Tubes
ST	[m]	Horizontal Distance between Adjacent Tubes
SO_x	[-]	Sulfur Oxide
t	[m]	Thickness
T	[K]	Temperature
V_2O_5	[-]	Vanadium Oxide
w	[m]	Width
y	[m]	Displacement

Greek Symbols

α	[m/(m·K)]	Coefficient of Thermal Expansion
δ	[-]	Displacement
Δ	[-]	Difference
ϵ	[-]	Strain
ν	[-]	Poisson's Ratio

ρ	[kg/m^3]	Density
σ	[Pa]	Stress

Abbreviations

FEM	Finite Element Method
FOD	Foreing Object Damage
FoS	Factor of Safety
GTF	Geared Turbofan
HCF	High-Cycle Fatigue
HX	Heat Exchanger
ICAO	International Civil Aviation Organization
LCF	Low-Cycle Fatigue
MCL	Maximum Climb
MTO	Maximum Take-Off
MTU	MTU Aero Engines AG
NPSS	Numerical Propulsion System Simulation
PFHE	Plate-Fin Heat Exchanger
SCC	Stress Corrosion Cracking
SFC	Specific Fuel Consumption
TBHE	Tube Bundle Heat Exchanger
UTS	Ultimate Tensile Stress
WET	Water-Enhanced Turbofan

Subscripts

a	Amplitude
A	Area
bends	Bends of Tube in TBHE
c	Creep
cr	Critical Buckling
cycles	Occurring Cycles
f	Fatigue
fin	Fins of one Passage of PFHE
fins	All Fins of PFHE
ft	Fin of TBHE
i	Index for Flow
inner	Inner
j	Index for Load Condition
m	Mean
mt	Melting Point
outer	Outer
p	Tube Passages in TBHE
passages	Flow Passages in PFHE
plate	Plate
pressure	Pressure
r	Radial Direction
sidebar	Sidebar
subst.	Substitute
t	Tube
θ	Circumferential Direction
tubes	All Tubes of a TBHE
weight	Weight

Contents

List of Figures

List of Tables

1 Introduction

1.1 Motivation

In recent years, enabling sustainable aviation has become more and more important to politics and society. Multiple governing bodies have developed ambitious plans to adhere to the 1.5 °C target defined by the Paris Agreement. The International Civil Aviation Organization (ICAO) aims to reach net-zero CO_2 emissions from global aviation by 2050 [16]. Other heat-trapping gases like nitrogen oxide or methane contribute to the warming as well. While they may not be as abundant in the atmosphere as CO_2 is, they can trap more heat. Further phenomena, like high-altitude ice-cirrus clouds, known as contrails, can lead to reflections and can therefore trap heat as well. These non-CO_2 emissions contribute to the global warming. While those emissions are not as well understood, they have received more attention from politics recently, emphasizing their significance [17].

The aviation industry aims to decrease fuel burn, which is proportional to emitted CO_2, by 2.1 % per year [18]. However, due to increasing globalization, especially in emerging countries, air traffic around the world is expected to grow by 4.3 % per year [19], leading to an increase in fuel burn, and hence CO_2 emissions of 2.2 % per year. While evolutionary technologies may still offer improvements in specific fuel consumption, these benefits are gradually more expensive to achieve over time as the technologies become more optimized. Therefore, new revolutionary concepts enabling a step change in fuel efficiency are required.

One of the proposed concepts is the Water-Enhanced Turbofan (WET) concept. It utilizes the Cheng cycle, which is a combination of the conventional Joule-Brayton cycle with a Clausius-Rankine cycle. In general, its components and general setup are comparable to the Geared Turbofan (GTF). However, steam is injected into the combustion chamber and later recovered from the exhaust gas. This new engine concept promises significant reductions in NO_x and soot particle emissions, as well as the formation of contrails. A vaporizer provides the required superheated steam, which is generated using heat contained in the exhaust gas. To avoid the need for large water tanks, as much water as possible needs to be extracted from the exhaust gas mixture using a condenser. Both vaporizer and condenser are high-performant two phase heat exchangers.

Heat exchangers (HXs) are widely used in different applications. However, the implementation of HXs in large civil aircraft applications is yet to be investigated. To ensure safe flight, the structural integrity of the HXs needs to be guaranteed in all flight states and over the complete engine lifetime. With high temperature and pressure gradients as well as rough ambient conditions and phase changes from water to steam (and back), the HXs face significant structural challenges.

The development process in the aerospace industry typically follows different design stages. The most important ones are the conceptual design, preliminary design, and the detailed design phase. The conceptual design process involves the creation of new engine concepts. During the preliminary design stage, the concepts are investigated more thoroughly. It is then further developed during the detailed design stage. The preliminary design stage, involving the investigation of the concept by simple methods, is especially important. During and especially after this phase, changes to the design are significantly more costly and the design freedom in general reduces. Therefore, a proper assessment of the component during the preliminary design is inevitable.

To properly assess different technologies and ease integration into the engine, an accurate prediction of geometry and mass is required during the preliminary design stages. Vaporizing great amounts of steam and condensing equally great amounts of water is only possible by using a large heat transfer area leading to large HXs. Therefore, both vaporizer and condenser significantly influence the WET concept's geometry and mass. Being one of the geometry and mass-defining components of the WET concept and highly stressed at the same time emphasizes the need for suitable structural-mechanic predesign methods.

1.2 Goals

The goal of this thesis is to derive methods for the structural-mechanic predesign of both vaporizer and condenser. Both the Plate-Fin Heat Exchanger (PFHE) and the Tube Bundle Heat Exchanger (TBHE) are investigated. First, possible failure modes of each heat exchanger type are collected and assessed according to their impact on mass and geometry as well as to their severity in case of failure. Then, the design driving failure modes are derived. For each of these failure modes, appropriate methods for their structural-mechanic assessment are derived. All methods need to provide adequate accuracy while featuring a low computation time. The derived methods will be implemented in Numerical Propulsion System Simulation (NPSS). The plausibility of the derived methods is checked, and the sensitivity of the methods to uncertainties is investigated. Ultimately, design studies on the impact of changes in the geometric properties of the heat exchangers are conducted.

2 Introduction to Heat Exchangers in Aero Engines and Occurring Failure Modes

In this chapter, a brief overview of the usage of heat exchangers in gas turbines is presented first. Then, Section 2.2 presents the WET concept, one example of using a heat exchanger in an aero engine. It involves the utilization of a PFHE and a TBHE. Both HXs will be explained in Sections 2.3.1 and 2.3.2.

2.1 Heat Exchangers in Aero Engines

Using heat exchangers in the engine cycle itself allows recuperating heat energy from the exhaust gas and can, therefore, lead to decreases in SFC [6]. However, while the recuperation of heat in the exhaust gas promises a reduction in SFC, NO_x and noise emissions, the constructive effort required for the design and integration of heat exchangers is significant [20]. Therefore, to the author's knowledge, no existing aero engine features heat exchangers integrated in the engine cycle. Currently, heat exchangers in aero engines are commonly used outside of the actual engine cycle, e.g., for cooling oil or air. However, heat exchangers play an important role in multiple revolutionary engine concepts. Examples are the flying fuel cell and the WET concept. The WET concept is used as use case in this thesis; the findings and methods can be applied to other engine concepts as well.

2.2 Water-Enhanced Turbofan (WET) Concept

The WET concept, shown schematically in Figure 2.1, is a gas turbine cycle concept involving the injection of steam into the combustion chamber. The concept of steam injection into gas turbines has been investigated since the 1950s. It has been mainly used in stationary gas turbines [21, 22] or as a mean for short thrust augmentation in aircraft without recovering the water [23]. The concept of injecting steam and subsequently recovering the water in a flying aero engine was first introduced by

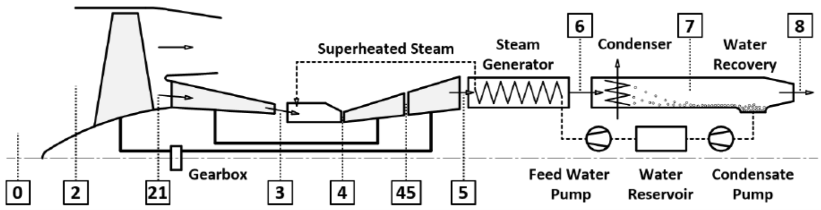

Figure 2.1: Schematic process and involved components of WET concept, from [1].

[1] in a concept now known as WET concept. It utilizes the Cheng cycle, which is a combination of the Joule-Brayton cycle, currently used in aero engines, with a Clausius-Rankine cycle involving water as working fluid. Steam is generated using the heat from the exhaust gas and then injected into the combustion chamber. This increases the specific heat capacity and the mass flow rate of the gas mixture and hence leads to a more efficient thermodynamic cycle. As carrying a large water tank leads to additional weight and integration challenges, the required water needs to be recovered from the exhaust gas mixture, leading to a quasi-closed circle. The WET concept is expected to reduce the SFC, NO_x emissions by 90 % and the radiative forcing by contrail cirrus by 50 %, leading to a substantial reduction of overall climate impact. [1, 24, 25, 26] The WET concept has been further investigated in [27, 28], estimating the weight of the propulsion system to be significantly higher due to the integration of the heat exchangers. While the components of the aero engine, excluding the components for heat recovery, are estimated to be 15 % lighter, the additional components for exchanging the heat and recovering the water are expected to increase the overall propulsion system weight by 40 % compared to a conventional propulsion system [1]. The large influence on overall mass shows the importance of proper HX predesign.

2.3 Introduction to Selected Heat Exchanger Types

2.3.1 Plate-Fin Heat Exchanger

The PFHE is similar to a plate HX. However, fins are added to extend the surface of the heat exchanger. Fins increase the surface area significantly and hence allow for a compact HX able to exchange significant amounts of heat. Figure 2.2a shows one passage, while Figure 2.2b shows the setup of a cross-flow PFHE. Side bars

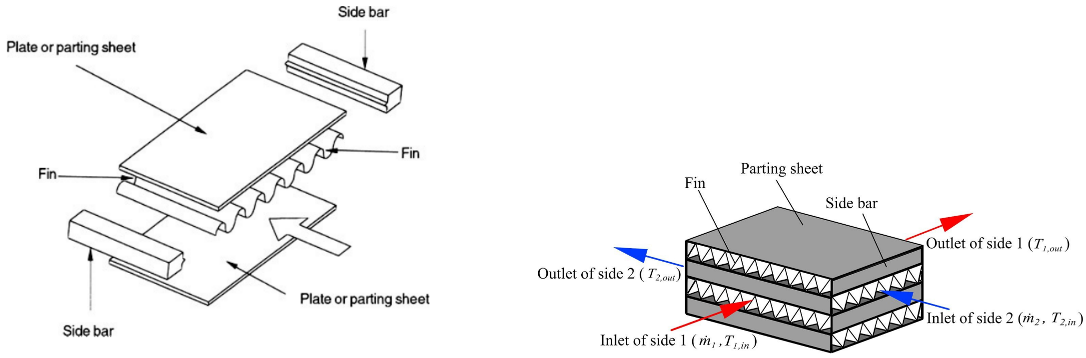

a) Components of a PFHE, from [2]   b) Setup of a cross-flow PFHE, from [29]

Figure 2.2: Characteristic setup of PFHE

and upper and lower plates bound the flow of the medium. The fins are enclosed between both plates. They serve the main purpose of increasing the heat transfer area. However, they can enhance the structural strength and rigidity of the structure as well. The fins are typically die-formed or roll-formed. They are attached to the plates, using, e.g., brazing, soldering, or welding. Common design parameters include the fin thickness, fin height, and the fin density, which is the number of fins per unit length. A higher fin density leads to a higher surface area density. PFHE are used since the 1910s in cars and since the 1940s in aircraft.

2.3.2 Tube Bundle Heat Exchanger

TBHE are similar to shell-and-tube HX, however, no shell is present. A tube bundle, consisting of multiple tubes, facilitates the first medium. The second medium flows around the tubes. Their configuration can be closed (shelled) or open. An example is shown in Figure 2.3. This type of HX offers considerable design flexibility, featuring different tube arrangements and varying shell diameters and lengths. Its layout can be adjusted to operate with different types of fluids and in different applications. Furthermore, it's robust and reliable. TBHE are especially suitable for very high operating temperatures and pressures. Their heat transfer area can be enhanced by using fins on the inside or outside of the tube. [2]

As shown in Figure 2.4, the fins can either be attached to the tubes without a connection between all plates (a) or as continuous plates connecting the tubes together (b). The fins can feature different shapes including plain, wavy or serrated

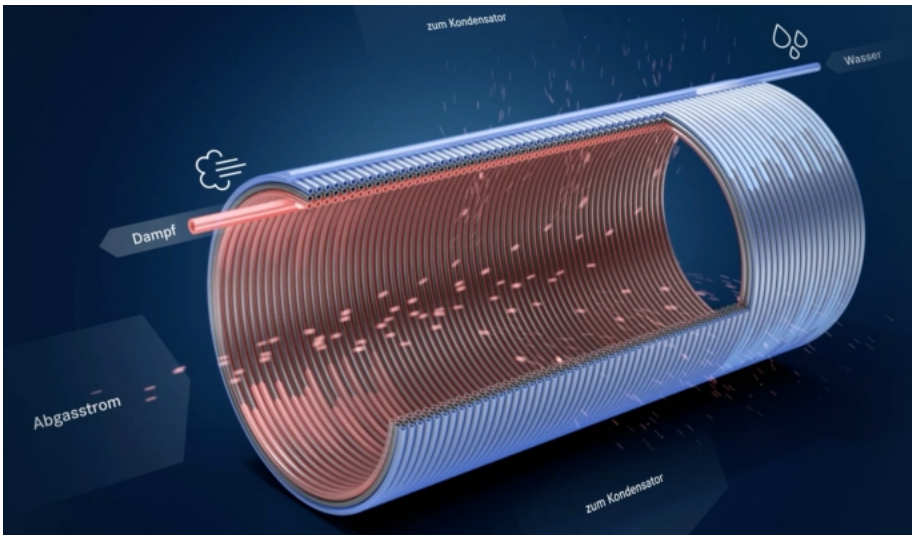

Figure 2.3: Example of tube bundle heat exchanger ©MTU Aero Engines AG

shapes can be used. They are mostly applied in cases where the outside flow has a lower heat transfer coefficient than the flow inside the tube (e.g. in the example of exhaust gas as outside flow and liquid water as inside flow). To balance the thermal conductance, the surface area is increased using fins.

2.4 Failure Modes

The sections above gave a brief overview of two different heat exchanger types and the WET concept as one exemplary use case of large heat exchangers. A structural

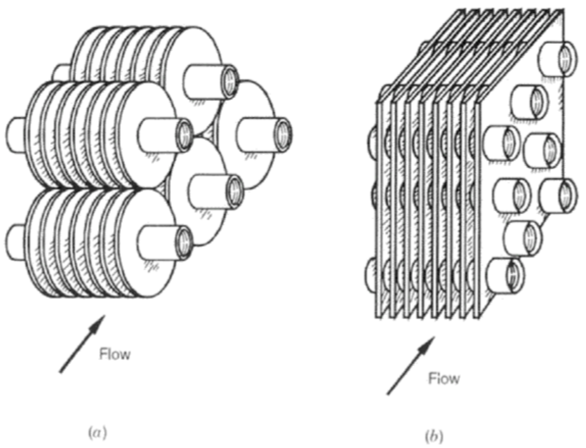

Figure 2.4: Different types of tube-fin HXs with (a) individually finned tubes and (b) continuous fins, from [2]

assessment of the heat exchangers is required to ensure their integrity over the whole lifetime. A method commonly used during the design process in the aerospace industry is the failure mode and effects analysis. It involves the derivation of the consequences resulting from a specific item or function failing. A complete failure mode and effects analysis is beyond the scope of this thesis. However, its first step, which is the collection of the possible failure modes, provides a good overview for the structural assessment. To ensure structural integrity all failure modes have to be covered by adequate assessment methods and/or constructive measures to avoid them. [30]

The most commonly occurring failure modes of mechanical components include corrosion, fracture, buckling, creep, fatigue as well as deformation [31, 32]. Deformation can be assessed in a similar way to fracture: instead of comparing the acting stress to the stress limit of the material leading to fracture, the acting stress can be compared to the stress limit leading to plastic deformation. It is, therefore, not specifically listed in this thesis but covered in Section 2.4.3.

Failure modes are typically a result of stressors. One can distinguish between different principal categories of stressors: Mechanical stresses are induced by applying a force either by solid contact or via hydrostatic pressure. These stresses can be either static, dynamic, or impact stresses, depending on the occurrence and magnitude of the resulting stress. Environmental factors, like present oxygen, moisture, or heat, can lead to stresses in the form of oxidative potential or elevated temperature. These environmentally-induced stresses can lead to corrosion, softening, or deformation. Furthermore, the interaction between environmental factors, like an elevated temperature, and mechanical stress can lead to creep. Finally, electromagnetic waves interact with the material through their radiation energies. [32]

All stressor categories can occur in an aircraft. However, their influence varies. In heat exchangers, no significant electromagnetic waves should occur. Therefore, this thesis focuses on mechanical stresses and environmental factors. Interactions between mechanical stresses and environmental factors are investigated as well, including thermo-mechanical loads.

2.4.1 Corrosion

Corrosion forms another important failure mode of materials. Material is wasted or degraded through chemical attack by environmental species. This can include water or oxygen as well as high temperatures. The latter is called high-temperature corrosion.

Corrosion is highly dependent on the environmental conditions. These include the temperature as well as the corrosive medium. Additionally, differences exist between cyclic, intermittent immersion in the environment, and continuous immersion. In general, especially in high temperature applications, cyclic testing should yield an increased corrosion rate due to the repetitive acting of thermal stresses. However, comparing two nickel-based alloys, a reduction of the corrosion rate in cyclic behavior compared to a continuous immersion was found. [33]

2.4.1.1 Relevance for Structural Design of Heat Exchangers

In PFHE, corrosion is one major failure mode, especially in the automotive and aerospace sectors, due to the occurring environmental conditions. It is dependent on the fluid parameters. High temperatures, low-pressure wet steam, and a high concentration of ions like sulfate, nitrate, chloride, oxygen, and iron enhance corrosion. Sudden changes in Reynolds number can increase the corrosion rate as well.

Corrosion is occurring often in TBHE as well. It can occur due to the intrusion of foreign materials, due to vibration, and due to uniform attack [34].

In general, one can distinguish seven types of corrosion. The first one, general corrosion, is characterized by a uniform attack over the whole component. Adequate material selection can prevent it. Pitting corrosion is another type of corrosion. A preexisting damage, e.g., a scratch or dirt, forms a pit. The resulting difference in oxygen concentration leads to an electrochemical potential in and outside of the pit. The resulting concentration cell corrodes the material inside the pit, increasing its size. Residual stresses from manufacturing can lead to a third type of corrosion, called stress corrosion. The introduced, fine cracks open the grain boundary, which then gets corrosively attacked. In stainless steel tubes, the corrodent is mostly chloride ions, while in copper tubes, ammonia acts as a corrodent. The phenomenon is commonly known as Stress Corrosion Cracking (SCC) Dezincification can occur at high temperatures and low pH values in alloys with more than 15 % zinc. The selective removal of zinc leads to a porous, copper-dominated material with less mechanical strength. Another corrosion type is galvanic corrosion. It occurs when dissimilar metals are joined in the presence of an electrolyte. An increase in the difference between the noble of a metal leads to an increased risk of galvanic corrosion. Secluded areas or dirt accumulation can lead to localized cells enhancing crevice corrosion. It leads to metal loss with local pits. Stagnant conditions are required for crevice corrosion to occur. Condensate grooving is described as the last type of corrosion. It occurs on the outside of steam-to-water HX tubes. Condensate runs along the outside of the tube, forming a groove. The wetted area forms a corrosion cell, especially if the condensate is aggressive. Controlling its pH value and regular cleaning of the tubes can prevent condensate grooving. [35, 36]

Additionally, vibration can cause fretting corrosion, which is corrosion resulting from damage to the protective film caused by chafing of adjacent parts. To prevent vibrations, the tube bundle should act as a single entity. Additional anti-vibration support can be used as well. [37]

Corrosion can be present in the entry region of the tubes at the inlet. This coincides with the location where the tubes are normally joined to the tube sheets. Internal and external corrosion can occur there. The joining of the tubes induces residual stresses, leading to circumferential SCC . Due to the tight fit, missing ventilation can lead to chloride buildup and, hence, crevice corrosion. [38]

The reduction of material thickness per time, called corrosion rate, is dependent on the temperature and on the material, as well as the environmental conditions. Typically, it is given in $\frac{\mathrm{mm}}{\mathrm{year}}$, indicating the reduction in thickness due to the corrosive medium per year.

2.4.1.2 Possible Constructive Measures and Assessment Methods

Industry norms, like [39], summarize constructive measures for unfired pressure vessels. Different forms of corrosion and erosion are concluded under one term: corrosion. A corrosion allowance defines the material added to the required net wall thickness to account for the reduction in wall thickness due to corrosion. However, corrosion allowance is no means to protect the component against SCC or pitting. These two forms of corrosion can be prevented by using well-suited materials, proper protective films, or appropriate manufacturing processes. Further protective measures include the usage of a corrosion allowance, which is an additional wall thickness, as well as the avoidance of sharp edges and dead spaces or the usage of special construction elements. The corrosion rate influences the heat transfer, dependent on the temperature gradient over the boundary layer near the wall. [40]

The amount of corrosion allowance is not well-defined in the literature. Some propose adding a lump-sum, like 1 mm, 2 mm, or 4 mm [41], 3 or 6 mm [42], between 0.3 mm and 3 mm [43] or 1.6 mm or 3.2 mm [44], dependent on the corrosiveness of the environment and the material itself. Others propose a corrosion allowance c based on the product of the corrosion rate per year CR and the expected lifetime in years LT [43, 45], as described in Equation 2.1.

$$c = CR * LT \tag{2.1}$$

However, adding a corrosion allowance is not recommended for plate HX, as typically the plates are much thinner than the tubes, and hence, the corrosion allowance would dominate the weight of the plate [46]. If possible, corrosion-resistant materials are recommended. However, if no corrosion-resistant materials with sufficient strength exist, a corrosion allowance can be used.

A different method can be used to estimate the corrosion lifetime of a protective layer. It relies on material data on the corrosive behavior of corrosion lifetime depending on the material temperature. An exemplary curve is shown in Figure 2.5. Using the data from this characteristic, the total corrosion lifetime of a mission covering different environmental conditions can be estimated by linear damage accumulation. [3, p. 8-11]

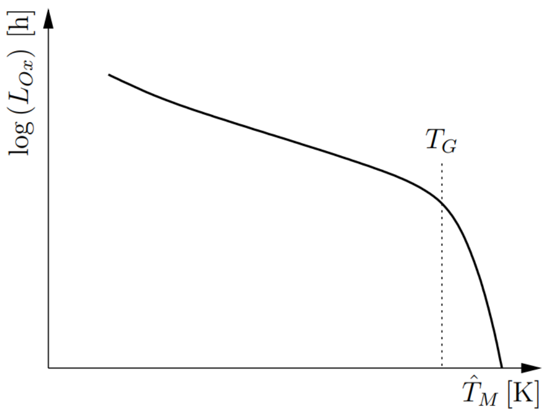

Figure 2.5: Material characteristic of protective layer lifetime L_{Ox} with temperature T, from [3, p. 10]

2.4.2 Erosion

Erosion specifies the mechanical abrasion of the surface of a material [32]. It can occur in most systems. Its rate is influenced by the fluid velocity, which can be increased, especially in bends and sudden changes of the flow path, the material itself, as well as the roughness of the chosen material [47]. A higher flow velocity can lead to a higher impact velocity of particles in the fluid. Therefore, limiting fluid velocity can be one measure to reduce the effects of erosion [35].

2.4.3 Fracture/Strength

Fracture is defined as the separation of one component into two or more parts occurring in a relatively short amount of time. Two fracture mechanisms exist: ductile and brittle fracture. Ductile fracture, seen in the sample (c) in Figure 2.6 is characterized by yielding and plastic deformation. The von Mises stress acting on the component exceeds the uniaxial tensile stress of the material. The material is plastically deformed and, ultimately, fractures as the resulting stress increases with decreasing cross-sectional area due to the deformation process. Sample (c) represents a completely ductile fracture, with the fracture area being infinitesimally small. However, in reality, ductile fracture looks more like sample (b) in the same Figure 2.6. Brittle fracture, in contrast, can occur even if the applied stresses are below the yield stress. It can develop due to stress concentrators in the material, like pre-existing imperfections in the material. Brittle fractures feature little plastic deformation, as

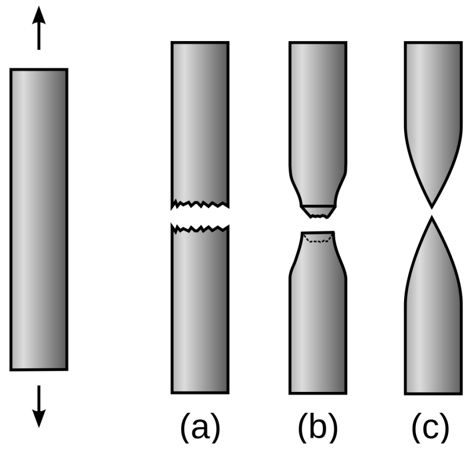

Figure 2.6: Overview showing different types of fractures: Brittle (a), ductile (b), and completely ductile (c), from [4]

can be seen in the sample (a) in Figure 2.6. A brittle fracture can even occur with no plastic deformation at all. The dominant fracture mechanism depends on several influence factors, like the acting stress level, the presence of pre-existing defects, material properties, and environmental conditions. [32]

2.4.3.1 Relevance for Structural Design of Heat Exchangers

Fracture of PFHE has been investigated in two main operational environments: One is in cryogenic environments with high pressure differences and low temperature differences [48, 49, 50] and the other is in conditions featuring high temperatures and pressures, like in nuclear reactors [51, 52, 53, 54, 55]. However, all analyses employed FEM. The location of the highest stresses occurs at keen-edged geometric structures [48], especially at the joints [53, 54, 55]. Additionally, connections between components with different material properties, like different thermal expansion coefficients and stiffnesses, lead to increased stresses [49, 51, 52]. The resulting stress can either be driven by temperature gradients leading to different thermal expansion or by pressure gradients. The dominant stress source depends on the operational conditions. In cryogenic conditions, the pressure loads are more dominant [48, 50, 55]. However, in conditions with high temperature differences, the temperature induced stresses dominate the pressure loads even if significant pressures occur [54].

Fracture can occur in TBHE as well. It can be caused by several reasons, including steam or water hammering or a loss of cooling water. Steam or water hammering occurs due to rapid changes in flow velocity which lead to damaging pressure surges, while a loss of cooling water leads to overheating and potential melting of the material. It occurs at high temperature and pressure gradients in bends and locations of the tube, where the thermal expansion is restricted. [35, 36]

An investigation of a cross-counter flow HX for usage in an intercooled recuperative aero engine, depicted in Figure 2.7, emphasized the importance of performance and structural mechanics in an HX analysis. The temperature profiles and stress distributions vary significantly during different operational phases, such as acceleration and deceleration. Using FEM, the location of the maximum stresses has been determined to be the connections between different structural parts, identical to the PFHE. [5]

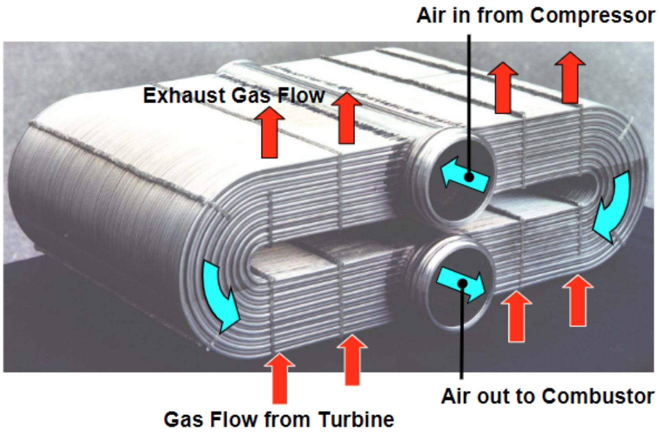

Figure 2.7: Lancet heat exchanger as described in [5], from [6]

2.4.3.2 Possible Constructive Measures and Assessment Methods

Preventive measures for mechanical failure include the usage of steam traps and proper material selection as well as proper sizing [35, 36]. Often, the design of HXs follows well-established norms, like [39]. It includes sizing guidelines based on pressure as well as thermal stresses and mechanical loading. A strength assessment of the TBHE from [5] investigated the lancets as well as connecting pipes. The lancets were modeled as two cylindrical tubes with equivalent cross-section. Based on the take-off conditions, stresses due to the inner overpressure, as well as stresses due to the flow of the exhaust gas, have been calculated and superimposed. Calculation methods have been derived from [56]. With the chosen geometrical parameters, strength was sufficient. However, foreign object damage (FOD) could damage the HX, leading to leakages and, subsequently, an increase in fuel burn. [57]

Increasing wall thickness leads to a higher safety factor against pressure differences. However, a higher wall thickness increases thermal stresses [56]. The necessary entry and exit tubes in PFHE lead to locally different temperature profiles and hence stresses, making a structural assessment difficult [20].

2.4.4 Buckling

Buckling is a geometric instability phenomenon. An excessive axial compressive load beyond a critical value leads to significant out-of-plane bending displacements. Until this displacement occurs, the work done by the applied force is stored as compression. However, at some point, the stiffness is too low to withstand the compression, and thus, the additional work done by the load is stored as bending strain energy, and the material deforms. This nonlinear phenomenon is especially relevant for thin structures, like plates, as the stiffness against compression is low. [58]

The literature research revealed no cases of buckling in either TBHE or PFHE. Additionally, the author has found no specific constructive measures or assessment methods for buckling in the literature. However, general structural mechanics laws for plate buckling apply.

2.4.5 Fatigue

In many cases, a component is loaded by an average stress as well as an alternating, additional stress. Fatigue accounts for these changing stress levels. It is the most common mechanical failure mode caused by alternating, repeating, or randomly recurring stresses on a system. Failure occurs as soon as the magnitude of applied stresses exceeds the fatigue strength. Each fatigue strength responds to a set number of cycles for which the stress can be applied. One distinguishes two types of fatigue:

low-cycle fatigue (LCF), meaning that failure occurs at a small number of cycles (e.g. less than 10^3 cycles) and thus under a higher stress and lower frequency, and high-cycle fatigue (HCF), which is described by failure after a high number of cycles (e.g. more than 10^3 cycles) and a lower stress. The specific number of cycles is dependent on the actual material behavior. The failure development of both types consists of three stages. First, a crack is formed during the crack initiation. Secondly, the crack grows in the sub-critical crack propagation phase. Ultimately, final fracture occurs if the crack reaches critical elongation. [32]

Thermal fatigue is a specific type of anisothermal LCF. Sudden heating and cooling of components, which does occur when starting an aero engine, lead to an expansion and contraction of the material, respectively. Figure 2.8 shows a turbine blade undergoing thermal stresses. When heating up, the edges heat up faster than the middle of the blade chord due to the thermal inertia, as shown in Figure 2.8 (a). During cooling down, the opposite happens, with the blade edges shrinking faster than the middle of the blade, visualized in Figure 2.8 (b). If these thermal strains

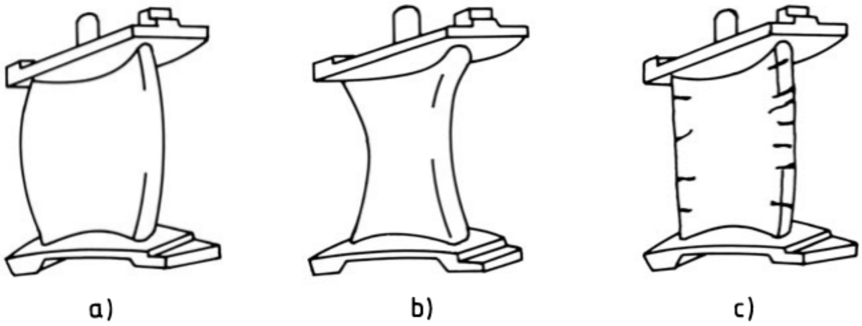

Figure 2.8: Thermal breathing of a turbine blade: (a) shows the deformation during heating, (b) shows the deformation during cooling, and (c) shows resulting cracks forming on blade edges, from [7]

are totally or partially restricted, thermal stresses arise. Repeating these thermal transients can result in thermal fatigue of the component, leading to cracks at the edges, as seen in Figure 2.8 (c). In most cases, thermal fatigue acts in addition to already existing mechanical stresses. A higher temperature gradient leads to a more pronounced thermal fatigue, as it leads to a higher thermal stress. [59]

Thermal fatigue has been compared to the simplified case of uniaxial isothermal fatigue. Experiments on an electrically heated and cyclically water-cooled, stainless steel, cylindrical specimen have been carried out and compared to results from thermal and mechanical analyses using FEM. The initiation of cracks due to thermal fatigue occurs before the initiation of cracks due to uniaxial isothermal fatigue. The biaxial state leads to a higher hydrostatic stress compared to the latter, uniaxial state. Hence, the biaxial stress state is more critical than the uniaxial stress state. Therefore, uniaxial stress-life curves need to be treated carefully. [60]

2.4.5.1 Relevance for Structural Design of Heat Exchangers

Fatigue in PFHE mainly results from four root causes: An inappropriate choice of working parameters can lead to thermal overload due to a high temperature or to mechanical overstresses due to high stresses. Residual stresses generated during the manufacturing process, e.g. due to welding, can lead to fatigue fracture as well. However, proper heat treatment can often omit this root cause. Welding the material can cause metallurgical transformation of the material, leading to undesired material properties, like embrittlement of increased grain size. Additionally, welding can cause porosity or microcracks in the weld deposit and heat affected zone. Special care needs to be taken during the heat treatment to avoid reheat cracking. Vibration can lead to crack formation and propagation. Additionally, it can damage protective films, allowing corrosion. Especially in tight assembly zones, vibration can cause contact between elements next to each other. The vibration itself can be caused by the working environment of the HX as well as the fluid flow conditions, especially if the flow is turbulent. [47]

Failure of PFHE due to fatigue has been investigated in water-nitrogen HXs ([52]), air-nitrogen HXs ([61]) and high-temperature HXs ([62]).

Failure due to fracture occurs, similar to the fracture case, in locations with high temperature and pressure differentials, especially at joints. If the joint is sufficiently strong, failure occurs at the fins [62]. Independent of the location of failure, the resulting cracks can lead to leakages. [53, 61]

Literature often employs FEM to determine the resulting stresses. To simplify the computation, the PFHE stack can be divided into different sections, like the sidebars and the matrix consisting of the plates and fins. Each has assumed isotropic properties. The resulting model is well-suited for the calculation of HXs. [52]

TBHE fail due to fatigue as well. The cyclic behavior of HXs, including start-up and shutdown, can lead to cyclic thermal stresses if the material cannot elongate freely. Cracks form radially around the tube, especially in bends and constrained positions. [35]

To allow free elongation, U-shaped tubes can be used, like in Figure 2.7. Here, no significant LCF was observed. [5]

Vibration can lead to fatigue stress cracks mainly at the point where tube movement is restricted [35]. It can be analyzed by determining the Eigenmodes of the profile tube package. As long as the geometry constrains the movement of the oscillations, the component can experience HCF.

2.4.5.2 Possible Constructive Measures and Assessment Methods

The proper assessment of fatigue involves the determination of occurring load cases. Each case occurs for a number of cycles and creates a set amount of stress. By summing up all occurring load cases and the involved load-cycle combination, the lifetime of a part can be assessed. [51, 52]

In general, two main approaches are described in the literature for the calculation of the estimated life cycles for each load case: the stress-life and the strain-life approach. The underlying theory and equations will be explained below. Besides these theoretical approaches, industry standards like [39] offer guidelines on constructive measures against fatigue failure.

Stress-Life (σ-N) Approach The stress-life approach is the most common and fundamental approach to fatigue estimation. It assumes that members of the same material have the same fatigue life if the stress concentration factor and loading history are the same. This excludes the effects of plasticity. To assess the structural integrity of a part, the occurring stress of each load case is compared to the material properties displayed by the Wöhler-curve. The Wöhler-curve is given for a set stress ratio R, describing the ratio of the higher to the lower stress. Material data is typically given for $R = -1$, which means alternating compression and tension with the same stress magnitude. This leads to a zero mean stress. In practice, in most of the cases, the mean stress is non-zero. Therefore, correction models enabling the calculation of equivalent zero-mean stresses, like the Goodman linear model, have been derived. [63]

The Goodman diagram, visualized in Figure 2.9, plots occurring mean stresses, σ_m and the ultimate tensile stress (UTS) of the material on the x-axis and the amplitude of the alternating stress, σ_a and endurance limit, S_e on the y-axis. The allowable alternating stress, assuming zero mean stress, σ_a^*, can be derived using Equation 2.2, indicated by the dashed line in the figure. The resulting stress amplitude is hence determined by the ratio between the acting mean stress and the UTS as well as by the acting stress amplitude.

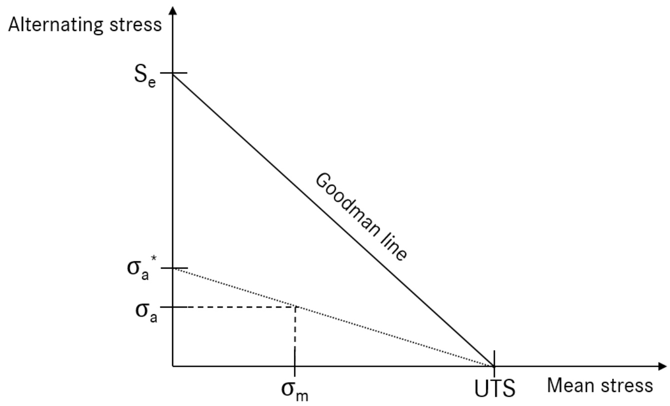

Figure 2.9: Exemplary Goodman diagram, as described in [8]

$$\sigma_a^* = \frac{\sigma_a}{1 - \frac{\sigma_m}{UTS}} \tag{2.2}$$

Furthermore, the Goodman diagram can be used to assess HCF. Components experiencing high cycle fatigue are designed for infinite life. In practical terms, a certain number of cycles, known as the endurance limit, is assumed to be sufficient for infinite life. A typical value of the endurance limit is 10^8 cycles. To assess the load condition and the resulting fatigue strength, each load condition is compared to the

Goodman-line. Points below the Goodman-line are assumed to lead to infinite life, while points above the Goodman-line lead to premature failure.

Therefore, from the Goodman diagram, load conditions falling in the region below and to the left of the curve are assumed to be withstood for (at least) the number of cycles equal to the endurance limit.

Despite the Goodman-linear model, further approximations exist, like the Gerber-Equation. It is more applicable to materials with a high yield to tensile strength ratio [64]. However, it is less conservative than the Goodman-equation, as it does not use a linear connection between the stress at the endurance limit and the UTS, but a quadratic one. The corresponding Gerber line therefore is to the right and above the Goodman line, enlarging the safe life area.

Strain-Life (ϵ-N) Approach The strain-life (ϵ-N) prediction method is used to determine the fatigue life of materials, particularly under significant plastic deformation. Therefore, it is especially suited for LCF. The fatigue life estimation of a component is based on its strain behavior under cyclic loading conditions. The underlying assumption provides that components from the same material under identical cyclic loads will exhibit similar local strains and, thus, fatigue lives. It accounts for influences of the load history, geometric shape and the material. It can thus yield an improved accuracy compared to the Stress-life approach. However, extensive knowledge of the material's strain behavior is required. The structural assessment process involves deriving the strain resulting from the stress of each load case. It is then compared to the material-specific strain-life curve.

Accumulation of Damage from Multiple Load Cases After the lifetime of each load case is determined, the total damage and hence the total lifetime can be derived using Miners linear damage rule, as shown in Equation 2.3. [51, 52]

$$D_{\text{total}} = \sum \frac{n_j}{N_j} \tag{2.3}$$

D_{total} is the total, accumulated damage. $n_{\text{cycles},j}$ is the actual number of cycles for which the load condition j occurs, and N_j is the material property describing the number of cycles the material can withstand until failure.

2.4.6 Creep

Creep is the occurrence of time-dependent plasticity under a fixed stress and elevated temperature. The temperature often is higher than $0.5 \cdot T_{mt}$ with T_{mt} being the absolute melting temperature. Three distinguishing stages exist and are shown in Figure 2.10: The first stage, primary creep, describes the region in the strain-time curve in which the plastic strain rate changes with time. In the second stage, called secondary or steady-state creep, the strain rate decreases towards a constant value. During the third stage, called tertiary creep, cavitation and/or cracking increase, and hence, the strain increases until the material fractures. Sometimes, the secondary or steady-state creep is omitted and the primary creep stage is directly followed by the tertiary creep stage. [65]

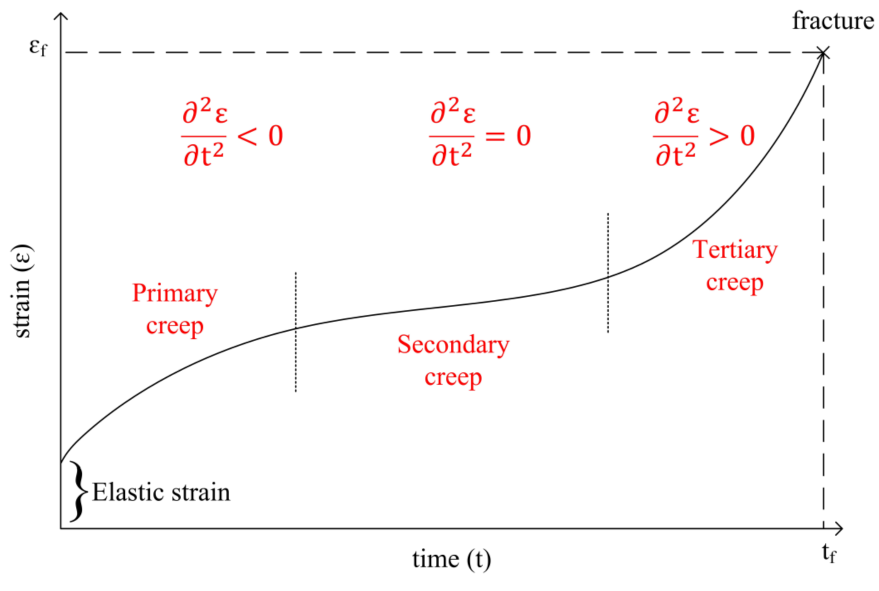

Figure 2.10: Strain-time-curve including different stages of creep, from [9]

2.4.6.1 Relevance for Structural Design of Heat Exchangers

The importance of creep strongly depends on the temperature acting on the heat exchanger type. Using the use case of the WET concept, significant creep is only expected in the TBHE and not in the PFHE. However, depending on the temperature level, significant creep can occur in the PFHE as well.

In general, creep rupture in PFHE can occur by primary stress, which is the stress resulting directly from the loading and can occur in high-temperature environments. The temperature of the thermal aging process, which is the temperature during the heat exchanging process, significantly affects creep resistance. A higher temperature generally leads to a lower creep resistance. Correction factors have been derived to account for the changes in material properties. Failure especially occurs at fins, as the fins are typically thinner and completely exposed to the hot flow, which leads to higher material temperatures. [62]

In TBHE, creep can lead to intergranular, transgranular or rupture failures. It can be caused by locally increased temperatures due to corrosion or other defects. Primary factors influencing creep are time, temperature and stresses. Approximately 30 % of all failures of HXs are due to creep rupture. Essential design parameters include the scaling resistance, the wall thickness and the thermal conductivity of the tube material. In general, tubes should feature high stiffness and denting resistance, which are dependent on the elastic modulus and yield strength of the tube's material as well as the diameter and wall thickness of the tubes. However, to manufacture finned tubes highly ductile material is required. [37]

In the cross-counter flow HX described in Figure 2.7, creep damage is only significant at the first row exposed to the hot exhaust gas at the connection of the inner tube to the manifold tube of the reheated air moving towards the combustion chamber due to the highest internal pressure and hot exhaust gas temperature. [5]

2.4.6.2 Possible Constructive Measures and Assessment Methods

Existing methods for assessing creep mainly focus on FEM analyses. Substitute models for easing the computational effort have been developed by splitting one complex model into several submodels with constant material properties, as can be seen in Figure 2.11.

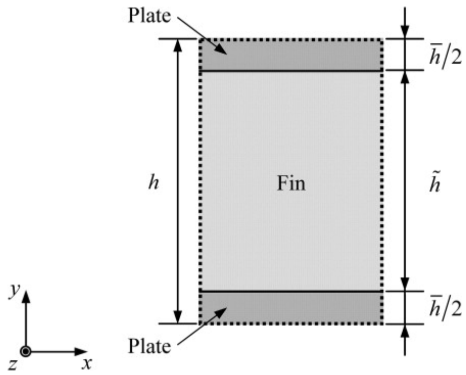

Figure 2.11: Duplex model as a substitute model for full-scale FEM analysis with two distinct submodels: one for the plate and one for the fin [10]

The plate layer is described by ordinary power-law equations of viscoplasticity, while the fin layer is represented using the anisotropic, compressible power-law equation. Material parameters were derived by performing a homogenization analysis in six cases: Tension in all directions x, y, z and shear in all planes xy, xz, yz. Verification with a full-scale FEM model shows excellent prediction of steady-state macros-stress under biaxial loading. However, it can only describe combinations of uniaxial tension and simple shears. Additionally, the model cannot be used near the core boundaries and, hence, for a small number of plates and fins, as significant local stress concentrations can occur there. [10]

To allow the analysis of more complex load cases, analytical formulas for the elastic moduli, shear moduli and Poisson's ratios are derived using the previously mentioned duplex model. The findings are verified against a full-scale FEM analysis and experimental data. The derived formulas are in good agreement with FEM results. Compared to the measurement, the elastic modulus in the direction of the side bar(z-direction) is slightly higher than the measured value. This can be due to the neglect of bending in the model. In general, elastic moduli and shear moduli increase with increasing face sheet thickness and fin thickness. However, elastic moduli decrease with increasing length of the fins. [12]

Further assessment methods are described in industry norms like the DIN EN 13445 ([39]). Typically, material-specific creep curves are given, involving the time until creep ruptures for a given stress. By calculating the stress and the material temperature, the maximum allowable time at the given load condition until creep rupture can be assessed. Creep damage can then be derived by using Miners linear damage rule.

Overall, creep damage can be reduced either by reducing the material temperature, choosing a more creep-resistant material, or reducing the acting stresses.

2.4.6.3 Creep-Fatigue Interaction

To estimate the total damage done by both creep damage, D_c, and fatigue damage, D_f, can be added linearly together, following Equation 2.4. The model assumes that the fracture occurs when the total damage exceeds a critical damage D.

$$D_c + D_f = D \tag{2.4}$$

However, the critical damage D needs to be determined experimentally. If one would assume $D = 1$, the interaction between creep and fatigue is ignored [66]. The creep-fatigue interaction diagram is given for 304 and 316 stainless steel, alloy 800H, 2,25Cr-1Mo alloy, 9Cr-1Mo-V steel and alloy 617, among others [67].

A creep-fatigue interaction diagram for the material assumed for the heat exchanger in this thesis, alloy 625, does not exist. As alloy 625 is similar to alloy 617, the creep-fatigue interaction diagram of alloy 617 is used.

2.4.7 Fouling

Fouling is the sedimentation of solid particles inside cross-sections, leading to a reduction of the cross-sectional area and eventually to blocking. While fouling is not a structural failure mode, it leads to significant impacts on the performance of HXs, including increased thermal resistance and thus reducing the HXs ability to transfer heat. [47]

2.4.7.1 Relevance for Structural Design of Heat Exchangers

Fouling occurs especially at lower flow rates and at enhanced surfaces [47]. It leads to a film deposited on the surface of heat transfer surfaces. It acts as an insulator, increasing the wall temperature and corrosion risk. Increasing the fluid velocity can aid in preventing the formation of an insulative layer. However, a velocity that is too high increases the risk of corrosion. [35]

2.4.7.2 Possible Constructive Measures and Assessment Methods

Fouling can be prevented by sufficiently high flow velocities in both fluids and proper operation and maintenance, including regular cleaning [36]. No literature to date is known to assess the expected structural damage introduced by fouling.

2.4.8 Further Failure Modes

The combination of mechanical failure and chemical-induced corrosion can lead to a quicker failure than if each of them were acting independently. The main causes are the occurrence of erosion combined with corrosion and the combination of corrosion with fatigue. Erosion removes the protective films due to the minerals, while ruptures are introduced due to fatigue and break the protective film. Both increase the risk of corrosion. [35]

High temperature hydrogen attack is stated as another failure mechanism. It occurs, when carbon steel is exposed to H_2 at temperatures over 205 °C. Molecular hydrogen then converts to nascent hydrogen, which diffuses into the carbon steel surface. There, methane is produced, which cannot escape. A pressure builds, which eventually leads to cracks. [37]

2.4.9 Overview of Failure Modes in Heat Exchangers

The following tables give an overview of potential failure modes identified in the literature and their probable root causes. A more detailed description of all failure modes can be found above. Table 2.1 shows common failure modes associated with PFHE, while Table 2.2 addresses failure modes of TBHE.

Table 2.2: List of possible failure modes, including their root causes and location of TBHE, as found in literature

Failure mode	**Root cause**	**Occurrence**	**Source(s)**
Corrosion (Condensate grooving)	Condensate grooves lead to corrosion cell in wet area	Outside of steam-water HX tubes, in bend areas	[35]
Corrosion (Crevice)	Localized cell leading to metal loss	Secluded areas, under scale/dirt, stagnant conditions	[35]
Corrosion (Dezincification)	Removal of zinc from material	Alloys with more than 15% zinc	[35]
Corrosion (Galvanic)	Electrochemical reaction between two different materials	Joints between metals with different nobilities	[35]
Corrosion (General)	Interaction between material and circulating fluid	Can occur everywhere	[34, 36, 37, 47]
Corrosion (Pitting)	Concentration cell due to different oxygen concentrations	Around scratches or dirts (pits)	[35, 68]

Table 2.2: (continued)

Failure mode	**Root cause**	**Occurrence**	**Source(s)**
Corrosion (SCC)	Residual stresses from manufacturing	Joints of tubes and tube sheets, inside tubes with high operating temperature	[35, 38, 69]
Erosion	Excessive fluid velocity or high levels of total dissolved solid	Inlet or in bends	[35, 36, 47]
Strength (Static Stress)	Excessive pressure and thermal stresses	Position with biggest temperature difference	[5]
Strength (Steam hammer)	Sudden pressure changes lead to condensation	Can occur everywhere in the region of the limit of vaporization	[35, 36]
Strength (Weld joints)	Weakened structure due to welding	Weld joints	[37]
Fatigue (LCF)	Cyclic thermal expansion	Locations with restricted expansions or different elongations	[5, 35, 37, 47, 70]
Fatigue (HCF)	Wear, crack formation or resonance disaster	Between adjacent parts in contact or components with no geometrical constraints	[5, 35, 37, 47]

Table 2.2: (continued)

Failure mode	**Root cause**	**Occurrence**	**Source(s)**
Creep	Excessive operating temperature	Position with the highest material temperature and lowest creep resistance	[5, 35, 37]
Hydrogen attack	Carbon steel exposed to hydrogen at temperatures higher than 205°C	Can occur everywhere	[37]

While condensate-grooving corrosion, SCC, steam hammering, and hydrogen attack were described as failure modes of TBHE due to their range of application, all failure modes could occur in PFHE under certain operating conditions as well. Additionally, failures can occur due to combinations of different failure modes, such as erosion and corrosion as well as corrosion and fatigue.

It is crucial to analyze all potential failure modes to accurately assess the structural integrity of heat exchangers. This thesis focuses on heat exchangers operated in the exhaust gas of jet fuel combustion. Therefore, no significant amount of hydrogen is expected. Hence, this thesis does not investigate hydrogen attacks. However, if the heat exchanger were to be used for hydrogen in fuel cells, hydrogen would need to be considered as an additional failure mode.

Table 2.1: List of possible failure modes, including their root causes and locations of PFHE, as found in literature

Failure mode	**Root cause**	**Occurrence**	**Source(s)**
Corrosion (Crevice)	Localized cell leads to metal loss	Secluded areas or under scale or dirt, stagnant conditions	[35]
Corrosion (Dezincification)	Removal of zinc from the material	Alloys with more than 15% zinc	[35]
Corrosion (Galvanic)	Electrochemical reaction between two different conductive materials	Joints between metals with different nobilities	[35]
Corrosion (General)	Interaction between material and circulating fluid	Can occur everywhere	[34, 47]
Corrosion (Pitting)	Concentration cell due to differences in oxygen concentration	Around scratches or dirt (pits)	[35]
Erosion	High levels of total dissolved solid	locations with high fluid velocity	[47]
Strength (Brazed joints)	Brazing material weaker than components	Brazed seams	[49]
Strength (Static stress)	Thermal and/or pressure loading	Corner region of fins to either plate	[48, 54, 55]
Fatigue (LCF)	Different elongation of two materials leading to thermal stresses	Joints of two materials	[47, 50, 51, 53, 61, 62]
Fatigue (HCF)	Wear and crack formation	Between adjacent parts in contact	[47]
Creep	Excessive operating temperature	Fins, if braze strong enough, otherwise braze material	[10, 12, 62]

3 Methodology

3.1 Heat Exchanger Setup

Two heat exchanger types are assessed in this thesis: PFHE and TBHE. Their respective general setup and input parameters are presented in this section.

3.1.1 Plate-Fin Heat Exchanger Setup

An exemplary PFHE setup is shown in Figure 3.1, including all relevant input parameters. The stack layout can be described by the plate length l_{plate}, the plate width w_{plate}, and the stack height h. All plates and sidebars typically have the same thickness t_{plate} and t_{sidebar}, respectively. Furthermore, each flow passage can be described by its height h_i, the fin thickness $t_{\text{fin,i}}$, as well as the fin density FD_i. The fin density FD describes the number of fins per unit length. In this thesis, the fins are assumed to be plain fins. Typically, all fins of each flow passage are manufactured as one corrugated sheet, leading segments parallel to the plate and the orthogonal

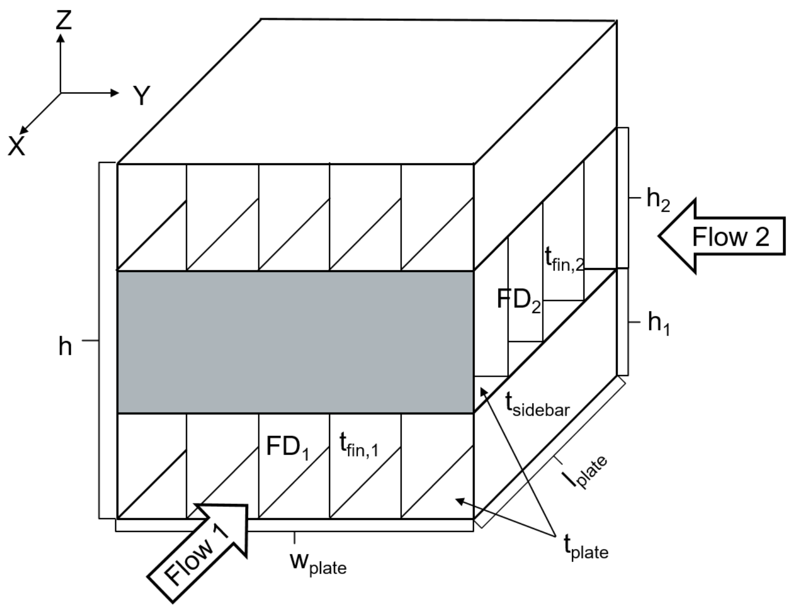

Figure 3.1: Exemplary PFHE setup

fins shown in Figure 3.1. For simplification purposes, the segments parallel to the plate are neglected in this thesis.

The total number of passages can be calculated using Equation 3.1. Typically, PFHE feature a large number of passages. The additional flow passage in case of equal flows in the top and bottom passages is thus neglectable. Therefore, the calculated number of passages is rounded to the nearest integer number, corresponding to the number of total passages, assuming different flows in the top and bottom passage.

$$n_{\text{passages}} = \lceil \frac{2 \cdot (h - t_{\text{plate}})}{h_1 + h_2 + 2 \cdot t_{\text{plate}}} \rceil \tag{3.1}$$

The PFHE is assumed to be made of Al6061-T6, an aluminum alloy. Temperature-dependent basic material properties are derived from [71]. Further temperature-dependent properties, like the yield and ultimate strength, have been derived from [72]. Fatigue curves have been used from [64]. A temperature correction factor is described in [73]. The material temperature is calculated as the average temperature of both the upper and lower plate surface.

3.1.2 Tube Bundle Heat Exchanger Setup

An exemplary TBHE is shown in Figure 3.2, including all relevant input parameters. The tubes can be described by their inner diameter d_{inner}, their wall thickness t_t, and their outer diameter d_{outer}. The general geometry of a tube bundle can be characterized by the length of one tube passage l_p, the number of passages per tube n_p, the number of tubes n_t as well as the vertical and horizontal distance between adjacent tubes SL and ST, respectively. The fins, used to increase the heat transfer area, can be described by their fin thickness t_{ft} and the corresponding fin density FD_t.

The vaporizer is assumed to be made of Inconel 625, a nickel-based alloy. The necessary material data can be found in [74]. The corresponding material temperature is calculated as the average of both the inner and the outer tube walls. However, no time-dependent data is available for the 1% creep resistance of Inconel 625. The creep behavior is described for 10^4 and 10^5 hours in a material specification from

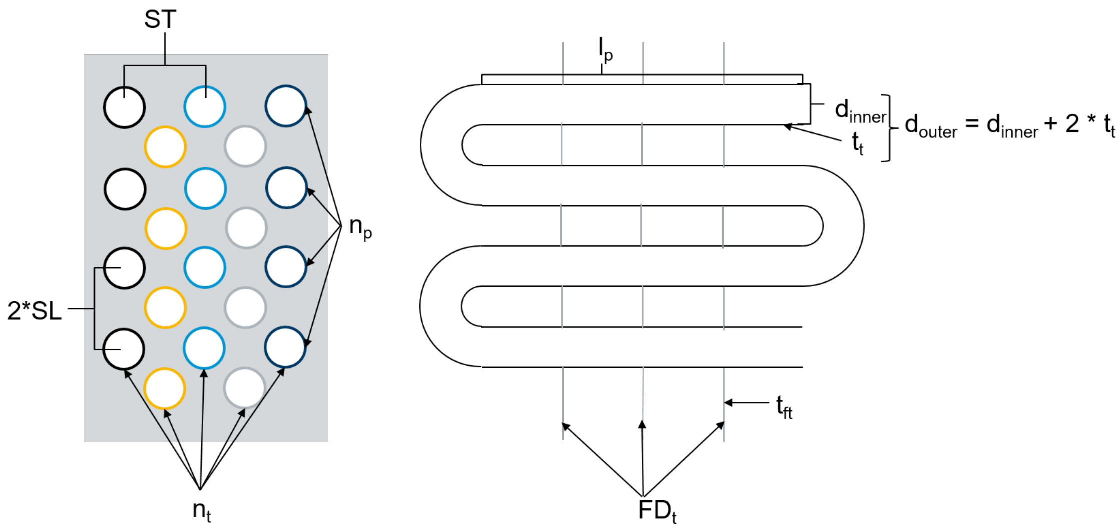

Figure 3.2: Exemplary TBHE setup

another manufacturer [75]. However, the creep rupture strength is inconsistent with [74]. The 1% creep resistance is calculated from the creep rupture mentioned in [74] by using a conversion factor of 1.39 to keep the data consistent. The conversion factor is derived from [75].

3.2 Structural Assessment of Failure Modes in Heat Exchangers

This section discusses the structural assessment of the failure modes presented in Section 2.4.9. Factors of safety are derived for both PFHE and TBHE heat exchanger types. Section 3.2.1 provides an overview of the general modeling approach. Subsequently, the assessment methods for both types of heat exchangers are described.

3.2.1 Overview of the Proposed Methodology

The objective of this methodology is to evaluate the structural integrity of a given HX geometry. The essential input data includes the pressure and wall temperature levels along an exemplary flow path. These values are used to calculate stresses resulting from pressure differences, weight, and temperature, which are then compared to material data. Figure 3.3 provides a general overview of the calculation approach.

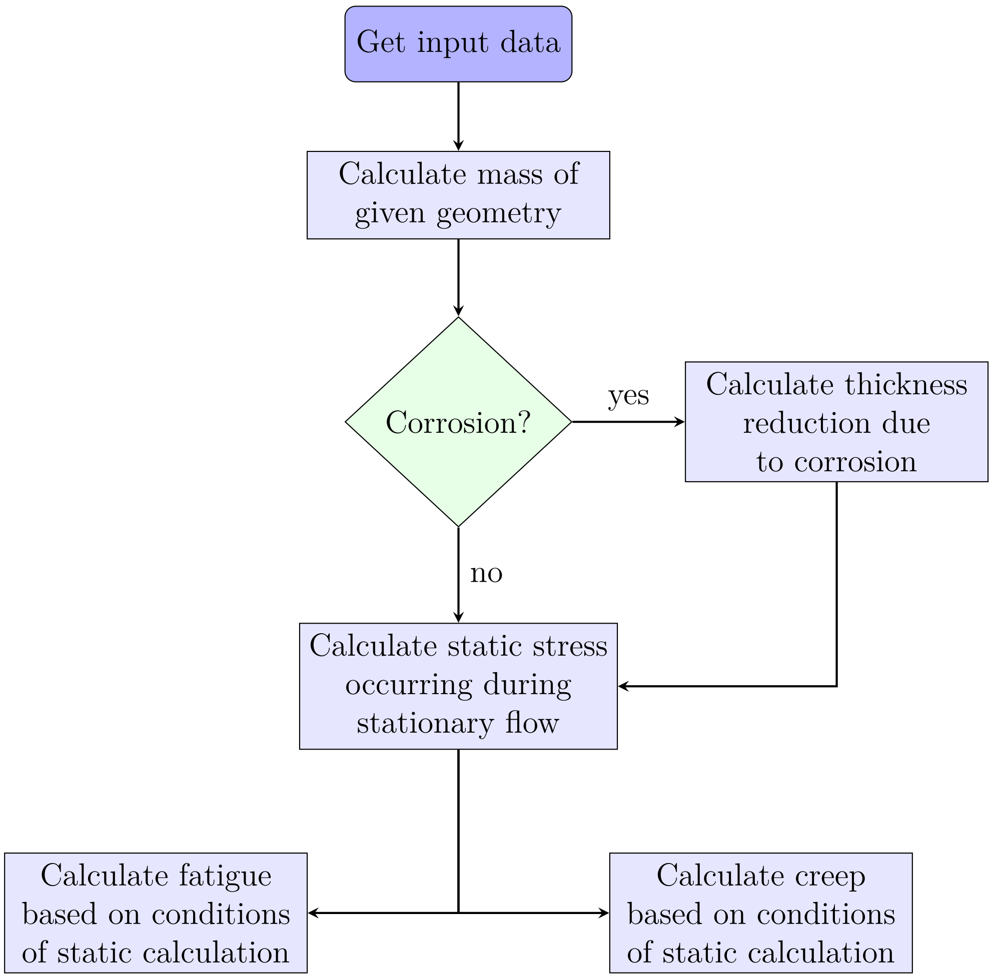

Figure 3.3: Schematic overview of the proposed assessment methodology

Initially, the input data is utilized to determine the mass of the given geometry. Depending on user input, the component thickness can be reduced to account for corrosion. This adjusted thickness is then employed to calculate the static stress during stationary flow, assuming the specified pressure and temperature levels as input. Lastly, the methodology assesses fatigue and creep damage.

3.2.2 Mass Calculation of Plate-Fin Heat Exchanger

The mass of a PFHE can be calculated by calculating the respective volumes and using the density of the material. The mass of the plates can be calculated by Equation 3.2.

$$m_{\text{plates}} = n_{\text{passages}} \cdot l_{\text{plate}} \cdot w_{\text{plate}} \cdot t_{\text{plate}} \cdot \rho_{\text{plate}} \tag{3.2}$$

As both passages can feature different fin densities, the mass of all fins features two terms, as Equation 3.3 shows. The number of passages of each flow can be determined by dividing the total number of passages, n_{passages} by 2, assuming different flows in the top and bottom passage.

$$\begin{aligned} m_{\text{fins}} =& \{[(l_{\text{plate}} \cdot h_1 \cdot t_{\text{fins},1}) \cdot (w_{\text{plate}} \cdot \text{FD}_1 \cdot \frac{n_{\text{passages}}}{2})] \\ &+ [(wplate \cdot h_2 \cdot t_{\text{fins},2}) \cdot (l_{\text{plate}} \cdot \text{FD}_2 \cdot \frac{n_{\text{passages}}}{2})]\} \cdot \rho_{\text{plate}} \end{aligned} \tag{3.3}$$

The mass of the sidebars can be calculated according to Equation 3.4.

$$m_{\text{sidebars}} = 2 \cdot [(l_{\text{plate}} \cdot h_1 \cdot \frac{n_{\text{passages}}}{2}) + (w_{\text{plate}} \cdot h_2 \cdot \frac{n_{\text{passages}}}{2})] \cdot t_{\text{sidebar}} \cdot \rho_{\text{plate}} \tag{3.4}$$

The total mass of a PFHE stack can be calculated by Equation 3.5.

$$m_{\text{PFHE}} = m_{\text{plates}} + m_{\text{fins}} + m_{\text{sidebars}} \tag{3.5}$$

3.2.3 Mass Calculation of Tube Bundle Heat Exchanger

The mass of a TBHE can be calculated similarly to the PFHE. All component weights need to be added up. However, the calculation of the weight of the components varies. The total mass of the tubes can be calculated by Equation 3.6.

$$m_{\text{tubes}} = \pi \cdot ((\frac{d_{\text{outer}}}{2})^2 - (\frac{d_{\text{inner}}}{2})^2) \cdot (n_p \cdot l_p + l_{\text{bends}}) \cdot n_t \cdot \rho_{material} \tag{3.6}$$

The additional length due to the bends, l_{bends}, can be calculated using Equation 3.7.

$$l_{\text{bends}} = \pi \cdot SL \cdot (n_p - 1) \tag{3.7}$$

As the TBHE features fins, their mass must also be calculated. The tubes pass through the fins, leading to the fins having the shape of a perforated plate. The mass of the fins can therefore be calculated following Equation 3.8.

$$m_{\text{fins}} = (h_{ft} \cdot w_{ft} - n_t \cdot n_p \cdot (\frac{d_{\text{outer}}}{2})^2) \cdot (FD_t \cdot l_p) \cdot t_{ft} \cdot \rho_{ft} \tag{3.8}$$

The height, h_{ft}, and width, w_{ft}, of the fins is derived using Equations 3.9 and 3.10, respectively.

$$h_{ft} = 2 \cdot n_p \cdot \mathrm{SL} \tag{3.9}$$

$$w_{ft} = (n_t + 1)/2 \cdot \mathrm{ST} \tag{3.10}$$

The total mass then can be calculated using Equation 3.11.

$$m_{\mathrm{TBHE}} = m_{\mathrm{tubes}} + m_{\mathrm{fins}} \tag{3.11}$$

3.2.4 Corrosion

After the mass calculation, the corrosive behavior of the material is assessed. A metallurgical analysis showed different types of corrosion, including pitting and galvanic corrosion. However, typically, the dominant corrosion behavior of a component is not known in predesign. Therefore, all corrosion failure modes are summarized and reduced to one method. The influence of constructive measures and protective layers on the mass of a heat exchanger is hard to estimate. Therefore, for both PFHE and the TBHE no protective layers or other constructive measures for avoiding corrosion are assumed. An approach deriving a corrosion allowance is applied. It is the industry standard and explained more thoroughly in Section 2.4.1.2. Due to the nature of aero engines and their interrupted service (e.g., when the engine is shut down), the corrosive loading is cyclic. However, as no reliable data on the time spans without corrosive loading is known, a constant corrosion exposure is assumed. This leads to a more conservative estimation than a cyclic corrosion exposure [33, 76].

Hence, a constant, uniform corrosion rate per flow is assumed for both heat exchanger types. It acts for the required amount of lifetime, LT, on the surfaces in contact with the specified flows. The corrosion allowance can then be calculated by Equation 2.1. However, as we assess the corrosion behavior of a given geometry, the normally to-be-added corrosion allowance is subtracted from the thickness on the respective wall, leading to the remaining thicknesses after the LT. The heat exchanger has to withstand all loads, even in this case. Furthermore, the heat exchanger is assumed to withstand all the occurring loads with the original, thicker walls as well. Using the outlined approach yields new thicknesses of the plates and fins as well as new inner and outer diameters of the tube. As both flows of each heat exchanger are significantly different in terms of chemical composition and temperature, a corrosion rate has been derived from the literature for each flow. These corrosion rates can be further adjusted if component corrosion tests are conducted at a later design stage.

3.2.4.1 Corrosion Rates in aluminum Plate-Fin Heat Exchanger

A heat-treated, 4 % SiC reinforced Al6061 specimen, commonly used in the aerospace industry, showed a corrosion rate of approximately 0.3 mil per year [77]. Converting this to SI units leads to 0.0762 mm/y.

Another study investigated the corrosion rate of an Al6061 specimen in simulated acid rain with a pH value of 4.8. The corrosion rate was determined to be 0.068 mm/y. [78]

Both studies result in similar values. The goal of this thesis was to accurately assess HX geometries. Therefore, instead of the more conservative, higher value, this thesis uses the average value for the surfaces facing the hot flow. This leads to a corrosion rate of the PFHE of 0.0721 mm/y. However, the influence of different corrosion rates is further investigated in Section 4.2.1.

The behavior of solution-treated Al6061 in rainwater has been investigated. Solution treatment is a heat treatment process involving heating the specimen and, subsequently, rapid cooling in a solution. During heating, precipitates are produced, which remain in the solution after cooling. The study derives a corrosion rate of approximately 0.00135 mm/y. Treatment of the material can hence be a constructive measure to decrease corrosion. [79]

The other surfaces face the cold bypass. Typically, corrosion can occur in the bypass as well due to humid air or more corrosive atmospheric conditions. However, the corrosiveness is expected to be significantly lower than the hot flow. As a simplified assumption, the corrosion rate is assumed to be zero.

3.2.4.2 Corrosion Rates in Tube Bundle Heat Exchanger

The TBHE is directly exposed to the exhaust gas. It contains multiple acid oxides, like SO_x, leading to a corrosive environment with pH-values between 3 and 6 [80]. Additionally, the temperature of the exhaust gas makes it prone to high-temperature corrosion. In the latter case, salt contaminants like Na_2SO_4 damage the protective surface oxides [81].

As the method to estimate the lifetime of a protective layer, as described in Section 2.4.1.2, relies on a lot of specific material data, which is not publicly available, the simplified method of a corrosion allowance is applied. Both flows in the heat exchanger are different. While the outer area of the tubes reacts with the exhaust gas, the inner area interacts with the water vapor. Two different corrosion rates are implemented to assess the total required corrosion allowance properly, one for each flow. The respective corrosion allowance is subtracted from the surface reacting with the set fluid.

However, literature on the corrosion rate of Inconel 625 in the exhaust gas and water vapor is sparse. A laboratory test of Inconel 625 in 80 °C sulfuric acid of 15 weight percent resulted in a corrosion rate of 0.19 mm/y [82]. A heat exchanger in a waste incineration plant operating with temperatures of 300 °C to 760 °C made of Inconel 625 showed a corrosion of less than 0.05 mm after 300 hours of exposure [83]. This equals a corrosion rate of 1.46 mm/year. A study on Inconel 625 in a Na_2SO_4, V_2O_5 molten salt environment, as commonly found in supercritical, oil-fired power generators, showed a corrosion rate of 0.135 mm/y at 700 °C at an exposure time of 120 h [84]. Corrosion rates of an Inconel 625 spray powder coating in a biomass-fired boiler were found to be 0.008979 mm/year on average at 550 °C and 0.408 mm/year at a temperature of 750 °C [85]. Another source derived a corrosion rate of Inconel 625 at 850 °C of 0.66 mm/year [86].

The corrosion behavior of Inconel 625 was investigated at 800 and 900 °C in an environment with 75 weight % Na_2SO_4 and 25 weight % K_2SO_4, which is typical for coal combustion. A corrosive mass change, MCA, of the Inconel specimen of $3.5 mg/cm^2$ and $6.5 mg/cm^2$ at 800 and 900 °C, respectively, and an exposure time exp. time of 120 hours has been experimentally derived [87]. Following Equation 3.12, the corrosion rates, CR, are derived to be 0.3027 mm/y for 800 °C and 0.5622 mm/y for 900 °C.

$$\mathrm{CR} = \frac{\mathrm{MCA}}{\rho \cdot \mathrm{exp.\ time}} \tag{3.12}$$

Similar findings have been derived for Inconel 625 in supercritical water of a sewage plant, which processes wastewater with a high concentration of inorganic salts leading to acidity at 500 °C. The corrosion rate is 0.1868 mm/year [88].

As the corrosion rates according to [87] and [88] are consistent with each other, they are used in this thesis. The temperature varies throughout the design mission of the engine. Therefore, the total acting corrosion rate varies as well. One corrosion rate is derived based on a linear accumulation of the corrosion rates required for each flight phase and their respective timeshare. The corrosion rates of the exhaust gas for each temperature are exponentially interpolated between the three corrosion rates found in [87] and [88].

The composition of the water vapor inside the tubes is yet to be investigated. As the water is recovered from the exhaust gas mixture, it could include corrosive components, which could condense as well. A more thorough investigation of the resulting condensed medium is required. However, this is beyond the scope of this thesis. Therefore, in this thesis, no corrosion is assumed from the water vapor in the tubes. Hence, the corrosion rate is assumed to be zero.

High temperature oxidation of Inconel 625 is low with 0.01 mm/y at a temperature of 982 °C [74]. As the operating temperature in the use case assumed in this thesis is significantly lower, high-temperature oxidation will be neglected.

3.2.5 Erosion

The erosion behavior is dependent on multiple input parameters. Some are known in preliminary design, like the material, the temperature and the occurring flow velocity. However, further parameters are unknown, including the impingement angle as well as the erosive medium and its occurring duration. Furthermore, erosion leads to a non-linear decrease in material thickness. No simple approximation has been found in the literature. The accuracy of the erosion prediction strongly depends on the assumptions for all the required parameters. A more thorough erosion investigation is required to derive dependable assumptions, e.g. by component erosion testing. However, this is beyond the scope of this thesis. While erosion can lead to significant decreases in material thickness, it can not be assessed using the methodology developed in this thesis.

3.2.6 Strength (Static Stress)

3.2.6.1 Stresses in Plate-fin Heat Exchanger focused on one Flow Passage

The method described below focuses on plain fins on one side of the flow. PFHE with no fins in both flows are rarely structurally integral due to the high bending stresses of the unreinforced plate. On the other hand, a PFHE with fins on both sides is difficult to structurally assess due to their more complex geometry and significant interactions between both sides. Especially thermal stresses, which are difficult to estimate, can lead to significant thermal stresses. In the case of the PFHE, the static stresses on the PFHE consist of pressure, temperature, and weight stresses. All types are superimposed. An exemplary PFHE passage is shown in Figure 3.4.

An easy, analytical solution is unfortunately not possible in this case. Using conventional plate theory, as described in [89, p. 508] only applies to unsupported plates. Here, the plates are supported by the fins. Methods used for sandwich plates with corrugated cores, like the homogenization method, as described in [90], convert the whole passage into one substitute plate. However, as the identical pressure gradient acts equally on both sides, no plate stress would result on the plate. Furthermore, [39] only offers design guidelines on reinforced, rectangular pressure containers

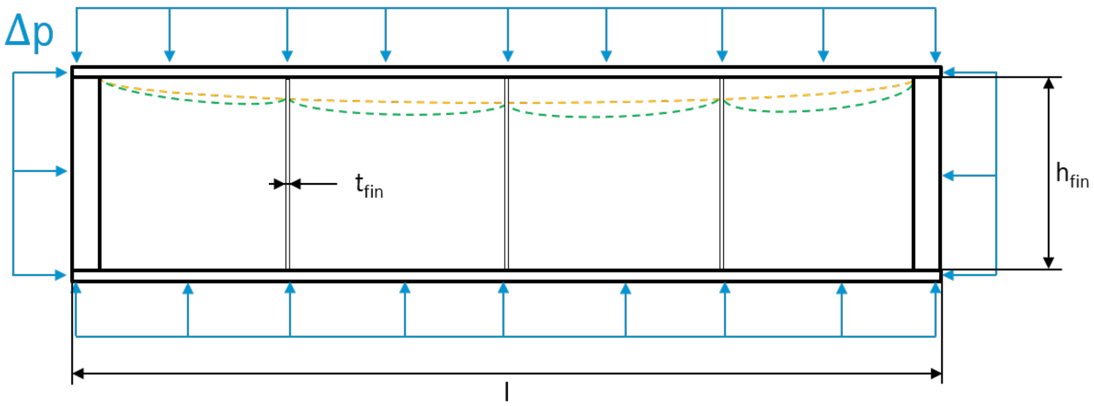

Figure 3.4: Graphical representation of one passage with assumed deformation of the plate (exaggerated for visualization)

or pressure containers separated by one single fin into two distinct cells. Both are not the case here. Therefore, a more detailed analysis is required. The structure, in general, is quite resistant to compression, assuming the fins do not buckle. This yields the first potential damage source, namely buckling in the fins. Furthermore, in case of a reverse pressure gradient, namely an overpressure on the finned side, the fins experience tensile stresses. Another potential damage source can result from the bending of the plate. The plate is assumed to bend due to the pressure as a whole as well as between two fins, leading to bending stresses. The sidebars are assumed to be significantly thicker and, therefore, yield no structural limitation. They are not assessed here. However, they lead to clamped boundary conditions on all four edges of the plate, as a cross-flow heat exchanger is assumed; thus, one sidebar is on every side of the plate. Therefore, the following damage sources will be analyzed in more detail below:

- Stresses in the plate due to bending, leading to yielding or rupturing of the material

- Compression on the fins leads to buckling or tensile stress leads to deformation of the fins

Plate Stresses In general, stresses in the plate are expected due to a shortening of the fins in compression, leading to a bending in the plate, shown in yellow in Figure

3.4. Additionally, bending occurs in each unit cell, leading to a second bending stress acting on the plate, as shown in green. If the pressure gradient changes sign, the bending stresses are assumed to be identical in magnitude and opposite in sign. For ductile materials, like Al6061 and Inconel 625, material properties can be assumed to be identical in compression and tension with sufficient accuracy [91]. Therefore, the calculation process does not change.

Bending Stress due to Shortening of the Fins The maximum deformation due to the shortening of the fins in compression allows the calculation of the bending stresses of the plate as a whole. According to Kirchhoff's plate theory, the maximum deflection is expected at the middle of the plate for the given clamped boundary conditions. All fins are substituted by one bar in the plate's center to estimate the plate's maximum deflection. This bar is under uniaxial compression, carrying the pressure and weight load acting on one fin. The plate is loaded by the pressure gradient and its weight. In the lower plate, the weight counteracts parts of the pressure bending. However, as the weight of one plate and its fins is much smaller than the pressure stress, this stress-reducing effect is neglected. The resulting substitute stress per fin, $\sigma_{\text{subst., fin}}$, can be calculated with Equation 3.13.

$$\sigma_{\text{subst., fin}} = \frac{F_{\text{pressure}} + F_{\text{weight}}}{A_{\text{fin, passage}}} \tag{3.13}$$

The area, $A_{\text{fin, passage}}$, refers to the crosssectional area of all fins in one passage in the plane perpendicular to the pressure, as seen in Equation 3.14.

$$A_{\text{fin, passage}} = FD_i \cdot l_{\text{plate}} \cdot t_{\text{fin}} \cdot w_{\text{plate}} \tag{3.14}$$

FD_i is the fin density of the passage analyzed, and w_{plate} is the length in the flow direction of the passage.

F_{pressure} is the equivalent total pressure force acting on the plate. It can be calculated according to Equation 3.15.

$$F_{\text{pressure}} = \Delta p \cdot l_{\text{plate}} \cdot w_{\text{plate}} \tag{3.15}$$

The weight force can be calculated by calculating the mass of one plate, m_{plate}, and the mass of the fins of one passage, m_{fin}. The masses can be calculated similarly to Section 3.2.2, as shown in Equations 3.16 and 3.17.

$$m_{\text{plate}} = l_{\text{plate}} \cdot w_{\text{plate}} \cdot t_{\text{plate}} \cdot \rho_{\text{plate}} \tag{3.16}$$

$$m_{\text{fin}} = l_{\text{plate}} \cdot h_i \cdot t_{\text{fin,i}} \cdot w_{\text{plate}} \cdot \text{FD}_i \cdot \rho_{\text{plate}} \tag{3.17}$$

The weight from the passages above and below are assumed to be carried by the sidebars and have thus no influence on the plate's behavior. In this first assessment, no loads due to maneuvers are assessed. Therefore, no load factor is introduced. The load of each fin is assumed to be carried half by the plate above and half by the plate below the fin. F_{weight} can then be calculated according to Equation 3.18.

$$F_{\text{weight}} = (m_{\text{plate}} + 0.5 \cdot m_{\text{fin}}) \cdot g \tag{3.18}$$

Applying basic mechanical knowledge, the displacement, δ_{bar}, can be calculated using Equation 3.19.

$$\delta_{\text{bar}} = \sigma_{\text{subst., fin}} \cdot \frac{0.5 \cdot h_{\text{fin}}}{E} \tag{3.19}$$

Following Kirchhoff's plate theory, the stress in the plate clamped at all ends can be calculated using Equation 3.20. [89, p. 508]

$$\sigma_{\text{max,plate}} = \frac{-\beta_1 \cdot q \cdot b^2}{t_{\text{plate}}^2} \tag{3.20}$$

β_1 is analytically derived for different ratios $1 \leq a/b \leq 2$ and can be cubically interpolated for values between 1 and 2 using Equation 3.21. For higher values, $\beta_1 = 0.5$ can be assumed.

$$\beta_1 = 0.106 \cdot (a/b)^3 - 0.683 \cdot (a/b)^2 + 1.495 \cdot (a/b) - 0.61 \tag{3.21}$$

a is the length of the long edge, and b is the length of the short edge. The maximum deflection, $y_{\max} = \delta_{\text{bar}}$ can be calculated using Equation 3.22.

$$y_{\max} = \frac{\alpha_p \cdot q \cdot b^4}{E \cdot t_{\text{plate}}^3} \tag{3.22}$$

Like β_1, α_p is another coefficient analytically derived for different ratios $1 \leq a/b \leq 2$. Using values from [89, p. 508], it can be interpolated by Equation 3.23 for values until 2. For higher values, $\alpha_p = 0.0284$ holds.

$$\alpha_p = 0.005 \cdot (a/b)^3 - 0.035 \cdot (a/b)^2 + 0.084 \cdot (a/b) - 0.04 \tag{3.23}$$

Transforming Equations 3.20 and 3.22 and substituting q into each other leads to Equation 3.24. It calculates the maximum stress, $\sigma_{\text{max. bending, plate}}$, in the plate due to compression of the fins.

$$\sigma_{\text{max. bending, plate}} = \frac{-\beta_1 \cdot \delta_{\text{bar}} \cdot E \cdot t_{\text{plate}}}{b^2 \cdot \alpha_p} \tag{3.24}$$

According to Kirchhoff's plate theory, the maximum stress is expected at the center of the long side [89, p. 508].

Bending Stress in Unit Cell The second stress adding to the bending stresses due to the deformation of fins is the stress that occurs due to the bending of the plate in the unit cell, called the plate segment hereafter. A unit cell here is defined as one section limited by two fins right and left and the plate on top and bottom. The dimensions of the plate segment are defined as $1/FD$ and w_{plate}. Hence, the plate segment is limited by the fins in one dimension and the sidebars in the other dimension. All edges of the plate segment are assumed to be clamped, as they are typically connected by brazes. Similar to the procedure above, the maximum bending stress in the plate segment occurs due to a combination of weight and pressure differences. However, only the weight of the plate segment is taken into account here. The loading is distributed equally across the whole plate. Therefore, the uniform load, q_{load}, is defined as

$$q_{\text{load}} = \Delta p + \frac{(m_{\text{plate}} + 0.5 \cdot m_{\text{fin}}) \cdot g}{l_{\text{plate}} \cdot w_{\text{plate}}} \tag{3.25}$$

Applying the dimensions of the plate segment and Equations 3.20 and 3.21, the maximum stress of the plate segment, $\sigma_{\text{max, plate segment}}$ can be calculated. It is supposed to act at the center of the long side of the plate segment.

The maximum stress of both the bending of a plate segment and of the plate as a whole occurs at the center of the long side. For a unit cell close to the sidebar, both maximum stresses can occur at the same location if the plate segment is limited by the sidebar and a fin. No apparent conversion factor can be derived for other configurations. For conservatism, both maximum stresses are therefore assumed to act at the same position independent of the geometry.

Temperature Stress in Plate The last component of the stress calculation in the plate is the temperature stress occurring due to a difference in wall temperature between the inner fin region and the outer unfinned region. In this thesis, only temperature gradients through the thickness of the plate are investigated. In reality, the temperature in flow direction varies, leading to a 2-dimensional temperature field on the plate.

For a flat plate with all edges fixed, the maximum resulting bending stress due to a linear temperature gradient between both faces of the plate can be calculated using Equation 3.26 [89, p. 760].

$$\sigma_{\text{plate, T, max}} = \frac{\frac{1}{2} * \Delta T \cdot \alpha \cdot E}{1 - \nu} \tag{3.26}$$

ΔT is the temperature difference between both faces, α the temperature expansion coefficient, E the elastic modulus and ν the Poisson's ratio. As temperature stresses occur due to restricted elongation, the maximum temperature stress acts at the location that is constrained the most: this is the connection of the plates to the sidebars, as the sidebars are assumed to be significantly thicker than the fins. The bending stress acts in compression on the hot face and in tension on the cold face of the wall. As each plate features a hot and a cold face, the temperature stress acts in the same direction as the bending stresses, either at the hot or at the cold face. Hence, the total superimposed stress is increased.

Total Stress in Plate The total stress in the plate can be calculated by superimposing all stresses:

$$\sigma_{\text{plate, max}} = \sigma_{\text{max. bending, plate}} + \sigma_{\text{max, plate segment}} + \sigma_{\text{plate,T ,max}} \tag{3.27}$$

This stress is compared to the yield strength, $\sigma_{R_{p0,2}}$, and UTS of the material, allowing the calculation of factors of safety.

Buckling In the example shown in Figure 3.4, the fins are loaded in compression. Therefore, fin buckling has to be investigated.

This thesis focuses on plain fins. One fin is characterized by the fin length w_{plate} the fin height h_{fin} and the fin thickness t_{fin}. The flow length w_{plate} is much greater than the height of a flow channel h_{fin}. Analytical solutions for the critical buckling stress σ_{cr} of a plate clamped at all edges typically follow the form described in Equation 3.28 [89, p. 730].

$$\sigma_{cr} = K * \frac{E}{1-\nu^2} * (\frac{t_{\text{plate}}}{b})^2 \tag{3.28}$$

The buckling coefficient, K, for a plate clamped at all edges, similar to the fins, is only defined for $\frac{a}{b} >= 1$, with a being the longer side and b being the shorter side, where the compressive load acts. However, typically in PFHE with plain fins the compressive load acts on the long side, which would lead to $\frac{a}{b} \ll 1$. As no coefficient K is given for these values, the fins are assumed to act as a bar under biaxial compression fixed on both ends. The critical buckling force F_{cr} can be calculated using Equation 3.29 [89, p. 718].

$$F_{cr} = K * \frac{\pi^2 * E * I}{h_{fin}^2} \tag{3.29}$$

The buckling coefficient, K, is four in this case. I_{plate} is the minimum area moment of inertia resisting the buckling.

$$I_{\text{plate}} = min((h_{fin} * t_{fin}^3)/12; (h_{fin}^3 * t_{fin})/12 \tag{3.30}$$

The resulting critical buckling force F_{crit} can then be compared to the occurring force on one fin, $F_{fin} = \sigma_{\text{subst., fin}} \cdot t_{fin} \cdot w_{\text{plate}}$ with $\sigma_{\text{subst., fin}}$ derived from Equation 3.13.

Plastic Deformation of Fins under Tension If the pressure difference acts in the opposite direction than shown in Figure 3.4, the fins are under tension. Therefore, the occurrence of plastic deformation under tension has to be investigated.

The maximum displacement of the fins has been derived in Section 3.2.6.1. However, this elongation reflects only the upper or lower side of the passage, as it is the deformation caused by the pressure gradient acting on one plate. The maximum elongation has to be doubled to account for the elongation on both sides. Its related strain, $\epsilon_{\text{fin, max}}$ can be calculated using Equation 3.31.

$$\epsilon_{\text{fin, max}} = \frac{2 \cdot \delta_{\text{bar}}}{h_{\text{fin}}} \tag{3.31}$$

No plastic deformation is allowed, as it would induce persisting changes in the geometry as well as alternate material properties, which are difficult to predict. Therefore, the resulting strain is then compared to the strain at yielding, ϵ_{yield}, which can be calculated using Equation 3.32, following Hooke's Law, as it is valid for the elastic region.

$$\epsilon_{\text{yield}} = \frac{\sigma_{R_{p,0.2}}}{E} \tag{3.32}$$

By comparing both ϵ values, the factor of safety against plastic deformation of the fins can be derived.

3.2.6.2 Stresses in Plate-Fin Heat Exchanger using Homogenization Method

A second approach involves focusing on the PFHE structure as a whole. The approach is outlined in Figure 3.5. It assumes the substitution of the finned flow passages by plates with orthotropic, equivalent properties. These properties can be derived using analytical formulas. Then, after conducting a simplified FEM analysis with the substitute model, magnification factors are used to derive the local stresses

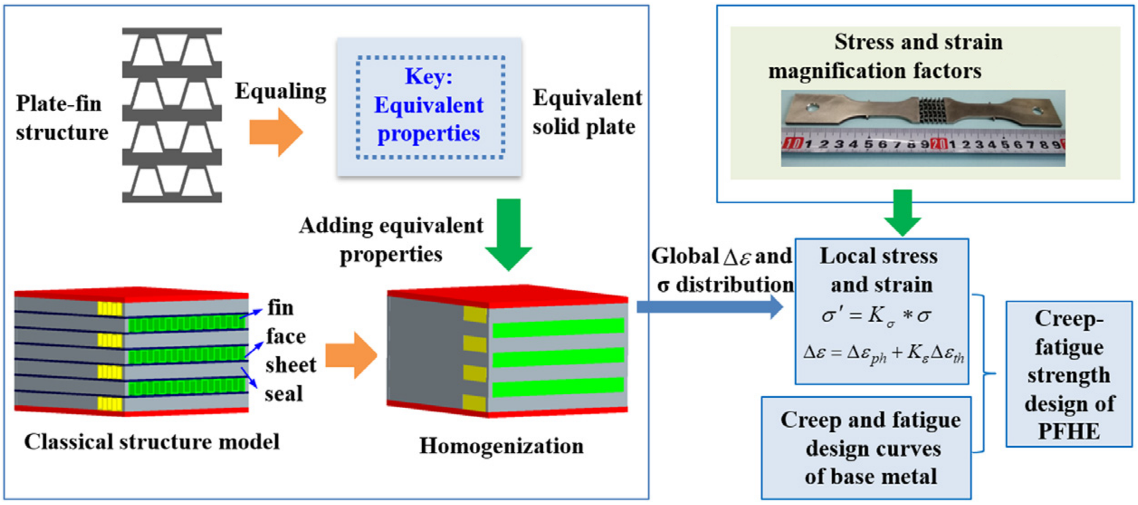

Figure 3.5: Homogenization method, as explained in [11], from [12].

from the stresses derived by the substitute model. [11] The equivalent properties can be calculated, as described in [11]. The respective coordinate systems need to be treated carefully when utilizing a cross-flow heat exchanger. To keep consistency in one global coordinate system, the respective parameters need to be converted according to Figure 3.6. A parameter $P_{d/D,i}$ denotes a parameter in the local direction d or global direction D of flow i.

The local coordinate system of flow one is not rotated compared to the global coordinate system. Therefore, $P_{D,1} = P_{d,1}$.

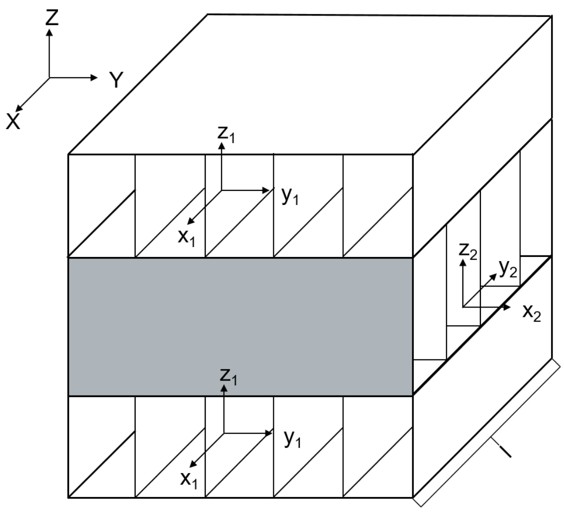

Figure 3.6: Local and global coordinate systems in different flows.

In flow two, the local coordinate system is rotated by 90 °around the Z-axis. Therefore,

$$P_{X,2} = P_{y,2} \tag{3.33}$$
$$P_{Y,2} = P_{x,2} \tag{3.34}$$
$$P_{Z,2} = P_{z,2} \tag{3.35}$$
$$P_{XY,2} = P_{xy,2} \tag{3.36}$$
$$P_{XZ,2} = P_{yz,2} \tag{3.37}$$
$$P_{YZ,2} = P_{xz,2} \tag{3.38}$$

holds. Using the equations derived in [11] and stated in [12], substitute material properties for an equivalent, homogenized model are derived.

The homogenization method can be utilized to simplify FEM analyses, e.g. for verification purposes. However, it is not further used within this thesis.

3.2.6.3 Tube Bundle Heat Exchanger

The strength of the tubes against static load conditions due to steady flow can be calculated using three different methods. One method uses empirical formulas to calculate the required wall thickness due to a pressure load and the resulting stress in the tube due to temperature and pressure stresses. It follows the industry norm DIN EN 13445-3, as described in [56]. A second method employs an adaption made by Lame to the vessel formula of thin vessels. It is validated against a FEM analysis and described in [92]. Grieb ([20]) presents a third method to estimate the occurring stresses in a heat exchanger similar to the one described in Figure 2.7.

Calculation of Static Stress according to DIN EN 13445-3 The DIN EN 13445-3 defines construction guidelines for unfired pressure vessels made of steel. Additional requirements for pressure vessels made of aluminum are described in [93].

Stress Intensification Factor due to Bends The following calculation refers to straight, thin-walled cylindrical unfired pressure vessels. However, in our case, the tubes are bent at both ends. Bends usually increase the stresses occurring in the tube. A stress intensification factor is introduced. It utilizes equations from DIN EN 13380, which is used for metallic industrial piping. [94, pp.257-259] The stress intensification factor of a tube bend, k_i can be calculated using Equation 3.39.

$$k_i = \frac{0.9}{k_h^{\frac{2}{3}}} \tag{3.39}$$

k_h is the form factor of the bend. It depends on geometric properties and can be calculated with Equation 3.40.

$$k_h = \frac{4 \cdot SL \cdot t_t}{((d_{inner} + d_{outer})/2)^2} \tag{3.40}$$

Depending on the bend radius, inner diameter, and tube thickness, the stress intensification factor calculated using the equations above can sometimes fall below 1 for a given configuration. This implies that a curved tube may experience lower stresses than a straight tube, which is not realistic and is likely a consequence of the simplified form of the equation. Stress intensification factors below 1 are particularly observed for combinations of small inner diameters, large thicknesses, and large bend radii. In such cases, the stress distribution is likely to be more uniform and comparable to that of a straight tube.

For a straight tube, the stress intensification factor is always assumed to be $k_i = 1$, regardless of the geometry. TBHE typically incorporate both straight and curved tubes. Therefore, even if a bend would result in lower stresses than a straight tube, the stress intensification factor is assumed to be at least 1 in all cases.
The derived stress intensification factor is applied to all stresses.

Stresses due to Pressure The required wall thickness of a straight cylinder, $t_{t,\text{required, straight}}$, due to an inner overpressure, can be calculated using Equation 3.41.

The equation is valid for $\frac{d_{outer}}{d_{inner}} \leq 1.7$. In a heat exchanger, thin wall thicknesses are expected, and therefore, $\frac{d_{outer}}{d_{inner}} \leq 1.7$ should always hold. [56]

$$t_{t,\text{required, straight}} = \frac{p \cdot d_{outer}}{2 \cdot f_d \cdot k_z + \Delta p} \tag{3.41}$$

Applying the previously derived stress intensification factor, k_i, yields

$$t_{t,\text{required, bend}} = \frac{p \cdot d_{outer}}{k_i \cdot 2 \cdot f_d \cdot z + k_i \cdot \Delta p} \tag{3.42}$$

Δp results from the pressure difference between both flows inside and outside the tube. k_z is a welding factor accounting for the weakening of the tube. It depends on the inspectionability of the component. In this thesis, the tubes are assumed to be testing group 3, meaning the material can be tested non-destructively [95]. This yields a welding factor, z, of 0.85. f_d represents the usable design conditions of the material. Inconel 625 is an austenitic steel with a minimum fracture elongation of 30 %. Therefore, f_d can be calculated using Equation 3.43 [56].

$$f_d = \frac{R_{p,1.0/T}}{1.5} \tag{3.43}$$

As literature data for Inconel 625 only provides the temperature-dependent yield strength (indicated by a T) at 0.5 % plastic elongation $R_{p,0.5/T}$, it is used instead. This yields slightly more conservative results.

The resulting required thickness in the bends is compared to the actual thickness to derive the factor of safety against tube bursting due to the pressure. This gives an initial assessment of the tube. However, typically temperature stresses occur as well. Furthermore, the tube should not deform plastically. Therefore, a more thorough assessment is required, leading to factors of safety due to combined temperature and pressure stresses against yielding and rupture. While the above-explained calculation method provides a first estimation, the more thorough calculation method presented below is used in this thesis.

Combined Temperature and Pressure Stresses Additional stresses due to the temperature difference between the inside and outside of the tube occur. These stresses can be characterized by Equation 3.44 [56], *inner* indicating the stress at the inner wall and *outer* the stress at the outer wall. α describes the thermal expansion coefficient of the material. The temperature difference between the outer and the inner wall is defined as $T_{outer} - T_{inner}$. ν is the Poisson's ratio.

$$\begin{aligned} \sigma_{T_{inner}} &= \frac{\alpha}{2} * \frac{E}{1-\nu} * (T_{outer} - T_{inner}) * \frac{3 * d_{outer} + d_{inner}}{2 * (d_{outer} + d_{inner})} \\ \sigma_{T_{outer}} &= -\frac{\alpha}{2} * \frac{E}{1-\nu} * (T_{outer} - T_{inner}) * \frac{d_{outer} + 3 * d_{inner}}{2 * (d_{outer} + d_{inner})} \end{aligned} \tag{3.44}$$

The maximum static stress combining thermal and pressure stresses can be calculated using Equation 3.45 [56]. It is the maximum of both the stress at the inner wall as well as at the outer wall.

$$\sigma_{\max} = \max\left[\left(\frac{p * (d_{outer} + t_t)}{2.3 * t_t} + \sigma_{T_{inner}}\right), \left(\frac{p * (d_{outer} - 3 * t_t)}{2.3 * t_t} + \sigma_{T_{outer}}\right)\right] \tag{3.45}$$

Applying the stress intensification factor, k_i, to the maximum static stress of the tube and comparing it to yield and ultimate tensile strength yields the factors of safety according to DIN EN 13445.

Calculation of Static Stress according to Lames Vessel Formula In a second approach, the pressure and temperature stresses are also superimposed. However, an explicit analytic formula for the pressure stress is used. The resulting equivalent stress is derived using either the Tresca criterion or the von Mises criterion. The maximum stress occurs at the inner wall of the tube. The equations stated beneath are validated against a FEM analysis. [92]

The following Equations 3.46 and 3.47 describe the pressure loading of a thin, high-pressure heater tube at a radius r in the wall in the circumferential and radial direction, respectively [92]. For better readability, in this section the indices i and o refer to the inner and outer walls of the tube, respectively.

$$\sigma_{\theta,p}(r) = \frac{p_i * r_i^2 - p_o * r_o^2}{r_o^2 - r_i^2} + \frac{(p_i - p_o) * r_i^2 * r_o^2}{(r_o^2 - r_i^2) * r^2} \tag{3.46}$$

$$\sigma_{r,p}(r) = \frac{p_i * r_i^2 - Pp_o * r_o^2}{r_o^2 - r_i^2} - \frac{(p_i - p_o) * r_i^2 * r_o^2}{(r_o^2 - r_i^2) * r^2} \tag{3.47}$$

Equations 3.48 and 3.49 describe the temperature stress at a radius r in the wall in the circumferential and radial direction, respectively.

$$\sigma_{\theta,T}(r) = \frac{E * \alpha * (T_o - T_i)}{2 * \ln(\frac{r_o}{r_i})} * (\frac{r_o^2}{r_o^2 - r_i^2} * (1 + \frac{r_i}{r}) * \ln(\frac{r_o}{r_i}) - \ln(\frac{r}{r_i}) - 1) \tag{3.48}$$

$$\sigma_{r,T}(r) = \frac{E * \alpha * (T_o - T_i)}{2 * \ln(\frac{r_o}{r_i})} * (\frac{r_o^2}{r_o^2 - r_i^2} * (1 - \frac{r_i}{r}) * \ln(\frac{r_o}{r_i}) - \ln(\frac{r}{r_i})) \tag{3.49}$$

A temperature field in the axial direction is expected, as well. However, its shape and magnitude are unknown. Furthermore, the shape of the tubes, featuring a U-bend at the end, allows them to elongate more freely in the axial direction if there is no intermediate clamping in the straight tube parts. Therefore, in the first assessment, no axial temperature stresses are assumed. Hence, the stress in the axial direction is assumed to be 0; $\sigma_z = 0$.

Next, the stresses in both circumferential and radial directions are superimposed. Principal stresses can be derived using Equations 3.50, 3.51 and 3.52 [92].

$$\sigma_1(r) = \sigma_\theta(r) = \sigma_{\theta,p}(r) + \sigma_{\theta,T}(r) \tag{3.50}$$

$$\sigma_2 = \sigma_z \tag{3.51}$$

$$\sigma_3(r) = \sigma_r(r) = \sigma_{r,p}(r) + \sigma_{r,T}(r) \tag{3.52}$$

The resulting, equivalent stress state can be calculated using the Tresca-criterion according to Equation 3.53.

$$\sigma_{\text{Tresca}}(r) = \sigma_1(r) - \sigma_3(r) \tag{3.53}$$

The Tresca criterion is generally regarded as more conservative than the von Mises equivalent stress [96]. However, the von Mises criterion is more applicable to ductile material, which is used in this thesis [97, p. 74f.] Therefore, the von Mises equivalent stress is computed as well, following Equation 3.54.

$$\sigma_{\text{Mises}}(r) = \sqrt{\frac{(\sigma_1(r) - \sigma_2)^2 + (\sigma_2 - \sigma_3(r))^2 + (\sigma_3(r) - \sigma_1(r))^2}{2}} \tag{3.54}$$

The stress intensification factor, k_i, is applied to the maximum stress for all radii r:

$$\sigma_{\text{Mises/Tresca, bend}}(r) = k_i \cdot \sigma_{\text{Mises/Tresca}}(r) \tag{3.55}$$

It is then compared to the material properties, like the yield strength and UTS, to derive the factors of safety.

Calculation of Static Stress according to Grieb Furthermore, the maximum stress of the heat exchanger described in [5] can be calculated by Equation 3.56. [20]

$$\sigma_{\text{max}} = 8.5 * \Delta p \tag{3.56}$$

Δp is the pressure gradient acting on the tube.

3.2.7 Low Cycle Fatigue (LCF)

The calculation methods proposed in [39] are valid for pressure vessels operated in the elastoplastic regime, as in this thesis. Maximum occurring stresses are below the yield strength of the material. As creep is not considered in the fatigue calculation method, creep-fatigue interaction will be investigated later. The structural assessment for fatigue follows multiple steps, as described in [98]. First, the acting stresses need to be defined. Then, the fatigue strength of the geometry can be derived from the Wöhler-Diagram. Finally, it is compared to the acting stresses, and a safety factor is calculated.

3.2.7.1 Definition of Acting Stress

To assess LCF, the mission profile, including its different load cases, needs to be modeled. Usually, this data is derived from actual missions. However, as no detailed knowledge of the mission profile exists yet, it is simplified in this thesis. Each flight mission consists of the relevant mission points. These include MTO, the maximum-climb condition (MCL), and the cruise condition. Figure 3.7 shows exemplary mission profiles of the PFHE and the TBHE.

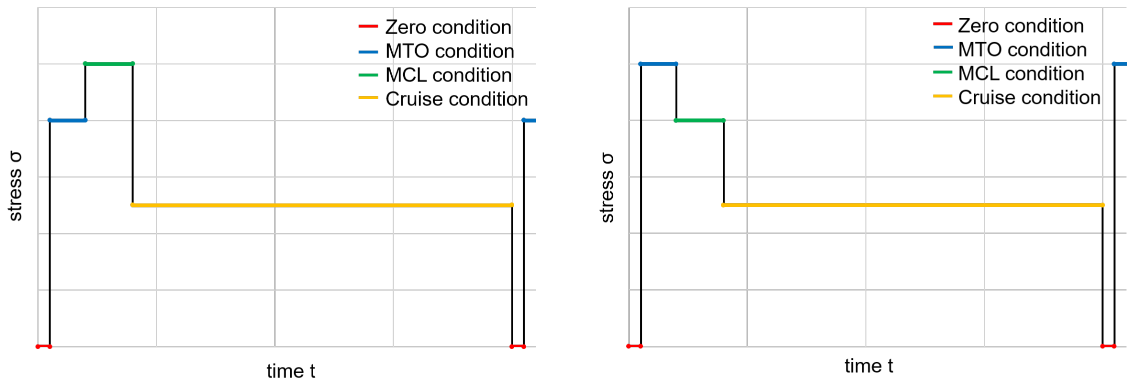

a) PFHE mission profile

b) TBHE mission profile

Figure 3.7: Exemplary mission profile of both heat exchangers with the relevant mission points

As can be seen, the mission point of maximum stress differs between both heat exchanger types. However, both mission profiles show one clear stress peak without intermediate cycles. Therefore, one cycle is defined as the difference between zero loading and maximum stress mission points. For the PFHE, this mission point is the MCL condition, while for the TBHE it is the MTO condition. The differences result from different pressure gradients at different mission points during the operation of both heat exchanger types.

As only stationary data is available during the preliminary design stage, transient behavior is estimated by using a correction factor of 1.1. This is consistent with [5], which found an increase of the maximum stationary stress by 10 % during transient behavior.

Every cycle is described by its mean stress σ_m, and its stress amplitude, σ_a, as seen in Figure 3.8. For LCF, Table 3.1 shows the respective acting stresses.

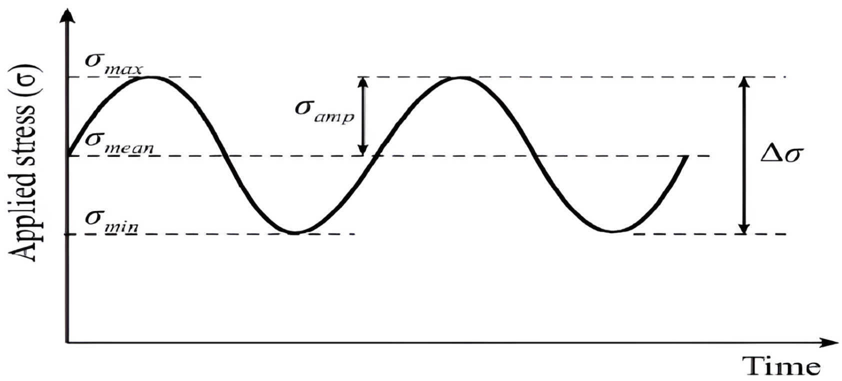

Figure 3.8: Cycle showing mean stress and stress amplitude, from [13]

HX type	σ_{min}	σ_{max}	σ_{mean}	σ_{amp}
PFHE	0	σ_{MCL}	$\frac{\sigma_{MCL}}{2}$	$\frac{\sigma_{MCL}}{2}$
TBHE	0	σ_{MTO}	$\frac{\sigma_{MTO}}{2}$	$\frac{\sigma_{MTO}}{2}$

Table 3.1: Description of LCF cycle

The material data typically involves tests with zero mean stress, meaning the stress amplitude is applied alternatingly in tension and compression. However, in our mission parameters, the mean stress is not zero. Therefore, a conversion needs to be applied. However, this formula assumes zero mean stress. In practice, often, an amplitude acts on top of a non-zero mean stress. Using the Goodman linear model, as explained in Section 2.4.5.2, the load condition can be transposed to a zero mean stress load by Equation 3.57. [64]

$$\sigma_{\text{acting, zero-mean}} = \frac{\sigma_{\text{acting}}}{\left(1 - \frac{\sigma_m}{\text{UTS}}\right)} \tag{3.57}$$

3.2.7.2 Stress-Life Curve

When using the stress-life method, the allowable stress, a material property, must be derived.

Plate-Fin Heat Exchanger Fatigue properties of aluminum 6061-T6 have been derived from the resulting hyperbolic allowable stress amplitude curve presented in [64] and shown in Equation 3.59. It involves interpolated measurement values for zero mean stress without any knockoff factors. A temperature correction factor k_T according to [73] is used to adjust these values for the elevated temperature levels between 0 and 200 °C. It is described in Equation 3.58 with the temperature T in °C as input.

$$k_T = 1 - 1.2 \cdot 10^{-3} \cdot (T - 50) \tag{3.58}$$

$$\sigma_{\text{allow., zero-mean}} = k_T \cdot \epsilon \cdot E = k_T \cdot (\frac{14479000000}{\sqrt{N}} + 96500000) \tag{3.59}$$

Transforming Equation 3.59 allows the determination of the maximum allowable number of cycles for a given zero-mean stress $\sigma_{\text{allow., zero-mean}}$.

$$N = \left(\frac{14479000000}{\frac{\sigma_{\text{allow., zero-mean}}}{k_T} - 96500000} \right)^2 \tag{3.60}$$

To derive the number of allowable cycles for a given load condition N_j, $\sigma_{\text{allow., zero-mean}}$ is set equal to $\sigma_{\text{acting, zero-mean}}$. The number of cycles becomes negative for zero mean stresses lower than 96.5 MPa. This stems from the fatigue data approximation used in [64]. Here, 96.5 MPa is assumed to be the stress at the endurance limit. No further reduction in fatigue strength is expected after the endurance limit. Especially for aluminum, however, this is not the case. Aluminum features a face-centered cubic crystal structure, allowing greater slip systems compared to the body-centered cubic structure of many steels. However, for simplification, the convention of an endurance limit used for many steels is applied. The resulting number of cycles is set to the endurance limit in case of a zero mean stress below 96.5 MPa to be conservative.

Tube Bundle Heat Exchanger Data for the TBHE can be found in [74]. A linear interpolation is applied to obtain the fatigue behavior at the acting temperature.

3.2.7.3 Derivation of Total Damage

The damage can be derived by comparing the allowable number of cycles, N, to the occurring number of cycles, n_{cycles}, as shown in Equation 3.61.

$$D_{\text{LCF}} = \frac{n_{\text{cycles}}}{N} \tag{3.61}$$

Equation 3.61 assumes only one load peak per cycle (MCL and MTO, respectively). If another load peak exists, e.g., if the occurring loads during thrust reverse are accounted for and they would be higher than the load during the cruise, the damage can be assessed using Miner's linear damage rule. However, in this thesis, only one load peak is expected.

3.2.8 High Cycle Fatigue (HCF)

The Eigenmodes of the respective components are required to properly assess HCF. However, they are typically unknown in the preliminary design stage. Therefore, a simplified approach is used. The design goal for components, where HCF is expected, is the endurance of the respective components. This thesis applies a lump sum alternating stress to the mean stress. In this case, the mean stress and alternating stress can be described by Equations 3.62 and 3.63 with σ_a being an estimation of the occurring stresses due to, e.g., flow instabilities or vibrations.

$$\sigma_m = \sigma_{\text{cruise}} \tag{3.62}$$

$$\sigma_a = \sigma_a \tag{3.63}$$

The stress occurring during the cruise is used as a baseline, as it accounts for the longest timeshare.

Typical values of stress amplitude due to oscillations in a gas turbine blade are 50-100 MPa [99, p.11]. The resulting stress amplitude depends significantly on the geometry as well as the acting flow. However, as no other data is currently available, a stress amplitude of 50 MPa is assumed as a first estimation. The influence of different stress amplitudes is further investigated in Section 4.2.5.

The resulting load condition of σ_m and σ_a corresponds to a point in the Goodman diagram, as shown by the cross in Figure 3.9.

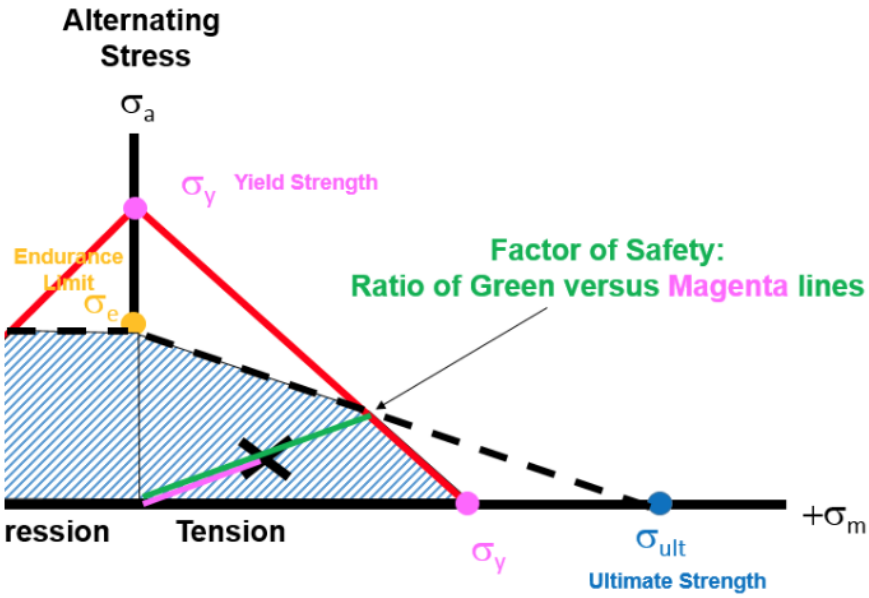

Figure 3.9: Modified Goodman-Haigh diagram for infinite life, from [14]

Besides the shown Goodman-line, a second line is created by connecting the yield strength points on the mean stress and the alternating stress axis. This line is mostly relevant to avoid yielding at low stress amplitudes and high mean stresses. To calculate the safety factor, the distance to the point of the load condition, shown in magenta, is compared to the minimum distance from the origin to either the Goodman line or to the yield envelope, as shown in green. It represents the limiting line to failure before reaching the endurance limit. Dividing both yields the factor of safety HCF.

3.2.9 Creep

Creep occurs at higher temperatures T, where $T > 0.3 * T_{mt}$ with T_{mt} being the absolute melting temperature [100, p. 391]. Table 3.2 provides an overview of the materials assumed in this thesis and the corresponding minimum temperatures for creeping to occur.

HX type	**Material**	**Melting point region** T_{mt}	$0.3 * T_{mt}$
PFHE	Al6061-T6	582 - 651.7 °C [72]	174,6 - 195.51 °C
TBHE	Inconel 625	1290 - 1350 °C [74]	387 - 405 °C

Table 3.2: Melting temperature and critical temperature for the occurrence of creeping of both HXs

As the PFHE's main task in the WET concept application example is the condensation of the fluid, maximum temperatures are assumed to stay around the boiling temperature of the water. The boiling temperature decreases with decreasing pressure and hence increasing altitude. Therefore, maximum temperatures are assumed to be around 100 °C, which is well below 174.6 °C. Therefore, no significant creep is expected in the condenser.

In the TBHE, temperatures are significantly higher due to its task to superheat the vapor. Therefore, creep is expected to occur, and a more thorough analysis is necessary.

The following assessment procedure follows common industry standard DIN EN 13445 [39]. It specifies two methods: one, where one load case is assumed throughout the whole lifetime, and another, which adds different load cases together. The latter assessment method is chosen because temperature and pressure levels can change significantly during the flight. Therefore, each mission point is assessed separately and then combined.

This approach first requires a definition of flight phases, including the acting stresses, f_j, temperatures, T_j, and the time spent for each flight phase, t_j.

The occurring stresses at a given wall thickness are calculated at all different load cases. From these stresses, the time until creep rupture, as well as the time until reaching the 1 % elongation limit, are calculated. These periods are compared to the time spans allowable by the material and linearly summed up. The result indicates if the wall thickness needs to be higher, is sufficient, or may be reduced.

3.2.9.1 Definition of Nominal Stress

Assuming we cannot sufficiently monitor the remaining lifetime, as we do not want to continuously inspect the HXs due to cost, the nominal stress allowed by the material, f, can be described by Equation 3.64 [39].

$$f = \min\left[f_{nc,j}; \frac{R_{m/T/t}}{SF}; R_{p1,0/T/t}\right] \tag{3.64}$$

$f_{nc,j}$ is the allowable stress of a given load case j based on the time-independent material properties. It is described as the maximum of the design condition f_d, as described in Section 3.2.6.3, or a different design condition based on chosen safety factors.

3.2.9.2 Determination of Creep Rupture Strength and Yield Limit

Subsequently, the creep rupture strength, $R_{m/T/t}$, and the yield limit $R_{p1,0/T/t}$ at a given temperature and duration must be calculated. Data is provided as mean data of multiple tests. As no continuous values for the creep behavior of Inconel 625 are provided in the literature, the available values are interpolated. The actual acting temperature and the time periods usually differ from values found in the literature. Therefore, an interpolation is required for both temperature and time span. Two methods are commonly mentioned in literature for this.

The first method, described in [39], interpolates the values towards the occurring temperature first. The derived values will then be interpolated towards the correct time span. Here, two distinct calculation steps are required. For a temperature difference between available information on creep behavior, $T_1/2$, and the real temperature occurring, T, Equations 3.65 and 3.66 can be used [39]. Indices 1 and 2 indicate the next lower and higher available data point.

$$R_{T/t} = R_{T_1/t} * \left(\frac{R_{T_2/t}}{R_{T_1/t}}\right)^{Z_R} \tag{3.65}$$

with

$$Z_R = \frac{log(T) - log(T_1)}{log(T_2) - log(T_1)} \tag{3.66}$$

A second method for estimating the creep rupture strength involves using the so-called Larson-Miller Parameter, LMP. As seen in Equation 3.67, it simplifies the interpolation by combining temperature and time span into one parameter, the LMP.

$$LMP = T * (\log(t) + C) \tag{3.67}$$

C is the material-specific Larson-Miller constant. For Inconel 625, C is 27.3. [101]

Both methods are valid in our use case. However, as the material data for Inconel 625 found in the literature would not lead to a good representation of the LMP-curve, the first method, according to DIN EN 13445, is used.

Now, the actual acting stress of each load case, f_i, is compared to the nominal stress of each load case, f. If it is larger in any of the load cases, the wall thickness must be increased. If the wall thickness is large enough, the resulting time until creep rupture and the time until reaching a 1% elongation can be calculated.

3.2.9.3 Time until Creep Rupture and reaching the Yield Limit

As mentioned, the creep curve is only given for certain combinations of nominal stresses and temperature. Therefore, a second interpolation is applied to determine the maximum time until creep rupture and until reaching the yield limit. For each load case, f_i, at a given temperature T_i, the time until creep rupture, t_{R,f_i,T_i} can be calculated with Equation 3.68. [39]

$$t_{R,f_i,T_i} = t_A * (\frac{t_B}{t_A})^{Y_R} \tag{3.68}$$

with Y_R being the interpolation factor, defined by Equation 3.69.

$$Y_R = \frac{\log(f_i) - \log(f_{R,t_A})}{\log(f_{R,t_B}) - \log(f_{R,t_A})} \tag{3.69}$$

A and B with their respective lifetimes and nominal stress indicate the nearest, given values from material data compared to the actual, acting stress of each load case, which satisfy Equation 3.70. [39]

$$f_{R,t_A} \leq f_i \leq f_{R,t_B} \tag{3.70}$$

Suppose the occurring stress of the load case, f_i, corresponds to a stress value for which no creep time is defined in the material data, i.e., the occurring stress is lower than the lowest stress for which a creep time is given. In that case, an alternative approach based on a third interpolation has to be used. The creep time is then defined by Equation 3.71.

$$t_{R,f_j,T_j} = min(t_A \cdot \frac{t_b}{t_a} \cdot Y_R; 2 \cdot t_b) \tag{3.71}$$

t_a and t_b refer to the two last creep times, for which data is given in the material data. The method mentioned above is also used to calculate the time until the yield limit is reached. Instead of the rupture strength, the yield limit is used.

For each load case f_j, the time until damage t_{D,f_j,T_j} is defined as the smaller value of both time until creep rupture and time until reaching the yield limit.

3.2.9.4 Assessment of Total Creep Damage

Finally, the damage is linearly accumulated to see if the structure withstands all acting creep loads. Following Equation 3.72, values smaller than one indicate that the structure withstands all occurring creep damage, and hence, the wall thickness may be reduced and the procedure iterated. A value higher than one, however, indicates failure before the end of the lifetime is reached. The wall thickness must be increased, and the procedure must be repeated. [39]

$$\sum_{j=1}^{n} \frac{t_j}{t_{D,f_j,T_j}} \leq 1.0 \tag{3.72}$$

3.2.9.5 Different Interpolation Techniques

As mentioned above, DIN EN 13445 uses a logarithmic interpolation approach. All methods are implemented in NPSS in this thesis. However, NPSS does not natively offer a logarithmic interpolation approach for tabular data. Therefore, linear interpolation is used. The error between the values from logarithmic and linear interpolation depends on the proximity of measurement points to each other. As data for Inconel 625 is provided in a continuous diagram, the error can be kept low. In this thesis, the discretization step corresponds to the distance between following logarithmic entries (e.g., 1 to 2 or 10 to 20). The maximum error between logarithmic and linear interpolation is 1.3 %.

3.2.9.6 Creep-Fatigue Interaction

As described in Section 3.2.9, creep is expected to occur in the considered TBHE, but not in the PFHE. Therefore, a closer look into the creep-fatigue interaction of TBHE is required to ensure structural integrity. As no data on the creep-fatigue interaction of Inconel 625 is available, a substitute is needed. In this thesis, Inconel 617 is chosen. Out of the available data, it is the most similar compared to Inconel 625. Equation 3.73 describes the total damage, derived from Figure 3.10 [67].

$$D(D_f) = \begin{cases} 1 - 9 \cdot D_f & \text{für } 0 \leq D_f \leq 0.1, \\ \frac{1}{9} - \frac{1}{9} \cdot D_f & \text{für } 0.1 < D_f \leq 1. \end{cases} \tag{3.73}$$

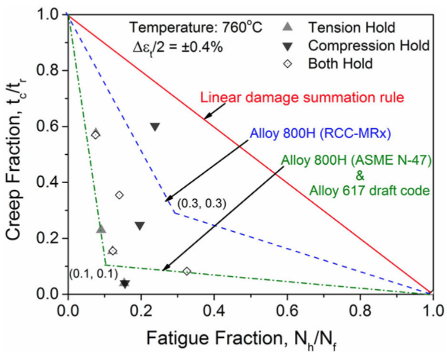

Figure 3.10: Creep-fatigue interaction for different materials [15]

4 Verification and Sensitivity Studies

This chapter presents results obtained using the methods described in Chapter 3. To verify these methods, Section 4.1 compares the results with those found in the literature, with industry data or FEM analyses. However, due to a lack of examples, some methods could not be verified. In these cases, sensitivity studies were conducted to assess the impact of uncertainties, as presented in Section 4.2. Once the accuracy of the methodology is assessed, Section 4.3 investigates the influence of different operating conditions on the factors of safety of the different failure modes. The design driving failure modes for both types of heat exchangers are derived. The impact of changing geometrical parameters is discussed in Chapter 5.

4.1 Verification

4.1.1 Corrosion

The design methodology used in this thesis is common practice in norms. Table 4.1 gives an overview of calculated as well as typical, industry-norm applied lump sum corrosion allowances. The lifetime of the component, and hence the time the material is exposed to the corrosive medium, significantly influences the calculated corrosion allowance. In order to facilitate comparison with industry data, both the calculated corrosion allowance and the industry values need to be referenced to the same lifetime. In Table 4.1, a reference lifetime of one year has been chosen. Therefore, the corrosion allowances presented are recommended values for a one-year lifetime.

Component	Calculated additional thickness	Typical corrosion allowance
Plate	0.144 mm	none [46]
Tube	0.184 mm	0.1 mm [44, 102]

Table 4.1: Comparison of the corrosion allowance calculated in this thesis and typical industry values for identical reference lifetime of one year.

Differences between both types of corrosion allowances, as seen in Table 4.1, can occur. As mentioned in Section 2.4.1.2, corrosion allowances are typically not applied to PFHE. Furthermore, industry norms only provide corrosion allowances for broader application ranges and do not specify them for specific operating conditions. Therefore, industry-norm corrosion allowances are only a rough estimate. Whilst providing a first estimation, standard corrosion allowances should only be used „unless the conditions of service make a different allowance more suitable“ ([44, p. 5.1-2]). The exhaust gas mixture can be a more severe condition of service, explaining the overestimation of the corrosion allowance using the method derived in this thesis.

Further verification of the corrosion method can be done by component corrosion testing. However, this is outside of the scope of this thesis. The results from the corrosion testing can be used to adjust the corrosion rate and hence the corrosion allowance. This allows a calibration of the method.

4.1.2 Static Stress

4.1.2.1 Plate-Fin Heat Exchanger

The methods developed in this thesis focus on the design of PFHE with fins in one flow channel and no fins in the second flow channel. However, literature on the stress estimation of PFHE only focuses on heat exchangers with fins in both flow channels. A FEM analysis of one unit cell in a parallel flow PFHE, which is equally finned in both flow passages, has been conducted in [103] and [104]. However, as the structural characteristics are different to a PFHE with no fins in the second flow channel, these analyses cannot be used as verification data.

Since no comparable data is available in the literature to fully verify the static stress calculation methodology of the PFHE, the accuracy of each step is assessed independently. The first step involves deriving a substitute load acting on the fins. In the second step, the length change of a fin, assumed as a bar, under the previously derived load is calculated. The third step determines the resulting stresses in a plate with a maximum deflection equal to the length change of a fin, as calculated in the previous step.

The derivation of the substitute load on the fins cannot be verified due to the lack of available literature data. Additionally, conducting experimental tests or performing FEM analyses to validate the methodology is beyond the scope of this thesis. To understand the consequences of this uncertainty, the effect of a changing plate stress has been investigated. It is presented in Section 4.2.2.
The following paragraphs aim to verify the second and third steps.

Length Change of a Fin, assumed as a Bar Using the stress-strain curves of Al6061-T6 presented in [105], different combinations of stress and strain are derived. Assuming a substitute load equal to the stress from the stress-strain diagram as an input, different length changes are calculated according to the presented methodology. Based on these length changes, strains are derived and compared to the strain values from the stress-strain curve corresponding to the relevant stresses. Table 4.2 gives an overview of the results.

Stress	**Strain from [105]**	**Calculated strain**
50 MPa	0.06 %	0.08 %
100 MPa	0.14 %	0.16 %
150 MPa	0.23 %	0.24 %
200 MPa	0.31 %	0.32 %
250 MPa	0.40 %	0.40 %

Table 4.2: Comparison between values from the stress-strain curve and the results obtained by the tool used in this thesis.

Differences can be explained by the used material data. The E-Modulus used in this thesis is approximately 62.99 GPa at the investigated temperature. The E-Modulus of the compared data differs significantly from it. It equals to 59.49 GPa [105]. A higher E-Modulus leads to a lower strain for a given stress, according to Hooke's law. Nevertheless, the strains and, therefore, the calculated length changes of the bar are in good accordance with the data for a similar E-Modulus found in [105].

Stress resulting from Maximum Deflection of Plate Using the derived length change as the maximum deflection of the plate, a substitute stress is derived according to Kirchhoff's plate theory. This stress is then applied to the plate. It should lead to an identical deflection of the plate. Figure 4.1 shows the results of a FEM analysis modeling the plate using shell elements, which is justified by its small thickness. It is loaded with the substitute stress.

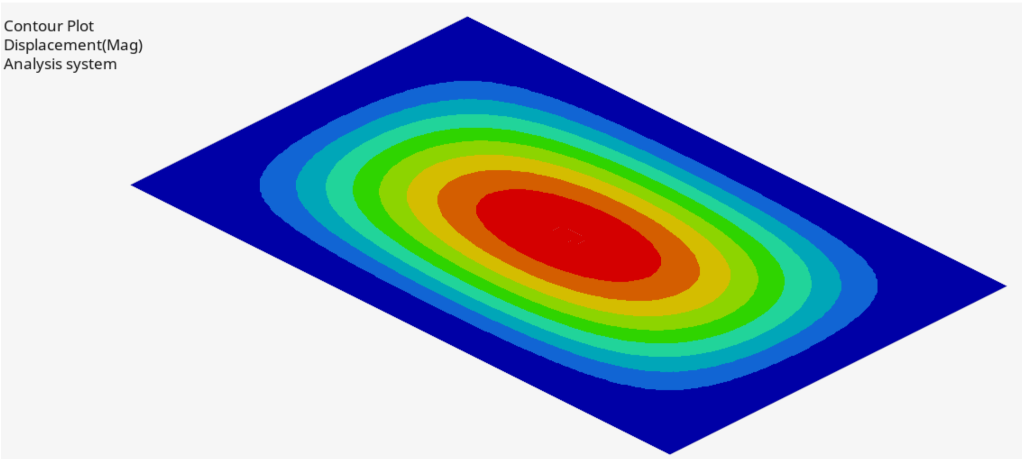

a) Deflection of a plate for the given load situation in mm.

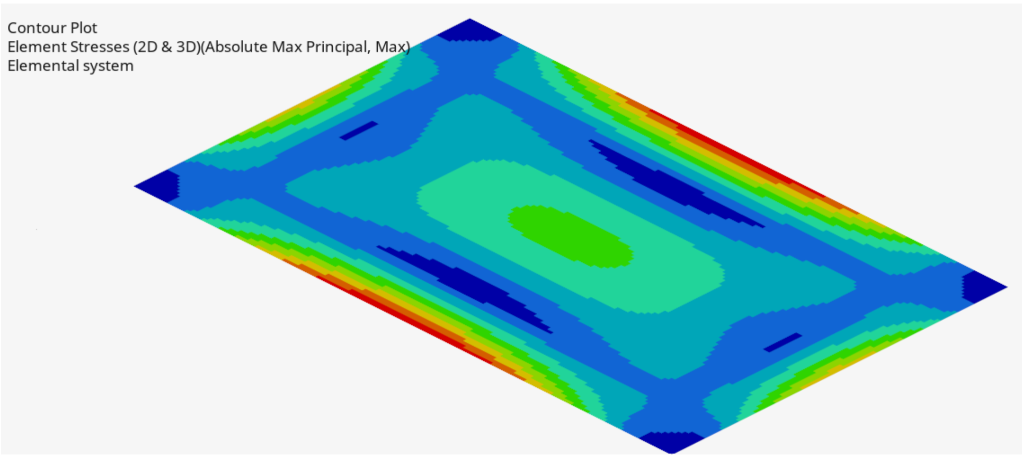

b) Derived stress of the deflected plate in Pa.

Figure 4.1: Results of a FEM analysis of a plate.

The tool underestimates the length change by approximately 10 %. These differences can occur due to the interpolation of the displacement differential equations by the constant factors α and β_1. The resulting stresses are overestimated by the tool by approximately 3 %. These minor differences are assumed to be acceptable during preliminary design.

In general, the method developed in this thesis shows good accordance with a simplified FEM analysis, assuming that the method to derive the maximum deflection of the plate by calculating the length change of a fin is correct. A FEM analysis of the complete structure including the fins is beyond the scope of this thesis. It could be used to verify the complete method, including all steps.

Buckling The buckling calculation method assumes the fins to act like a bar, consistent with the assumptions made for the stress calculation. The fins are joined to the bar, e.g. by brazing. They are therefore assumed to be clamped to the plate. The accuracy of the equations for the critical Euler force of bars and plates with different boundary conditions has been investigated and validated extensively (e.g. in [106]). A full FEM analysis is beyond the scope of this thesis. Therefore, this section focuses on comparing the buckling behavior of rectangular plates with different boundary conditions to the characteristic of a clamped bar.

Figure 4.2 shows the normalized critical buckling force of a rectangular plate and a bar for different aspect ratios $\frac{a}{b}$.

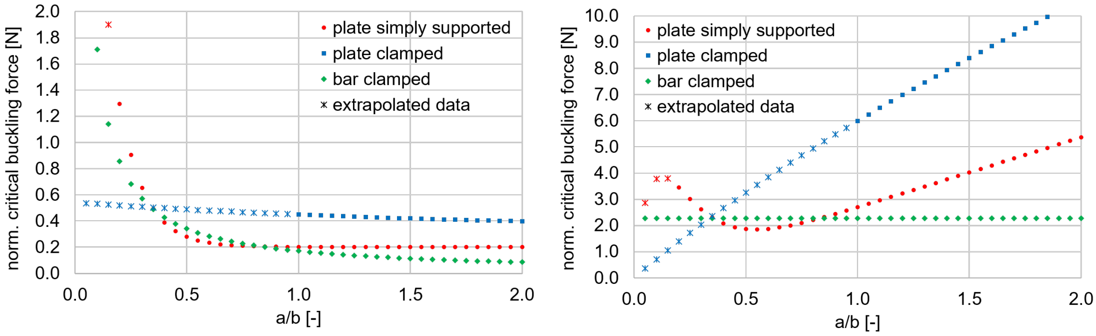

a) Critical buckling force for different aspect ratios $\frac{a}{b}$ by varying the fin height ($\hat{=}a$) (normalized by identical factor).

b) Critical buckling force for different aspect ratios $\frac{a}{b}$ by varying the flow length ($\hat{=}b$) (normalized by identical factor).

Figure 4.2: Comparison of critical buckling force derived based on different boundary conditions with extrapolated data indicated by a star.

As explained in Section 3.2.6.1, the buckling factor K of a rectangular plate has only been derived for aspect ratios $\frac{a}{b}$ larger than 0.2 and 1, assuming simply supported and clamped edges, respectively. Here, smaller buckling factors have been extrapolated based on a function derived through exponential regression using all available combinations of aspect ratio and buckling factor of the respective boundary conditions. Extrapolated values are indicated by stars in the respective color of the corresponding curves. A detailed explanation of the curves can be found in [106]. The following section explains the physical implications of the finding on the accuracy of the method used in this thesis.

This thesis assumes plain fins, meaning each fin completely extends in flow direction. The fin height, equal to the distance between the plates h_i, is typically much smaller than the length in flow direction l_i. Therefore, the fins can be characterized by a rectangular, thin plate with the dimensions h_i and l_i. In the equations used in this thesis and derived in [89] and [106], the aspect ratio $\frac{a}{b}$ is introduced, where b corresponds to the length of the edge, on which the load acts, and a to the other dimension of the plate. Applying this to the plain fin assumed in this thesis leads to $a = h_i$ and $b = l_i$. As $l_i \ll h_i$, the aspect ratio typically is very small.

Typically, a rectangular, simply-supported plate's critical buckling load is smaller than a plate clamped at all edges. This can be seen in both figures for the whole range, where buckling factors K have been numerically derived and not extrapolated. For very small aspect ratios, the critical buckling force of a clamped plate is lower than that of a simply supported one. This behavior is not expected, as the clamping of the plate typically increases its resistance against deformation. A simply supported plate allows rotations at the edge, which generally translates to less resistance against deformation. It is thus generally more prone to deformation and buckling than a plate clamped at all edges. Therefore, the critical buckling force of a clamped plate with extrapolated buckling factors probably does not accurately represent the actual plate characteristics.

Furthermore, the critical buckling force of a bar is typically smaller and/or similar to the critical buckling of a simply supported plate for a wide range of aspect ratios. For small aspect ratios and larger flow lengths $b = l_i$, the critical buckling force of a simply supported plate first decreases, as seen in Figure 4.2b. This is due to the calculation of the critical buckling force. Using a buckling factor K, the critical buckling stress is derived. However, to be able to compare it to the case of a bar, it needs to be converted to a force. This conversion is dependent on the fin length $b = l_i$. For small aspect ratios and larger flow lengths, the effect of an increase in the area the critical buckling stress acts on is more significant than the decrease in critical buckling stress due to the less slender plate.

For very small aspect ratios and extensive flow lengths $b = l_i$, the critical buckling force of a simply supported plate significantly decreases, as seen in Figure 4.2b. That would mean that very wide plates with a very small height would be more prone to buckling than more slender plates. However, increasing the width of the plate typically leads to more lateral stability. More total energy would be required to deform the plate laterally, as the area that needs to be deformed is larger. Therefore, the critical buckling load assessment of a simply supported rectangular plate probably does not accurately reflect the actual buckling behavior if the buckling factor K is extrapolated.

Overall, the extrapolation of buckling coefficients leads to inconsistencies compared to the characteristics using interpolated buckling coefficients. The method used in this thesis assesses buckling based, assuming the fins to be a bar. In general, the critical buckling force of a bar is smaller than and/or similar to the critical buckling force of the plates, assuming that the extrapolation of the buckling factor does not lead to an accurate representation of the actual behavior, as explained above.

Overall, the bar-based assessment used in this thesis generally provides a conservative estimate for fins, as its critical buckling force is lower than for clamped plates and similar to that of simply-supported plates. While this method offers a reasonable approximation, further accuracy could be achieved with a FEM analysis or component testing.

Tensile Rupture If the fins are not loaded in compression but in tension, they could rupture. Hence, the factor of safety against tensile rupture is derived in this thesis as well. The method utilizes material data, namely the E-Modulus and the yield strength, and compares it to the strain resulting from the length change calculation of the fins. Therefore, verifying this method would only lead to the verification of the material data used, which is beyond the scope of this thesis. As long as the assumption of the fins as bars is valid, which has already been extensively discussed above, and the material data is accurate, the method probably results in valid results.

4.1.2.2 Tube Bundle Heat Exchanger

Figure 4.3 compares the factors of safety of the different methodologies implemented for the TBHE for varying tube thicknesses. Varying the outer diameter of the tube, assuming a fixed thickness, leads to similar observations and is thus not shown here.

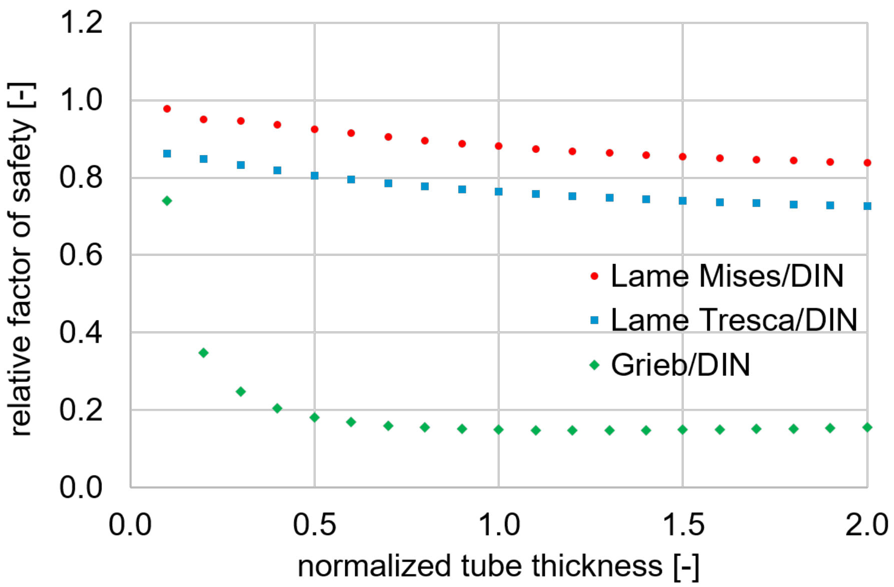

Figure 4.3: Factors of safety normalized by the DIN 13445 method for the different implemented methods with varying tube thickness.

As can be seen, in general the results according to the DIN EN 13445 are in good accordance with the results obtained by using the von Mises equivalent stress derived from Lame's formulas. The factor of safety, according to Grieb, is only dependent on the pressure difference and not on the tube thickness. Therefore, as seen in Figure 4.3, its relative factor of safety changes drastically. It is only in good accordance with the other methods for a small range. Additionally, it can be seen that Lames von Mises criterion leads to more conservative stress approximations compared to Lames Tresca criterion. Furthermore, Lames vessel formula leads to increasing discrepancies in the factor of safety according to DIN 13445 for higher tube thicknesses.

When comparing the different factors of safety of yielding with the corresponding one to UTS, an identical ratio of 2.198 is observable, independent of the chosen calculation method and the design variable, which is changed. As yielding leads to permanent changes in the geometry with non-linear material behavior afterwards, it should be avoided during operation. Therefore, in the following, only the factors of safety against yielding are further investigated.

The general behavior described above for changing tube thickness applies to changing pressure gradients as well. However, the factor of safety according to Grieb changes as well, leading to less changes in the relative factor of safety. Figure 4.4a shows the relative factors of safety normalized by the corresponding factor of safety according to DIN 13445. In this case the factor of safety according to Grieb is significantly more conservative than the one according to Lames formulas. The factors of safety according to Lames method are consistent with the factor of safety of the DIN 13445.

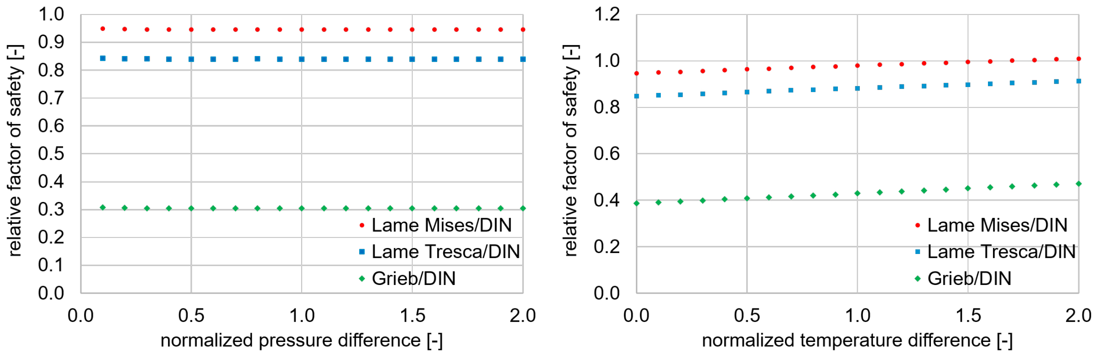

a) Relative factors of safety with varying pressure difference.

b) Relative factors of safety with varying temperature difference.

Figure 4.4: Factor of safety using the different implemented methods with varying operating conditions.

Figure 4.4b shows the different relative factors of safety normalized by the factor of safety according to DIN 13445 with varying wall temperature gradients. Similar to the behavior explained for the pressure difference, Grieb leads to a significant overestimation of the stresses, while Lames method leads to factors of safety in good accordance with the DIN 13445. For higher wall temperature gradients, the differences get smaller. Temperature differences lead to lower overall stresses according to the DIN 13445 when compared with Lame's method.

Overall, the methods according to DIN EN 13445 and von Mises stress from Lames formula are in good accordance with each other for most of the operating conditions and geometries. Special care has to be taken for thicker tubes. Grieb's method is only valid for specific operating pressure and temperature differences as well as tube thicknesses. In general, the method according to DIN 13445 leads to less conservative stress estimations compared with the other method's results.

A FEM analysis of a straight tube has been conducted in [92]. Table 4.3 compares the maximum stresses obtained from the implementation in this thesis with the stresses from this FEM analysis, as found in Figure 4 (b) of the respective paper. All values are in good accordance with each other.

Source	**Radial stress**	**Circumferential stress**	**Equivalent stress (von Mises)**
FEM analysis [92]	-34.63 MPa	162.24 MPa	196.88 MPa
DIN EN 13445 method	n.a.	n.a.	201.92 MPa
Lames formula method	-35.89 MPa	163.49 MPa	199.38 MPa

Table 4.3: Comparison between a FEM analysis and the results obtained by the tool used in this thesis.

All in all, both the method according to DIN EN 13445 and Lames von Mises formula yield consistent results for preliminary design and are a valid approach for assessing the structural integrity of TBHE. Lames Tresca-criterion leads to a more conservative assessment. Grieb's formula however is only valid for selected combinations of pressure difference and wall thickness.

4.1.3 Fatigue & Creep Calculation Methods

The creep as well as the fatigue calculation method follows the processes described in industry norms, like DIN EN 13445. However, until now, there are no replicable examples in the literature that would allow the verification of the methods. Therefore, the results for two different load conditions, leading to ”low” and ”high” stresses, were compared with an alternative tool.

4.1.3.1 Low cycle Fatigue Damage Calculation

In general, the result from the low cycle fatigue calculation strongly depends on the underlying material data. The material data used in this thesis is limited to a maximum of 10^8 cycles. In the case of the "low" stress condition, the occurring stresses are significantly lower than the maximum stress at the last measurement point. Without extrapolating the material data beyond the last measurement points, the fatigue damage according to the methods described in this thesis significantly differs from the damage result of the alternative tool. For low stresses, extrapolation can improve the accuracy of the methods in this thesis.

However, even when using an extrapolation or for higher occurring stresses, there is still a significant difference between the fatigue damage calculated from the methods in this thesis compared to the alternative tool. The most probable causes are differences in material data, underlining the importance of using proper material data. Further investigation using identical material data for two different assessment methods is beyond the scope of this thesis but can provide further verification of the calculation method.

4.1.3.2 High Cycle Fatigue Damage Calculation

The procedure described in Section 3.2.8 is industry standard, as described in [20]. However, it varies strongly with the applied lump sum stress amplitude. Verification would require component tests, which are beyond the scope of this thesis. The impact of the lump sum stress amplitude is investigated in Section 4.2.5.

4.1.3.3 Creep Damage Calculation

For the given "low" stress condition, the calculated creep damage in the TBHE is negligible, which is in accordance with the alternative tool.

In the ”high” stress condition, the creep damage calculated by the methods derived in this thesis significantly differs from the result obtained by the alternative tool. The most probable cause is, similar to the differences in the LCF assessment, the underlying material data.

As stated before, creep is not relevant for PFHE and is therefore not assessed in this thesis.

4.1.4 Conclusion

In general, the damage assessment strongly depends on the used material data and assumptions regarding the operational conditions, such as the corrosion rate. Assuming correct material data, the methods for the calculation of the static stresses in the TBHE provide enough accuracy. The methodology to assess the static stresses in the PFHE can predict the occurring pressure stresses well but cannot properly assess all temperature stresses. The assessment of LCF, HCF and creep strongly depends on the used material data and made assumptions. However, the material data as well as all the assumptions, e.g. regarding the lump sum stress amplitude, are user-defined and can be easily adjustable, as soon as more representative material data and values for the assumptions have been derived. The methods in this thesis thus provide a good first assessment of the stresses and can be improved once more knowledge of the material and operating conditions is available.

4.2 Impact of Methodology Uncertainties

This section investigates the impact of uncertainties in the methodology on relevant calculation results.

4.2.1 Impact of Corrosion Rate

To investigate the impact of the corrosion rate, a given TBHE geometry is investigated under certain operational conditions and exposed to varying corrosion rates. To relate the derived changes in factors of safety to masses, the tube thickness is varied to achieve designs of identical minimum factors of safety. In this study, the static strength is assessed using the factor of safety against yielding, as calculated using the DIN-13445 method. The increase in the tube thickness leads to an increased outer diameter. The inner diameter remains constant. Figure 4.5 shows the impact of changes in geometry, which are required to withstand the higher corrosion rate, on the mass of a TBHE.

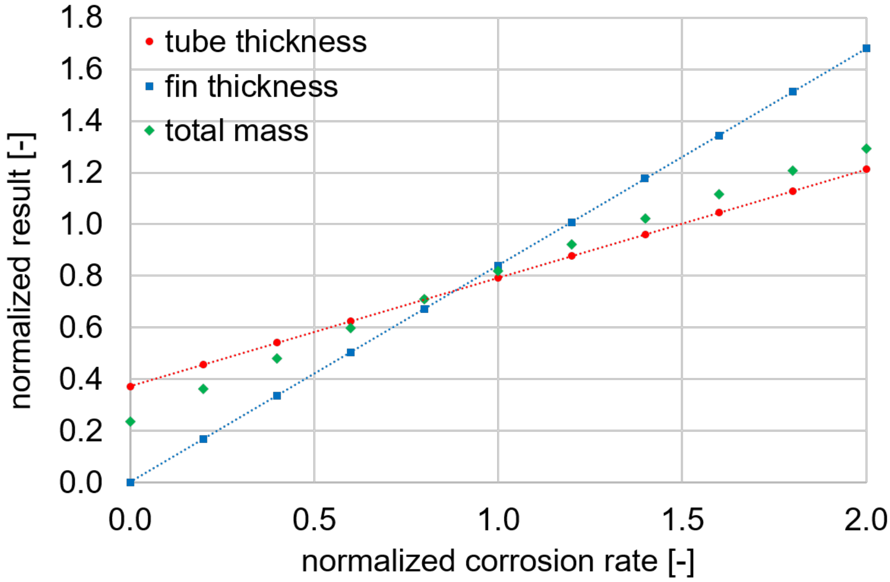

Figure 4.5: Mass and thickness of tube and fins of TBHE with changing corrosion rate (thicknesses normalized by identical factor).

With increasing corrosion rate, more material has to be added as corrosion allowance. Hence, the mass increases. In the case of the TBHE, the fins are exposed to the corrosive medium on both sides. Additionally, they are assumed to carry no structural load. Therefore, their minimum thickness is only defined by the corrosion rate. Hence, doubling the corrosion rate leads to twice the fin thickness.

The tube itself carries all the loads. Therefore, it has a baseline value, as can be seen by the non-zero y-axis intercept, even though a corrosion rate of zero is assumed. When increasing the corrosion rate, this baseline value dampens the normalized change in tube thickness. If the tube would not carry any loads, its thickness would increase by half as much as the thickness of the fins increases because the inner surface is not exposed to corrosion. Hence, the gradients of both thickness curves are correlated by a factor of two, as the corrosive medium acts on both sides of the fins, but only on one side (the outer wall) of the tube.

The changes in required thicknesses influence the mass. Figure 4.6 shows the distribution of the masses on the different components. With an increasing corrosion

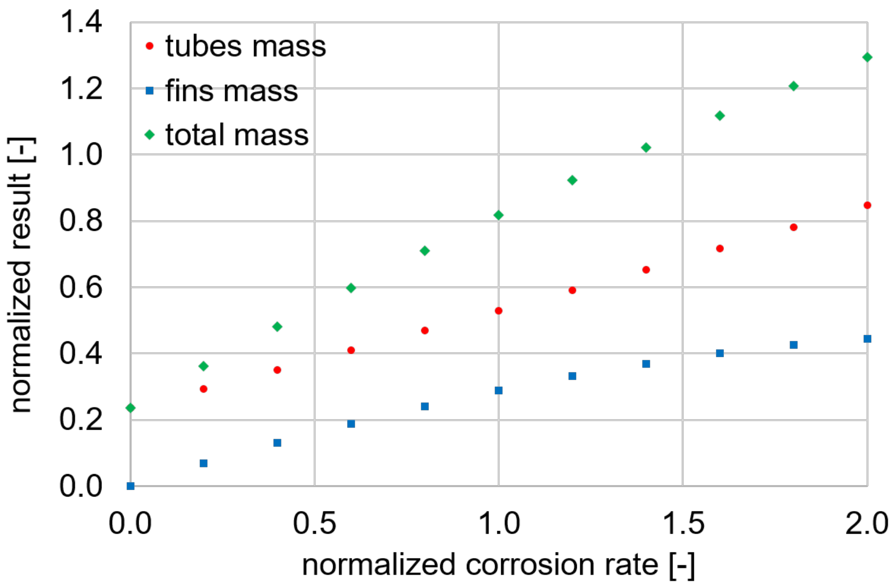

Figure 4.6: Mass of the tube and fins of TBHE with changing corrosion rate (normalized by identical factor).

rate, mass increases. The tube's mass is calculated using the cross-sectional area of the tube's wall. The outer diameter of the wall is defined by the inner diameter plus twice the respective tube thickness. It then needs to be squared to derive the cross-sectional area. Therefore, its behavior is, compared to the change in thicknesses, not linear.

A thicker tube influences the fins' mass as well. Increasing the tube thickness leads to a larger outer diameter of the tubes. As the tubes intersect with the fins, a thicker tube leads to larger perforations in the fins. The fins' mass increases due to the extra thickness required to withstand corrosion but tends towards a limit value. That limit value is defined by the fins' width and height. These studies were conducted for a fixed bend radius SL and horizontal distance between two adjacent tubes ST. The fins width and height were thus fixed. With an increasing tube thickness, the distance between the outer wall of two different tubes, assuming constant ST and SL, decreases. At some point, the outer walls would overlap themselves, posing an unrealistic design. These designs are therefore omitted.

Both effects, the increase of the fin thickness coupled with the increasingly significant decrease in cross-sectional area of the fins due to the perforations leads to the behavior of the mass of the fins seen in Figure 4.6

Overall, the corrosion rate significantly influences the required thicknesses of tubes and fins, and therefore the mass. A corrosion rate twice as large results in an approximately doubled mass. As the heat exchangers themselves are already quite heavy, these changes in mass are significant in absolute numbers as well.

As the accurate estimation of the required mass is one of the objectives during preliminary design, the corrosion rates used during its calculation process need to be chosen carefully. Otherwise, there can be significant over- or underestimation of the mass. Component corrosion tests should be carried out even at a preliminary design stage to accurately predict the corrosion rate.

Besides the choice of the right corrosion rate, corrosion is indeed a major failure mode and a significant impact factor on heat exchangers' mass. The usage of corrosion-resistant materials is beneficial.

The corrosion rate impacts both PFHE and TBHE. The calculation method of the corrosion allowance used in this thesis is identical. However, the effect the corrosion allowance has on the mass differs slightly due to the different geometries assumed and the different areas of exposure of the material. Nevertheless, the trends indicated above are observable in PFHE, with the total mass increasing significantly for a higher corrosion rate.

4.2.2 Impact of Plate Stress

As the method to calculate the stresses in the PFHE could not be fully verified, the influence of varying plate stresses on the factors of safety is investigated. Figure 4.7 shows the resulting factors of safety assuming a varying stress in the plate as an input. Exaggeratingly high factors of safety are excluded to keep the figure readable.

The factor of safety against yielding is described by dividing the yield strength of the material by the acting plate stress. As only the plate stress is changed in this study, Figure 4.7 shows this expected hyperbolic relation. The accurate prediction of the acting stresses in the plate is important. Underestimating the stresses in the plate by 50 % can lead to a change in the factor of safety of 100 %. Using different methods,

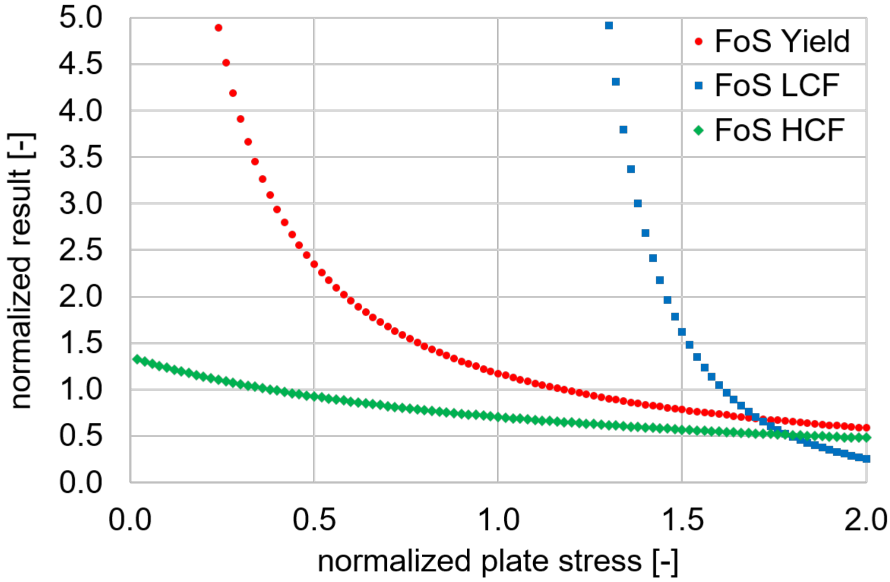

Figure 4.7: Factors of safety with changing plate stress (normalized by identical factor).

like a FEM analysis, and deriving correction factors can ensure the consistency of the results obtained using this method with the actual stress characteristic.

Furthermore, Figure 4.7 shows the factors of safety against LCF and HCF. LCF is constant for low normalized plate stresses at a large value outside of the scale of the figure. After crossing a certain threshold, it follows a hyperbolic trend. This is due to the nature of the material data. It follows a hyperbolic decrease with increasing number of allowable cycles, tending to an asymptotic value for $n \to \infty$. However, in reality, stresses below the asymptote can occur. To allow the computation, all stresses below the asymptote are assumed to lead to a certain constant value of cycles. This is chosen to be the amount of cycles for endurance strength, which is typically 10^8 cycles. Therefore, low stresses lead to constant factors of safety for LCF, even though the stresses change.

HCF shows a different behavior. Its factor of safety, described by the ratio of the distance from the origin to the point and to the Goodman-line through the load condition point, decreases with increasing mean stress. Figure 4.8 shows a Goodman-diagram for load conditions with increasing mean stress.

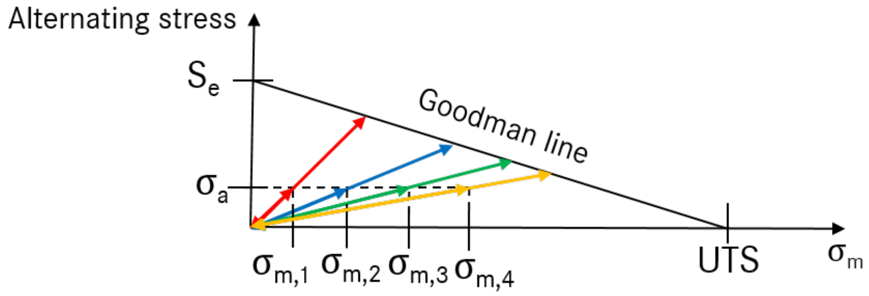

Figure 4.8: HCF calculation for increasing mean stresses.

For low mean stresses, larger changes in the distance ratio occur. Here, the stress amplitude is significant compared to the mean stress. With an increasing mean stress, the amplitude gets less significant compared to the mean stress. Therefore, the line from the origin to the Goodman-line through the load condition point gets less steep. In the Goodman-line itself, the allowable stress amplitude reduces less than the allowable mean stress increases. If the mean stress is the dominant stress, the increase of the means stress itself gets more and more equal to the increase of the allowable mean stress. For load conditions with significant mean stresses, the ratio and therefore the factor of safety hence decreases hyperbolically to a set value. This can be seen, when comparing $\sigma_{m,3}$ to $\sigma_{m,4}$. The mean stress increases significantly in both the actual load condition and the allowable load condition. Furthermore, the allowable stress amplitude decreases while the mean stress amplitude is constant. However, the stress amplitude ratio tends towards one for increasingly large mean stresses. Combining both effects leads to the asymptotic behavior of the ratio between the occurring and allowable stress condition, which equals the factor of safety.

All factors of safety, including yielding, LCF and HCF, are normalized by the same value. Therefore, for the investigated geometry, one can conclude that for lower plate stresses, HCF is more critical. After crossing a certain plate stress threshold, LCF dominates the design choices. Yielding typically is not design driving in the case of the PFHE for the assumed material.

4.2.3 Impact of Temperature Difference on PFHE

Another stress used in the calculation of the total plate stress is the stress due to the temperature difference between the plates' surfaces. Its influence is investigated by changing both the hotter and colder side wall temperature while keeping the mean wall temperature constant. This avoids changes in material properties. Figure 4.9 shows the derived factors of safety.

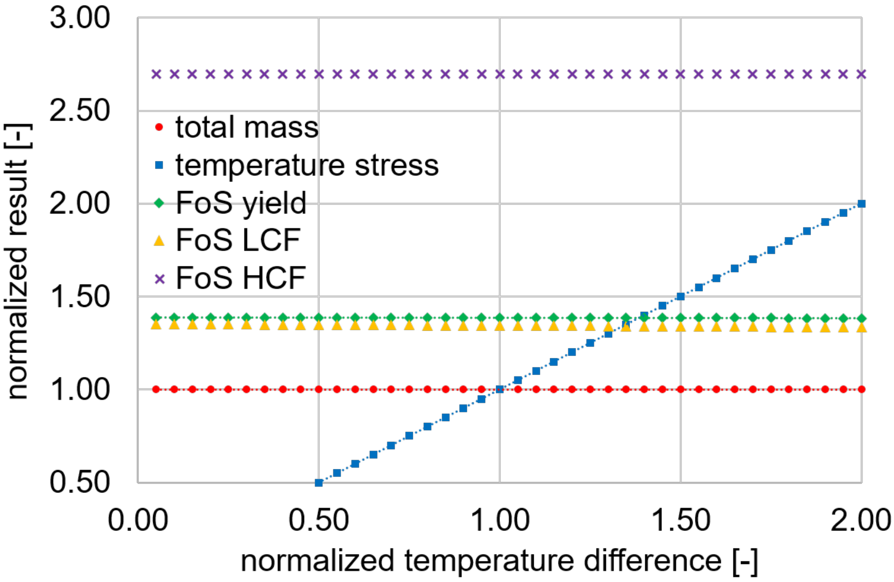

Figure 4.9: Factors of safety with changing temperature difference and constant average material temperature (FoS normalized by identical factor).

As can be seen, the normalized factors of safety barely change. While the temperature stresses linearly increase with the normalized temperature difference, the influence on the yielding and LCF factors of safety is negligible. This stems from the temperature stress being significantly smaller than the other two plate stress components: the substitute plate stress and especially the plate segment stress. Even significantly increasing the fin density and/or thickness, and hence reducing the two other plate stress components, does not lead to any changes.

As explained in Chapter 2, temperature gradients and the resulting interaction between the components can typically lead to significant temperature stresses in PFHE. This is not reflected in the provided method. Therefore, the derived method is not well suited for estimating temperature stresses besides the temperature stress due to a radial temperature gradient in the plate of a PFHE.

4.2.4 Impact of Transient Overshoot Factor

In this thesis, a set factor is used to account for the stress increase expected during transient operation. It is applied for the calculation of the factor of safety against LCF.

4.2.4.1 Plate-Fin Heat Exchanger

Increasing the transient overshoot factor in the case of the PFHE leads to a higher mean stress, equivalent to an increase in the plate stress. Therefore, the behavior of the PFHE with increasing transient overshoot factor is identical to the one described above in Section 4.2.2 for an increasing plate stress.

4.2.4.2 Tube Bundle Heat Exchanger

Figure 4.10 shows different factors of safety for LCF and the creep-fatigue interaction as well as the corresponding corrected stress using different transient overshoot factors for the TBHE. All curves are normalized by different values.

The factor of safety of LCF decreases less significantly for lower transient overshoot factors than for higher transient overshoot factors. This behavior stems from the underlying material fatigue data combined with the correction of the stress to a zero mean stress. The corrected stress follows a trend of the form $\frac{x}{1-k_1*x}$ with $k_1 * x \leq 1$ and k_1 being a constant. The material data is not determined for low stresses. In this case, it is linearly extrapolated. In Figure 4.10, all but the last two points are calculated based on extrapolated points. For these points, a higher corrected zero mean stress leads to a linearly decreasing number of allowable cycles. However, the corrected zero mean stress increases faster for higher transient overshoot factors.

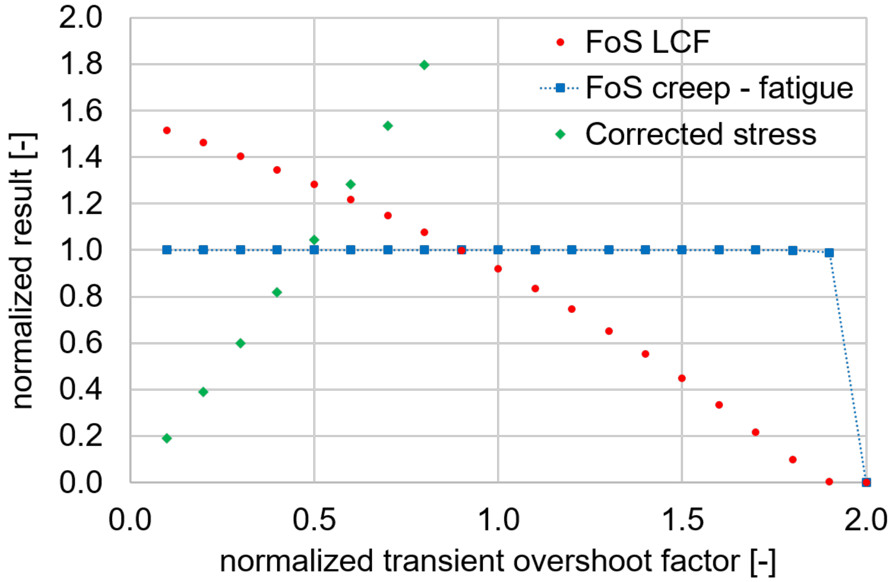

Figure 4.10: Corrected stress, LCF and creep-fatigue factor of safety of TBHE with changing transient overshoot factor (normalized by different factors).

Then, the number of allowable cycles decreases faster as well. This is exactly what can be seen in Figure 4.11.

The last two points on the factor of safety LCF curve seem to have the same y-value. However, they still change, but much less than observed before. As the number of allowable cycles cannot be below zero, the factor of safety against LCF cannot become negative. This implies that the trend described above cannot continue for very large transient overshoot stresses. It is only valid for smaller transient overshoot factors and thus large factors of safety against LCF. As soon as the factor of safety approaches a certain threshold and the material fatigue data is not extrapolated anymore, its characteristic changes. Therefore, it is further investigated below.

As indicated by the figure, the choice of the transient overshoot factor leads to a change in the factor of safety of LCF. However, its importance is significantly higher after crossing the explained threshold, leading to LCF being the design driving factor.

In the methodology implemented in this thesis, the transient behavior has no influence on the static calculation process. Hence, the static, creep and HCF behavior remains unchanged. However, creep-fatigue interaction gets more severe with increasing LCF. It changes following the trend explained in the factor of safety of LCF. However, as the absolute LCF factor of safety is at a high level for most of the range shown, its influence on creep is small. Therefore, the interaction between fatigue and creep is mainly driven by the creep damage, which is constant in this study. Only after the LCF factor of safety drops to a lower level the factor of safety of the creep-fatigue interaction drops sharply.

Further Investigation for High Transient Overshoot Factors The area in which the above-mentioned drastic changes occur is further investigated in Figure 4.11. Here, both curves are normalized by the same value.

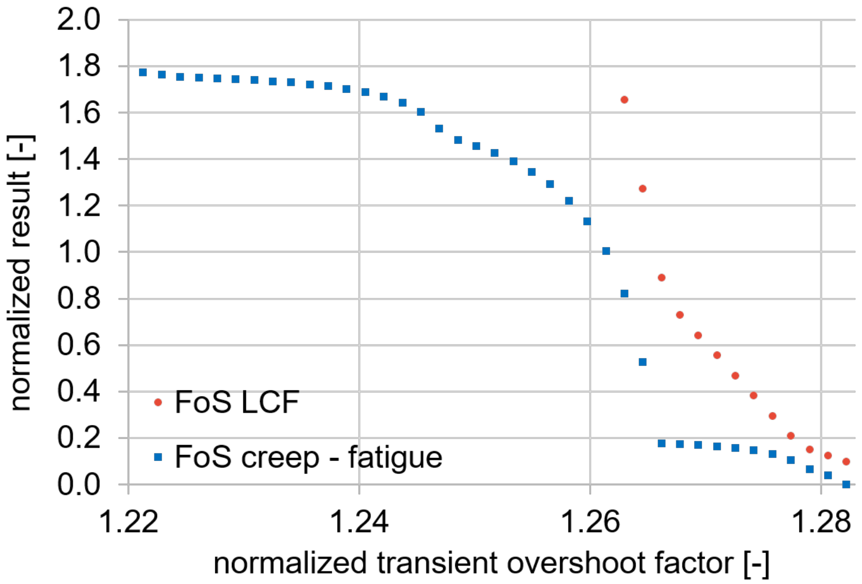

Figure 4.11: LCF and creep-fatigue factors of safety of TBHE for high transient overshoot factors (normalized by identical factor).

In contrast to Figure 4.11, in this figure, the factor of safety against LCF damage is based on interpolated material data. The material characteristic allowable stress decreases hyperbolically towards an asymptote for an increasing number of cycles. The difference between the number of allowable cycles between two stresses decreases with increasing stress levels. As the factor of safety against LCF compares the number of allowable cycles to the number of occurring cycles, this behavior translates to the factor of safety against LCF, depicted by red dots in Figure 4.11. If the transient overshoot factor is smaller (but big enough to be inside of the material data), the corrected stress is smaller as well. The number of allowable cycles increases significantly for a slight increase in corrected stress. Therefore, the gradient of the factor of safety against LCF is large in the beginning. For a higher transient overshoot factor, the gradient gets smaller.

The factor of safety of the creep-fatigue interaction, in general, is always lower than the LCF safety factor, as the creep-fatigue interaction involves creep as well. Furthermore, an inflection point in the creep-fatigue curve can be seen. This point corresponds to the intersection of the two straights in the creep-fatigue interaction diagram, as described in Figure 3.10. Here, the gradient of the curve changes suddenly, leading to an inflection point. Before the inflection point, a small change in LCF damage leads to a big change in the allowable creep damage. After the inflection point, further changes in LCF damage lead to a smaller change in allowable creep damage. As the creep damage remains constant in this study, the factor of safety of creep-fatigue interaction decreases less after the inflection point.

4.2.4.3 Conclusion

Overall, the choice of the transient overshoot factor influences the LCF behavior. However, for most cases, LCF is not the design limiting factor. Only after passing a certain threshold, it can become design driving and special care must be taken to accurately predict the stresses during transient behavior. If material data were available for smaller stresses as well, the behavior described in Figure 4.11 would be observable for lower transient overshoot factors as well. The fatigue material data follows a hyperbolic trend. Its gradient gets smaller for an increasing number of cycles, while the gradient of the linear extrapolation is constant. Therefore, the factors of safety against LCF would be assumed to be even larger than the extrapolated ones.

The creep-fatigue interaction factor of safety accounts for both creep and fatigue and is therefore always smaller than the factor of safety of LCF. For very high factors of safety of LCF, it is an indicator for the creep damage. With increasing LCF damage, it is more significantly influenced by LCF.

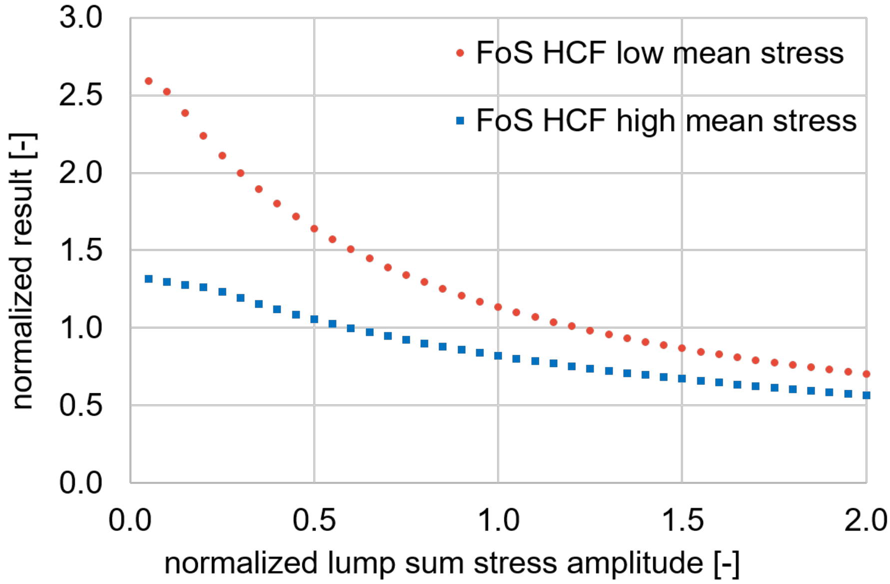

Figure 4.12: HCF factor of safety of PFHE with changing lump sum stress amplitude for two stress scenarios (normalized by identical factor).

4.2.5 Impact of assumed Lump Sum HCF Amplitude

The last source of uncertainty in the developed methods results from the estimation of the lump sum stress amplitude acting during HCF. Figure 4.12 shows the normalized factor of safety against HCF for various lump stress amplitudes and two different mean stress scenarios: a ”low” and a ”high” one. Both lines have been normalized by the same value. While this figure refers to the PFHE, a similar behavior is observable for the TBHE. The HCF calculation process is independent of the heat exchanger type. Only the required material data for the Goodman-diagram varies. In general, for lower lump sum stress amplitudes, the HCF factor of safety changes more significantly than for higher lump sum stress amplitudes. For $\sigma_a \rightarrow \infty$, a decreasing gradient is observable. Furthermore, a lower mean stress leads to a more significant change in the factor of safety than a higher mean stress.

The factor of safety is calculated by comparing the distance from the origin to the load condition point and to the modified Goodman-line through the point. The stress amplitude is only one of the two components. Therefore, its influence decreases with a higher mean stress, which is the second component, explaining smaller changes.

For very small lump sum stress amplitudes, the factor of safety against HCF does not change significantly. The magnitude of the gradient then increases until a kink occurs. Thereafter, the changes in factor of safety against HCF reduced hyperbolically. This characteristic, including the kink, can be explained by the modified Goodman-line. It is described by two straight lines, one connecting the endurance strength to the UTS and one connecting the yield strengths, as shown in Figure 3.9. The maximum allowable mean stress-amplitude combination is described by the point on either of the two lines, which is closer to the load condition point.

The kink corresponds exactly to the load condition point, which is equally far away from either line. For a higher stress amplitude, the load condition point is closer to the line connecting the stress at the endurance limit and the UTS. For lower stress amplitudes, the point is closer to the yield line. As shown in Figure 3.9, the steepness of the lines changes. This leads to a change in the allowable load condition, leading to a kink in the factor of safety curve. As the yield line is only design limiting for a small range of stress amplitudes, the effect is limited to a small region. For a higher mean stress, the kink occurs for a higher lump sum stress amplitude. The point of the load condition is closer to the yield line and therefore is still limiting, even for a higher stress amplitude.

The hyperbolic behavior of the curves in general can be explained by the changes in the distances to the modified Goodman-line and to the load condition point. While the first distance changes with $\Delta g \sim \sqrt{(\frac{1}{x^2})}$, the second distance changes with $\Delta\sigma \sim \sqrt{(x^2)}$. Dividing both to get the factor of safety leads to a hyperbolic behavior. It is dampened by the material properties used for the Goodman-line.

In general, changing the lump sum stress amplitude influences the HCF factor of safety, especially in cases where the mean stress is low.

4.3 Design-Driving Failure Mode

This section aims to derive the failure mode, which drives the design for the assumed operational conditions and geometric properties. It is described as the lowest factor of safety of all failure modes.

4.3.1 Plate-Fin Heat Exchanger

No creep is assumed in the PFHE. Therefore, the possible failure modes include yielding, LCF and HCF, assuming that the corrosion allowance is chosen sufficiently high. As described in Section 4.2.2, for a wide range of plate stresses, HCF is the design driving failure mode. Furthermore, for higher plate stresses and higher transient stresses, LCF becomes dominant.

An increase in required lifetime leads to an increase in plate thickness to cope with the occurring corrosion. Furthermore, the number of cycles, and hence, the LCF damage increases. However, as explained above, LCF is only relevant for higher plate stresses and/or higher transient stresses. Therefore, HCF is design-driving in most of the cases.

4.3.2 Tube Bundle Heat Exchanger

When assessing the TBHE, LCF is mainly influenced by the transient overshoot factor, as explained in Section 4.2.4. HCF is driven by the stress amplitude, as explained in Section 4.2.5. Increasing the mean stress does influence the static strength more significantly than HCF. The last failure mode, creep, has not been investigated more thoroughly in Section 4.2 and will be assessed below.

Figure 4.13a shows the relation between creep and yielding for different temperature levels, indicated by different depictions. The temperature levels are plotted according to the temperature difference T_{diff} from a certain value T. The horizontal line at one indicates the turnover points. Above the line, the factor of safety of creep is larger than that of yielding. Below the line, the creep behavior dominates the design. With increasing lifetime, creep gets more and more important, and the curve follows a hyperbolic trend. Furthermore, the mean wall temperature does not influence the relation significantly for lower mean wall temperatures. However, after crossing a certain threshold, changes are more drastic and can lead to creep driving the design for all lengths of lifetime.

This can be explained by the underlying material data. Figure 4.14 shows the creep strength for creep times between 0 and 2000 hours of a fictitious material. The creep

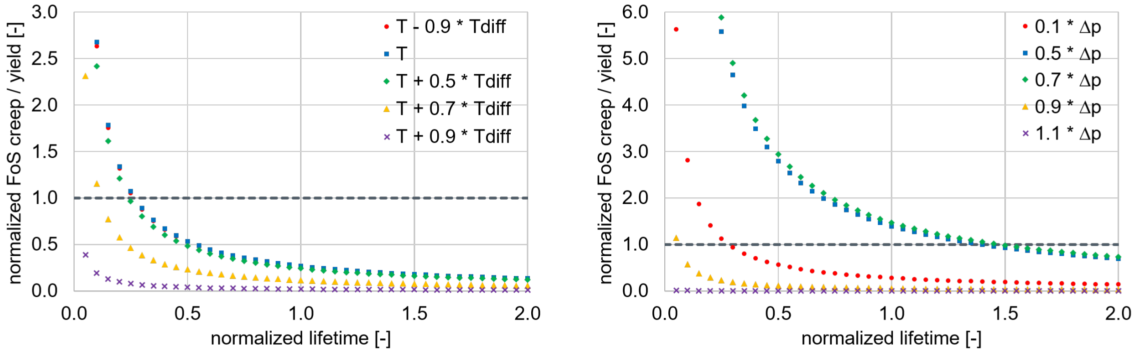

a) Factor of safety relation for different mean wall temperatures and lifetimes (all normalized by identical factor).

b) Factor of safety relation for different pressure differences and lifetimes (all normalized by identical value).

Figure 4.13: Relation between creep and static strength of a TBHE for different temperatures and pressure differences.

data follows approximately a linear decreasing line in the direction of the logarithmic x-axis. This leads to a hyperbolic decrease in a diagram with a linear x-axis, as seen in Figure 4.14.

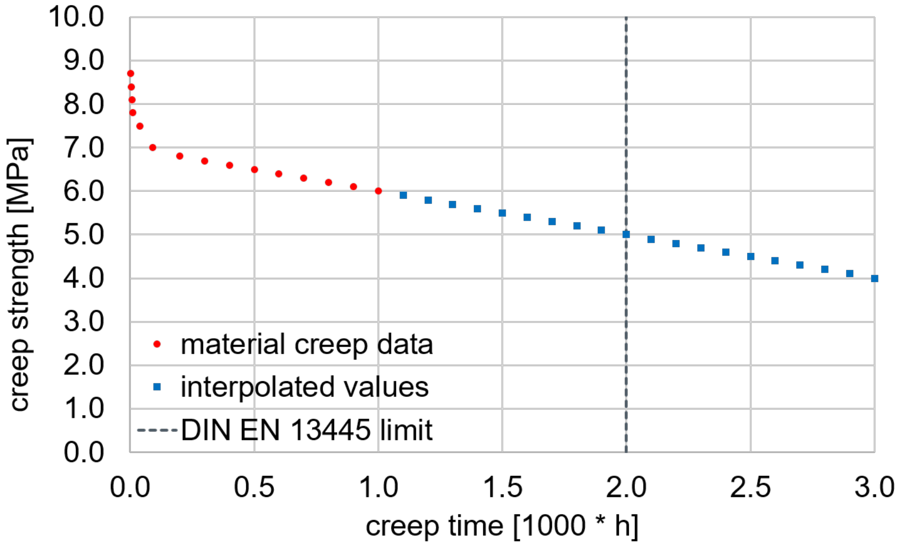

Figure 4.14: Exemplary creep data for a fictitious material and interpolation results according to DIN EN 13445.

However, stresses below the last given creep strength, which is 6 MPa in Figure 4.14, can occur. The creep times associated with these stresses will then be interpolated according to DIN EN 13445. Furthermore, DIN EN 13445 defines a maximum al-

lowable creep time at a value of twice the last material data point measured. The dashed line indicates this limit. If no material data is available, the allowable creep time is therefore significantly smaller than the the real value.
In the case of the fictitious material in Figure 4.14 and an assumed stress of 4 MPa, the resulting interpolated creep time would be 3000 hours. However, as this is more than twice the creep time of the last given material data point, the latter is used instead. This leads to a maximum allowable creep time of 2000 hours in the example. The maximum allowable creep time stays constant until the stresses are high enough that the calculated creep time is below this threshold; in the case of the fictitious example higher than 5 MPa.
In general, higher mean temperatures lead to a decreasing creep strength. Therefore, stresses can be high enough to be inside the material data. After passing this threshold, the creep behavior changes, lowering the curves.

However, the time-independent material data, especially the yield limit, gets lower with increasing temperature. If the stresses are too low and the creep time is thus limited by the maximum, increasing mean temperatures can lead to a higher curve. This includes the curves of T, which is above the curve for $T - 0.9 * T_{\text{diff}}$, even though the temperature is higher.

Figure 4.13b shows the second main influence of creep and static strength: the pressure difference between the inner and outer side of the tube, assumed at a set mean wall temperature. Here, the behavior is similar to the behavior for different mean wall temperatures. However, the pressure difference influences the factor of safety against yielding more significantly, as it directly influences the acting stresses. This explains the large gap between $0.1 \cdot \Delta p$ and $0.7 \cdot \Delta p$. While the pressure difference gets larger, the yielding factor of safety decreases significantly, while the creep behavior remains identical, as it is capped at twice the maximum value. In this case, the stresses are too low compared to the available material data. However, after passing a certain threshold (here around $1 \cdot \Delta p$), creep becomes much more dominant, irrelevant of the lifetime.

All in all, the design-driving failure mode of the TBHE strongly depends on the operating conditions and the geometry. Creep dominates for large lifetimes, high mean wall temperatures and high pressure differences. In the case of high transient stresses, indicated by high transient overshoot factors, LCF is design driving. Having large stress amplitudes leads to HCF being the most influential. However, until the design leads to operating conditions and stresses below the critical thresholds, as explained above, yielding is the dominant design driver, and creep and fatigue are less relevant.

5 Influence of Changes in Geometrical Properties

Chapter 4 showed the plausibility of the results obtained using the methodology introduced in this thesis and indicated some of its limitations. Furthermore, the design-driving failure mode for different scenarios has been derived.

This chapter examines how variations in geometric parameters affect the factors of safety, by analyzing the resulting changes in mass and geometry.

To investigate the impact of varying geometric parameters, the effects on the resulting static stresses and, hence, the factor of safety against yielding are investigated. These stresses are used in the calculation of the other failure modes, creep, LCF and HCF, as well. Furthermore, the static stresses do not face as significant uncertainties as the other failure modes do: Creep and LCF are highly dependent on the available material data as well as the assumed lifetime. Similarly, HCF is strongly dependent on the assumed lump sump stress amplitude.
The effects of an increasing stress on the other failure modes have been presented in Chapter 4.

Therefore, this section focuses on the impact of the geometric parameters of the heat exchanger on the factor of safety against yielding under static loading.

5.1 Plate-Fin Heat Exchanger

5.1.1 Change in Plate Thickness

Figure 5.1 shows the effects of increasing the plate thickness, assuming constant temperatures of the plate on both surfaces and a constant overall height of the heat exchanger.

The graph shows a maximum of the factor of safety for a certain normalized plate thickness. This can be explained by looking at the resulting plate stresses and its

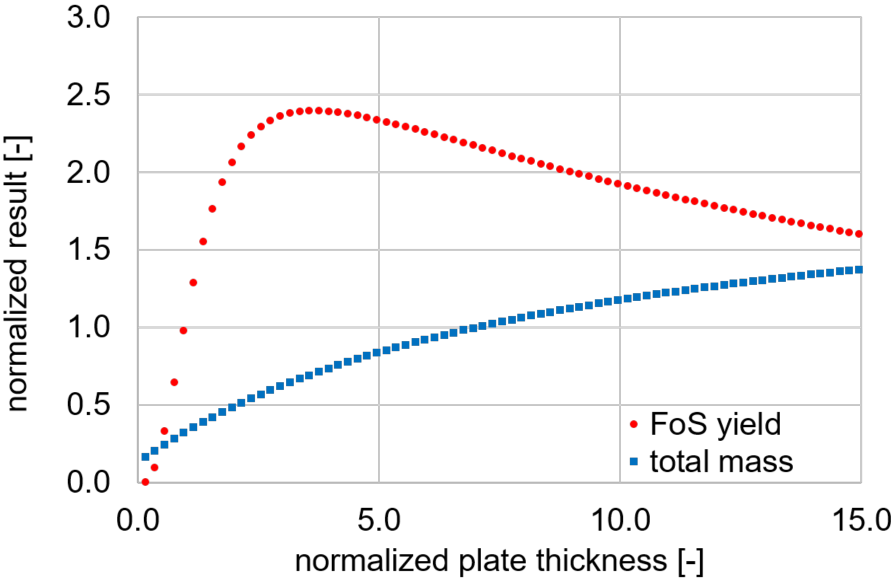

Figure 5.1: Factor of safety against yielding of PFHE with changing plate thicknesses.

components, as shown in Figure 5.2. All stresses are normalized by the same value.

The total stress has a minimum corresponding to the maximum factor of safety. For low plate thicknesses, the total stress in the plate is mainly driven by the stress due to the bending of the plate between two fins, the so-called segment stress. As it decreases hyperbolically, after a certain threshold, the temperature stress, which is constant for all plate thicknesses, becomes more important. It is only dependent on the temperatures of both plates' surfaces, which are assumed to be constant within this study. However, in reality, an increase in plate thickness could change the temperatures on the plates' surfaces. The stress calculated using the shortening of the fins as maximum displacement, the so-called substitute stress, increases with increasing plate thickness due to an increasing mass and, therefore, higher gravitational force of one plate acting on the fins. The total mass, as seen in Figure 5.1, increases less for a higher plate thickness. One of the assumptions made in this study is a fixed overall height of the heat exchanger. Therefore, while the plate thickness increases, the number of passages has to decrease and therefore the number of plates, fins and sidebars reduces, explaining the flattening of the mass curve.

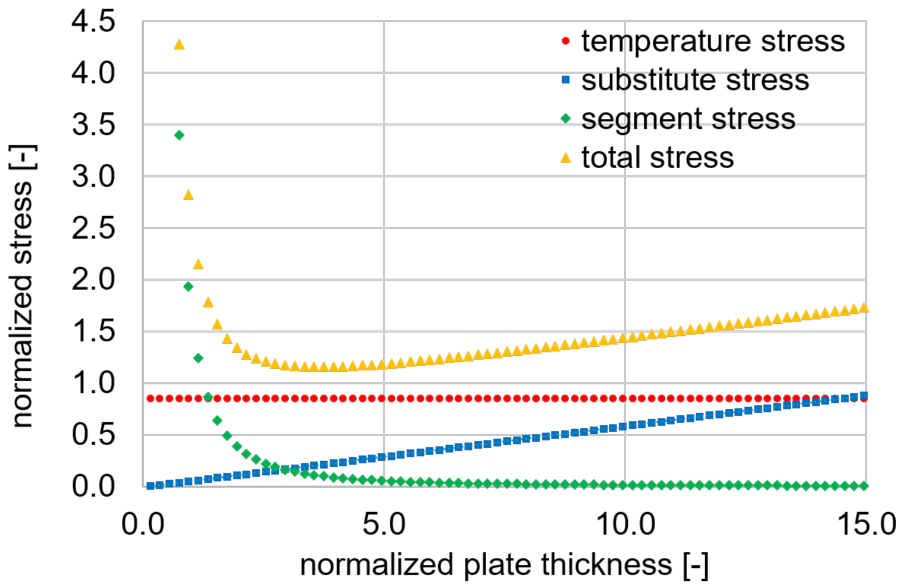

Figure 5.2: Stress components of PFHE with changing plate thicknesses (normalized by identical factor).

The methods in this thesis assume that the fins carry all the load. Hence, despite the increasing weight of the plate, the forces acting in the fins change only due to the additional mass of a thicker plate. However, the weight is significantly smaller than the pressure and temperature load. Therefore, the factors of safety against buckling and rupture remain nearly constant.

Increasing the plate thickness leads to less heat transfer through the wall. From a thermodynamic perspective, thin walls are strived for, keeping the thermal resistance low. This is what makes the PFHE so attractive. Therefore, while trying to optimize the structure, one has to keep the impact on the heat transfer in mind.

5.1.2 Change in Fin Thickness

The resulting stresses occurring in the plate can be influenced by changing the thickness of the fins, as well. However, the maximum thickness of the fins is influenced by the fin density. For a given fin density, FD, the distance between two fins and hence the maximum thickness is given by $\frac{1}{\mathrm{FD}}$.

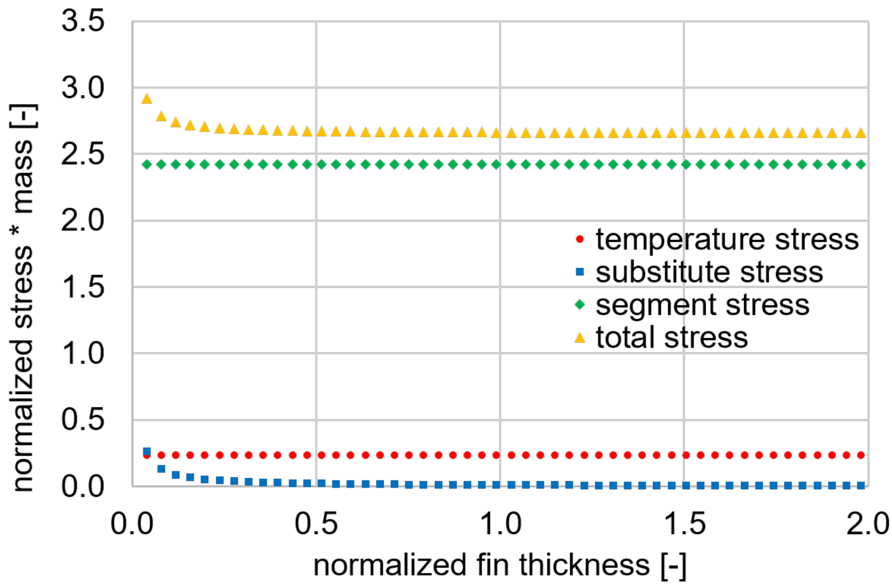

Figure 5.3: Stress components of PFHE with changing fin thicknesses (normalized by identical factor).

Figure 5.3 shows the changes in the plate stress due to a changing fin thickness. All curves have been normalized by the same value.

The temperature stress remains constant. Furthermore, for very low normalized fin thicknesses, the substitute stress component, while still being lower than the segment stresses, has a more significant influence on the resulting stress. This shows the effect of the developed methodology; it assumes the fins to carry all loads. Therefore, with a higher fin thickness, the substitute stresses in the plate reduce, as the fins can carry more load. As the substitute stress is normalized by the same value as the significantly higher total stress, it seems to remain constant for larger fin thicknesses. However, as the pressure per fin and hence the length change of the fins leading to the maximum deflection continues to decrease hyperbolically with an increasing fin thickness, the substitute stress in the plate is reduced further.

This hyperbolic trend of the substitute stress can be found in Figure 18 from [103, p. 11] as well. However, the resulting stress curve levels off slower. Especially for small fin heights, the impact of an increase in fin thickness on the plate stress gets significantly less pronounced. Overall, the derived method probably slightly underestimates the impact of increasing fin thickness on the substitute stress. However, the substitute stress for the assumed operating conditions is significantly smaller than the total stress anyway. Therefore, the possible slight underestimation of the substitute stress can be neglected in further analysis.

The segment stress decreases slightly with an increase in fin thickness. A higher fin thickness slightly reduces the cross-sectional area of a plate segment between two fins. A lower area leads to smaller bending stresses in the segment.

The effects on the resulting plate stresses are transferred to the factor of safety against yielding, as shown in Figure 5.4.

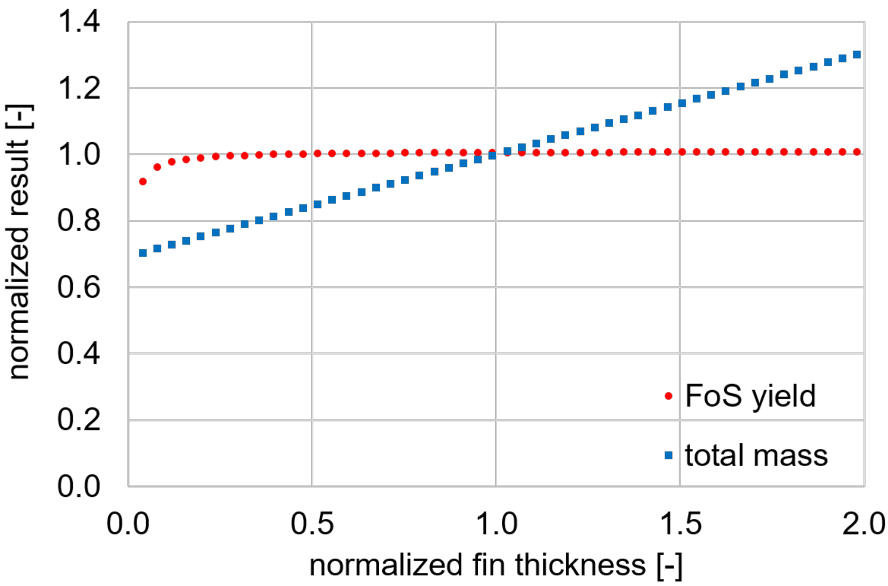

Figure 5.4: Factor of safety against yielding and total mass of PFHE with changing fin thicknesses.

As can be seen, after a certain point, the factor of safety of yielding does not change noticeably with a further increase in fin thickness. However, the mass increases linearly with an increase in fin thickness. Therefore, the structure-mechanical goal agrees with the thermodynamic goal of using thinner fins compared to thicker fins, as they offer a better heat transfer per mass.

One important aspect of the fins is their task of maintaining structural integrity. Therefore, their factor of safety with regard to buckling under compression and rupture under tension has to be taken into account as well. Both occur under different

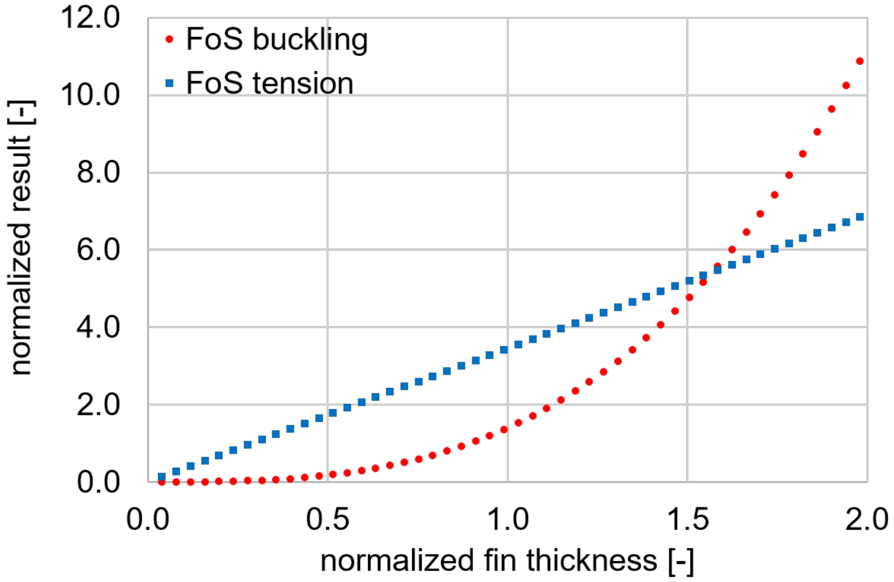

Figure 5.5: Stress components of PFHE with changing fin thicknesses (normalized by different factors).

operational conditions. Buckling occurs if the fins are stressed in compression. That happens if the plates bend towards each other. Conversely, rupture occurs if the plates bend away from each other and the fins are stressed in tension. As they describe two different operating conditions, they are not being normalized by the same factor. The occurring trends are shown in Figure 5.5.

As can be seen, decreasing the fin thickness leads to a linear decrease in the factor of safety against rupture. Furthermore, the buckling factor of safety decreases hyperbolically with decreasing fin thickness. Both are direct consequences of the used Euler equation. Therefore, the fin thickness should not fall below a limit value. Otherwise, the fins will fail.

5.1.3 Change in Fin Density

Figure 5.6 indicates the factors of safety for different fin densities chosen. The factor of safety for static yielding, buckling and tension are normalized by the same value. The total mass as well as the factors of safety indicating the stability of the fins (buckling and tension) change linearly with increasing fin density. The latter results from an increase in the number of fins, leading to more fins carrying the same load

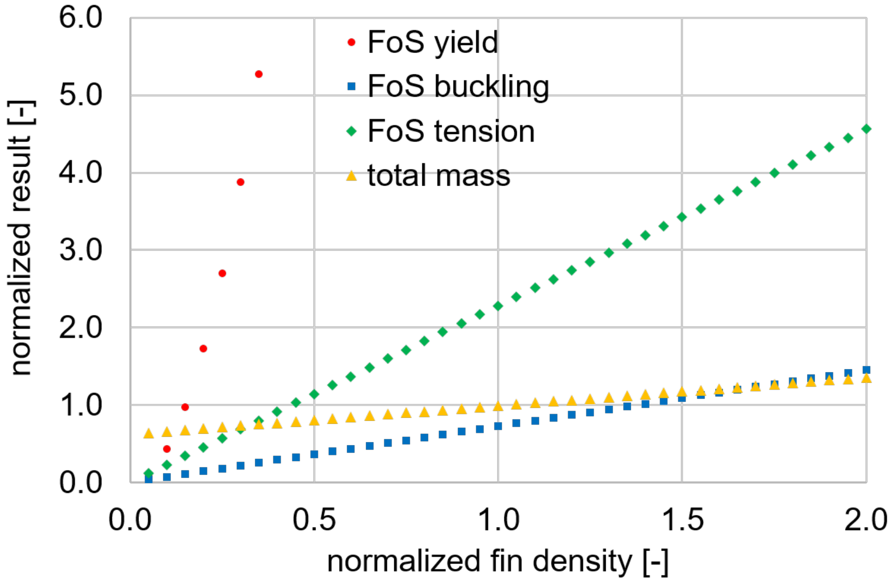

Figure 5.6: Factors of safety of PFHE with changing fin density (normalized by identical factor).

and, thus, a lower internal stress. In general, the fins are more prone to stability failure due to buckling than due to tension. Especially for low fin densities, buckling of the fins can be the design driving failure mode. Furthermore, the factor of safety against yielding increases quadratically with increasing fin density. By increasing the fin density, the dimensions of the plate segment reduce linearly, and therefore, the resulting plate segment stress reduces quadratically. The temperature stress calculated using the methods of this thesis does not change with an increasing fin thickness. Furthermore, for the assumed operating conditions, the segment stresses are significantly higher than the substitute stresses, as seen in Figure 5.5. Therefore, the characteristic of the segment stresses dominates the factor of safety against yielding, leading to the mentioned quadratic increase. However, for other operating conditions, the substitute stress can become more significant. Then, its linear increase with an increasing fin density can influence the factor of safety against yielding more than the segment stress. However, the factor of safety against yielding still increases with increasing fin density.

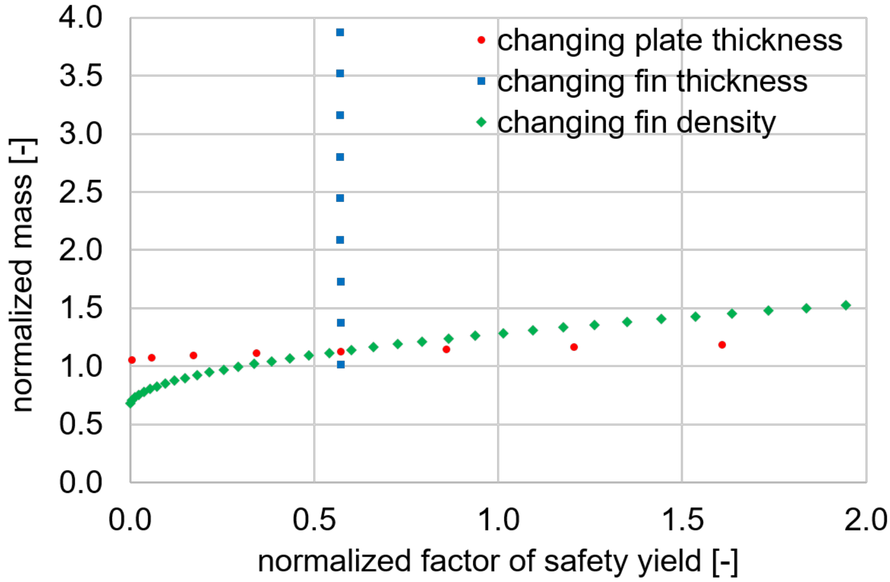

Figure 5.7: Factors of safety against static yielding and changes of mass of PFHE with changing geometric parameters (normalized by identical factor).

5.1.4 Best Design Option to Increase the Factor of Safety

The previous sections investigated the influence of three geometric parameters on the structural integrity of a PFHE. The investigation of further geometric parameters, like the height of the finned flow or the plates' dimensions, is beyond the scope of this thesis.

As the factor of safety against yielding allows a direct comparison of occurring stresses without other factors, like stress amplitude or transient overshoot factors, Figure 5.7 shows the factor of safety against yielding by changes in all three geometric parameters compared to their mass. All curves are normalized by the same value. The gradient of each curve corresponds to the mass change per change of factor of safety against static yielding. A low gradient corresponds to only a slight increase in mass for a high gain in the factor of safety. Therefore, the curve with the smallest gradient corresponds to the most optimal design option for increasing the factor of safety against static yielding. From Figure 5.7, it can be derived that it is most mass-optimal to increase the plate thickness, as its gradient is the smallest. The second best option is an increase in the fin density. Increasing the fin thickness yields no significant change in the factor of safety while steadily increasing the mass. However, as mentioned in Section 5.1.2, the impact of an increasing fin thickness is slightly underestimated. Nevertheless, the difference in the gradient from the other options is significant. Therefore, even if the impact of an increasing fin thickness would be underestimated, an increase in fin thickness would probably still be the least mass-efficient option. Additionally, increasing the fin thickness leads to a smaller heat transfer area per volume and therefore less possible total heat transfer compared to a design with a higher fin density.

Increasing the fin density leads to an increase in surface area, as more fins are present in the flow passage. Therefore, it enhances heat transfer. Taking both the thermodynamics and the structural mechanics into perspective, it could thus be beneficial to increase the fin density instead of the plate thickness. However, considerations regarding the pressure as well as the blockage of the flow channel, which increases with an increasing fin density, are required.

Furthermore, manufacturers typically provide standard thicknesses. Hence, the optimal plate thickness could be a thickness that is not manufacturable. This could be due to the precision of the manufacturing process. Therefore, a combination of both a varying plate thickness and a varying fin density can be a practicable solution to obtain the required factors of safety while still being manufacturable.

While generally, the rupture of the fins is not design-limiting, buckling can be a critical failure mode. Therefore, its behavior is investigated as well. Figure 5.8 shows the changes in the buckling factor of safety.

As can be seen, here, an increase in plate thickness has no significant impact on the factor of safety of buckling due to the chosen modeling approach. In reality, increasing the plate thickness would lead to a smaller compressive load acting on the fins, as the plates can carry more load compared to a thinner plate. However, the effect is still expected to be smaller than changing the fin geometry. Hence, it is not considered an adequate measure to increase the stability of the structure. It mainly depends on the fin thickness and density. While for low normalized buckling factors of safety, the gradient of the fin thickness curve is higher, the characteristic changes for higher normalized buckling factors of safety. The mass-optimal parameter for increasing the buckling resistance of the fins can thus vary between their thickness and density.

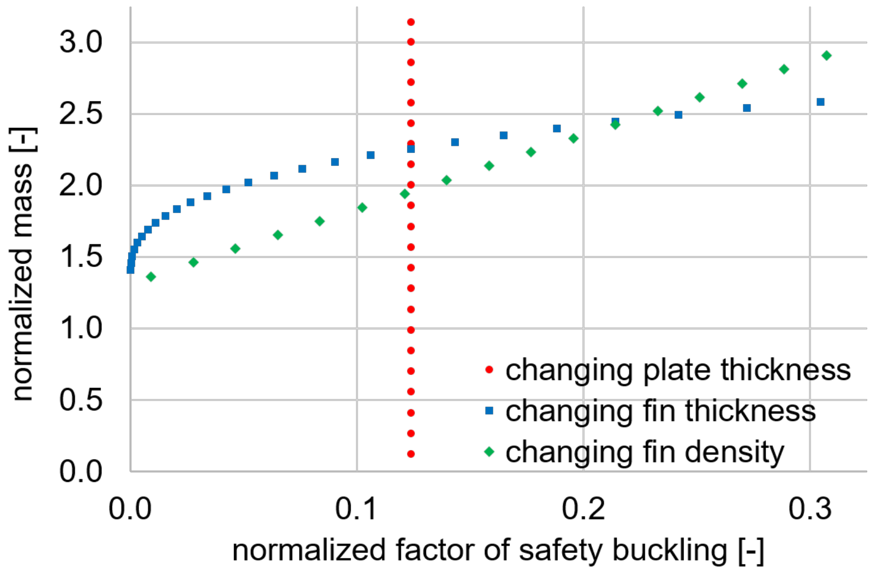

Figure 5.8: Factors of safety against buckling and changes of mass of PFHE with changing geometric parameters (normalized by identical factor).

However, as mentioned above, increasing the fin density would probably be the preferred method. It increases the possible heat transfer area and reduces the stresses on the plate. Interdependencies between the fin thickness and the fin density regarding the stability against buckling exist. Both the fin density and their thickness influence the stability of the fins. Therefore, when ensuring the stability of the fins, both a very low number of fins and a very low fin thickness must be avoided.

Using the tool and conducting a grid search optimization with given operational parameters for a minimum mass while varying the three mentioned geometric parameters shows exactly the described behavior. If one wants to increase the factor of safety of the plate (e.g. when the fins are stressed under tension and rupture is not design-limiting), the fin thickness should be chosen as low as possible. The plate thickness is increased. However, as the mathematical optimum lies between the step size defined in the grid search, the fin density is increased. Therefore, the resulting heat exchanger geometry includes a certain plate thickness, a fin density between the minimum and maximum defined in the grid search and a fin thickness as low as possible. However, when optimizing a geometry in which the fins are stressed in compression, the buckling resistance plays a significant role. The resulting design features a medium fin density as well as fin thickness.
In general, designs with the fins stressed in compression lead to higher required mas-

ses than designs where the fins are stressed in tension. While this assumes the fins to be bars, this should hold for rectangular, thin plates as well. The buckling criteria is more critical than tensile rupture, as the buckling is a function of structural stability and not the material strength. Typically, the structural stability is lower than the material strength.

5.2 Tube Bundle Heat Exchanger

This section investigates the changes in the factor of safety against yielding when varying three geometric parameters. First, the influence of the tube thickness is discussed. Then, the influence of changing bend radii of the tubes is investigated. Furthermore, the influence of a changing inner diameter of the tube is explored. Finally, the best design option of the TBHE for reaching a certain factor of safety is assessed.

5.2.1 Change in Tube Thickness

The tube thickness is the first geometric parameter of the TBHE investigated. Figure 5.9 shows the normalized factor of safety and mass of the TBHE for different tube thicknesses.

As can be seen, the factor of safety first increases significantly before asymptotically tending to a certain value. The mass generally increases more significantly for higher tube thicknesses. This is a consequence of the mass calculation involving the derivation of the cross-sectional area of a circular ring, as already explained in Section 4.2.1.

The factor of safety curve can be explained by looking at the stresses resulting in the tube, shown in Figure 5.10. In general, the temperature stresses in the radial direction are zero at the inner wall, which is where the maximum total stress occurs. The pressure stress at the inner wall in the radial direction remains constant for all tube thicknesses and is equal to the inner pressure, which is independent of geometrical parameters. The temperature stresses in the circumferential direction increase logarithmically. However, as they are significantly smaller than the pressure

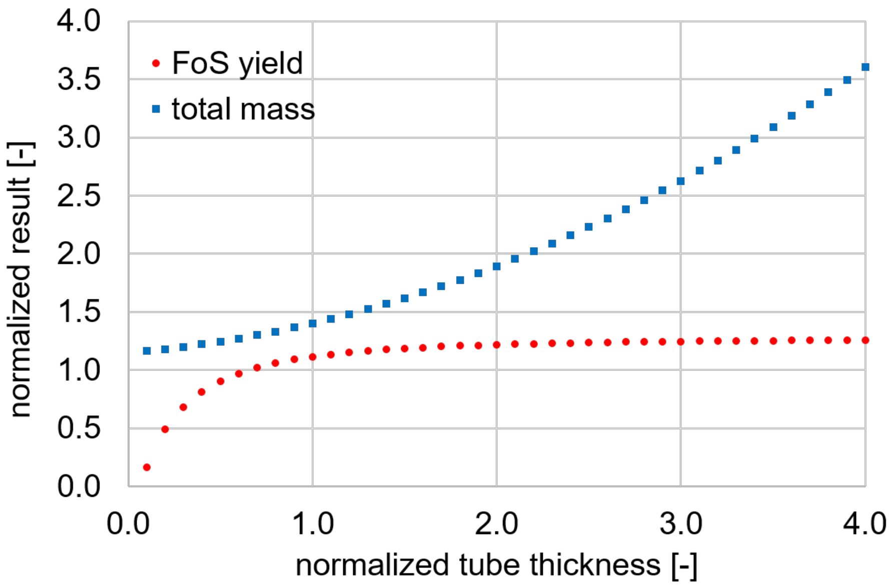

Figure 5.9: Factors of safety against yielding and changes of mass of TBHE for changing tube thicknesses.

stresses, they are not shown in the figure either. The total stress, thus, is similar to the circumferential pressure stress.

The circumferential pressure stress decreases with increasing tube thickness. This behavior is expected, as more material is available onto which the load can distribute itself. However, the circumferential pressure stress decreases hyperbolically. For low tube thicknesses, an increase in the tube thickness leads to a better load distribution in the radial direction. However, for large tube thicknesses, the stress peak, which occurs at the inner wall, does not change noticeably anymore, as the additional material does not carry any pressure loads. The pressure is already completely carried by the inner part of the tubes.

The stress intensification factor due to the bend decreases hyperbolically for low tube thicknesses. However, beyond a certain threshold, the stress intensification factor of the bend would fall below 1, as explained in Section 3.2.6.3. Hence, a stress intensification factor of 1 is used, corresponding to the straight part of the tubes. In this case, the total stress before and after applying the stress intensification factor is identical.

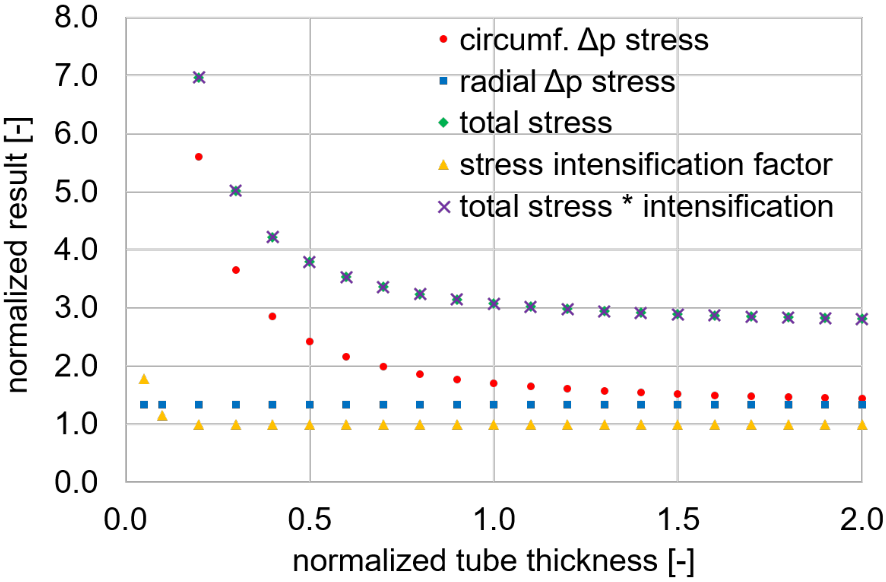

Figure 5.10: Pressure, total stresses and stress intensification factor of TBHE for changing tube thicknesses (stresses normalized by identical factor).

The goal of this study was to see the effect of changing tube thicknesses. The fin height and fin width, defined by SL and ST have been assumed to be constant. Furthermore, the number of tube cross-sections, defined by n_p and n_t, was assumed to be constant. The outer diameter and hence the maximum tube thickness is thus limited by the geometry of the fins. SL and ST were thus derived based on the maximum outer diameter, which corresponds to the maximum thickness. For thinner tubes, this leads to shallow bends. The stress intensification factor of the bend hence drops quickly below 1, as a small thickness is sufficient to counteract the stress concentrations due to the shallow bend. A stress intensification factor of 1 is used in this case.

Investigating the tube thickness with varying SL and ST would lead to completely different designs with significantly varying heat transfer areas of the fins. These studies would only be possible when using a multidisciplinary approach and comparing other metrics, e.g. designs with varying geometrical parameters but identical heat transfer capabilities. This would help assess the influence of a changing thickness on the fluid- and thermodynamic behavior. While the fin geometry has a significant impact on the heat transfer area, the thicker tubes influence the fluid- and thermodynamics as well. Thicker tubes lead to increased thermal resistance and an increased pressure drop [107].

The factor of safety can be increased significantly by increasing the tube thickness up until a certain point. In this case, the total mass does not change significantly. However, thereafter, an increase in tube thickness does not yield a further stress relief, but a significant mass increase. Other measures are required.

5.2.2 Change in Bend Radius SL

The bend radius SL describes the vertical distance between two adjacent tubes, as shown in Figure 3.2. The yield factor of safety, as well as the changes in mass and fin height, are shown in Figure 5.11. With an increasing bend radius, the stress

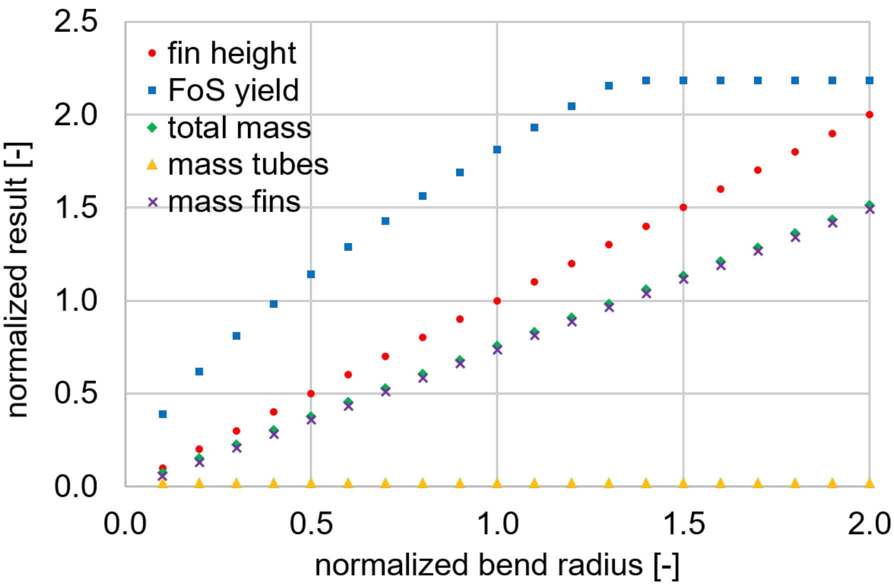

Figure 5.11: Factor of safety against static yielding as well as mass and fin height of the TBHE for changing bend radii (masses normalized by identical factor).

concentrations in the bend reduce. This is shown by the increasing yield factor of safety, depicted in red. The impact of the bend radius on the factor of safety is stronger for small bend radii. Especially in the case of tight bends, increasing the bend radius can thus be a practicable measure to reduce stresses. However, this can only be done until a certain threshold. After crossing it, the bend is too shallow for a negligible stress concentration to occur. Therefore, the factor of safety against yielding cannot be changed by increasing the bend radius further.

Changing the bend radius influences the total mass. The mass of the tube remains approximately constant; its changes stem from the changing additional length of the tube required for the bend. However, compared to the mass of the fins and tubes, this additional mass is significantly smaller. The mass of the fins however increases linearly with increasing bend radii, as the height of the fins increases. The fin height is defined by the number of passages as well as the bend radius. The latter indicates the vertical distance between two adjacent tubes. Increasing the bend radius thus shifts the tubes further apart. In this study, the number of tube passages is fixed. Therefore, the fins' size increases. While the mass of the tubes dominates the total mass for small bend radii, it shifts towards a more dominant fin mass for higher bend radii.

Besides the influence of the mass, the influence of the fin height on the geometry is significant. Doubling the bend radius leads to fins twice as high. Heat exchangers for aero engines are typically designed in a compact way, as design space is sparse in aero engines. Doubling the size of the fins involves a significant change in the geometry of the heat exchanger and, hence, the aero engine.

Increasing the bend radius may be a proper design choice for decreasing the occurring stresses if the fin geometry is fixed and the bend radius is very small. Furthermore, increasing the fin height leads to a larger heat transfer area of the fins. If the geometry of the fins is predefined and the bend radius does not influence fin height, it should be chosen as large as possible to ease stress concentrations. However, if the bend radius SL is used to size the fins, it should be chosen as small as possible to avoid a significant mass increase due to an increase in fin height.

Changing the bend radius influences the fluid- and thermodynamic behavior of the tubes as well. With larger bend radii, the longitudinal spacing between the tubes grows. Increasing the distance between the tubes leads to a decreased pressure drop. Furthermore, positioning the tubes closer together can lead to an increased flow velocity of the gas flowing through the tubes. If turbulence occurs, heat transfer can be enhanced. Additionally, a larger spacing between the tubes means that fewer tubes fit into a given space, and hence, the heat transfer area is reduced. From a thermodynamic perspective, one generally wants to maximize the number of tubes and, hence, minimize the distance between tubes. However, choosing a too small distance leads to difficulties regarding the cleaning and can increase the risk of plugging [108].

5.2.3 Change in Diameter

Another geometric property influencing the stresses in the tube and hence the factor of safety against yielding is the diameter of the tube. Within the methodology developed in this thesis, the inner diameter and the tube thickness are user inputs, whilst the outer diameter is calculated based on them. As the inner and outer diameters are coupled by the thickness, the results when varying the inner diameter and the outer diameter would be identical. In this study, the change in the inner diameter is investigated. Figure 5.12 shows the resulting factor of safety against yield for different inner diameters.

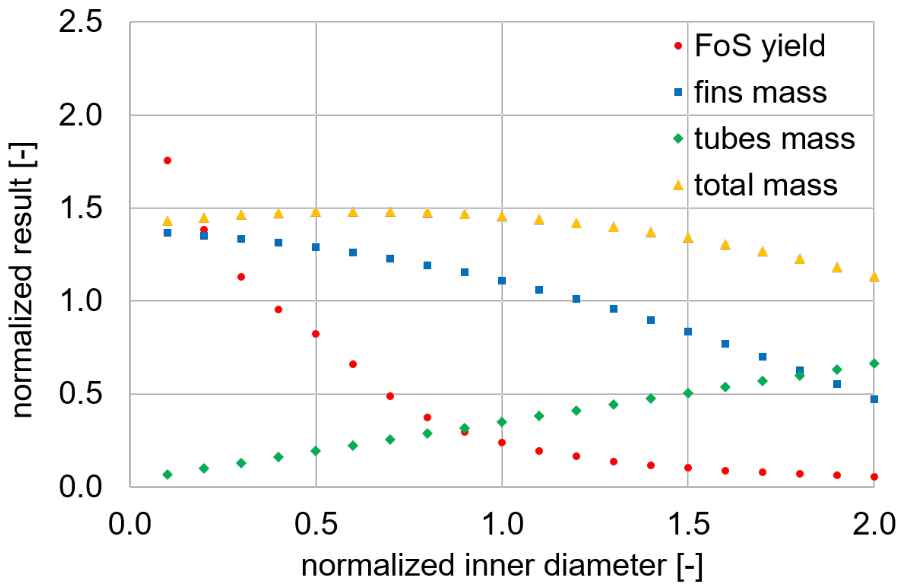

Figure 5.12: Factor of safety against static yielding and mass of the TBHE for changing inner diameter.

Increasing the inner diameter leads to a hyperbolic decrease in the factor of safety. The pressure stress acts on the surface area of the tube. The surface area of an infinitesimal small tube segment, defined by $\pi \cdot d_i$, increases faster than the cross-sectional area, defined by $\frac{\pi}{4} \cdot (d_o^2 - d_i^2)$, as $d_o^2 - d_i^2 = (d_i + 2 \cdot t)^2 - d_i^2 = 4 \cdot d_i \cdot t + 4 \cdot t^2$ and $t \ll d_i$. Therefore, the induced total force, defined by the surface area, increases faster than the ability to withstand the load, characterized by the cross-sectional area. While an increasing inner diameter leads to a larger cross-sectional area and, hence, a larger mass, the factor of safety actually decreases.

The total mass increases for small inner diameters. However, after crossing a certain threshold, it decreases with an increasing inner diameter. This is due to the interaction between the mass of the fins and the mass of the tubes. For the calculation of the tubes' mass, the cross-sectional area of the tube is used. By subtracting the area defined by the inner diameter, $\pi \cdot (\frac{d_i}{2})^2$, from the area defined by the outer diameter, $\pi \cdot (\frac{d_o}{2})^2 = \pi \cdot (\frac{d_i+2\cdot t_t}{2})^2$, the quadratic term d_i cancels out. This results in a linear relationship between the inner diameter and the cross-sectional area of the tubes.

However, with an increasing inner diameter, the mass of the fins reduces as the perforations in the fin induced by the tubes increase. The inner diameter is hence dependent on the geometry of the fins as well as the tubes. It occurs if the mass increase in the tubes is equal to the mass decrease in the fins due to the large perforations. Using the equations introduced in Section 3.2.3, the maximum occurs for $d_i = \frac{(2-2\cdot FD\cdot t_{ft})\cdot t_t}{FD\cdot t_{ft}}$. The critical inner diameter is thus dependent on the thickness of the tube as well as the thickness of all fins combined, defined by $FD \cdot t_{ft}$. If the thickness of all fins combined is larger, it occurs earlier. However, for a large tube thickness, the gradient of the tubes' mass is larger, and hence, the maximum of the total mass occurs later. A typical heat exchanger geometries with $t_{ft} \ll t_t$, medium values of FD and $t_t \ll d_i$, would generally lead to a mass increase with increasing inner diameter. However, further increases in the inner diameter can lead to a reduced mass but a significant decrease in the factor of safety.

Looking at the yielding factor of safety, a small tube diameter is strived for. However, decreasing the tube diameter significantly influences the flow behavior of both the inner flow and the outer flow. It slightly decreases the pressure drop due to less blockage of the outer flow. However, the effect of erosion inside the tube, which is not assessed in this thesis, can increase due to a higher fluid velocity. The heat exchange is significantly influenced by the tube diameter as well. Increasing it leads to an increase in heat transfer area but a decrease in flow velocity, following the continuity equation. This decreases the Reynolds number as well, indicating the influence on the flow behavior.

Based on the methods included, a minimal diameter would be beneficial for structural integrity. In practice, however, the inner diameter needs to be adjusted to the operational parameters and the required heat transfer while being able to withstand the structural loads in all occurring operating conditions.

5.2.4 Best Design Option to Increase the Factor of Safety

Figure 5.13 compares the three options to influence the structural integrity, as presented above.

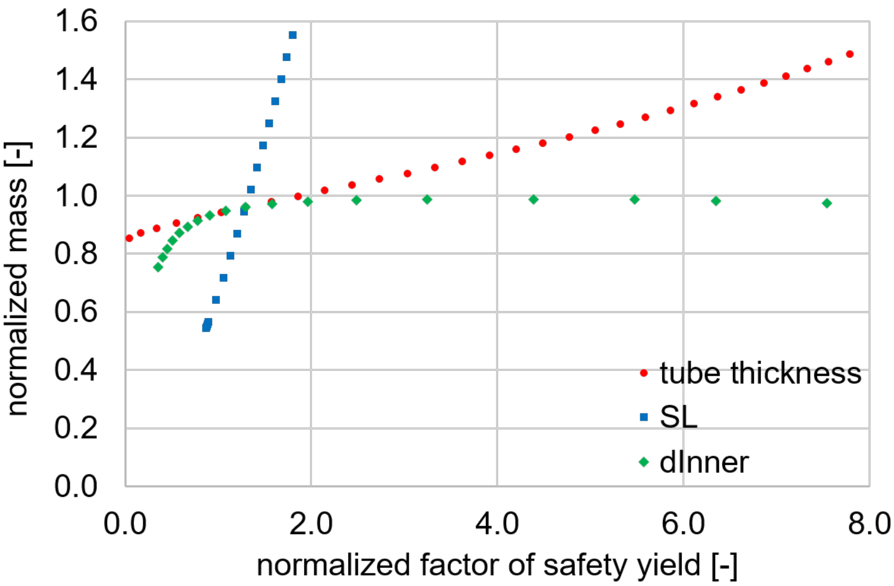

Figure 5.13: Factor of safety against yielding and mass of the TBHE for changing geometric parameters (normalized by identical factor).

Increasing the yield factor of safety by adjusting the inner diameter first leads to a significant mass increase, but for larger factors of safety, the mass decreases again, leading to a slight negative gradient. This has already been explained in Section 5.2.3. A higher factor of safety against yielding can thus be achieved by minimizing the inner diameter, as a smaller inner diameter leads to an increase in the factor of safety against yielding and mass decrease. Furthermore, due to the steep gradient of the bend radius curve, a bend radius as low as possible is desired, as a decrease in bend radius leads to a smaller mass. The gradient of the tube thickness is approximately linear. It is smaller than the gradient of the bend radius SL, but especially for higher factors of safety, larger than the gradient of changes in the inner diameter.

From a structural standpoint, all designs should have a diameter as small as possible. If the stresses of the tube would be too high, it would be most effective to increase the tube thickness. The bend radius should be chosen as small as possible.

Conducting a grid search optimization on all three parameters for given operating conditions shows the same behavior. A design with the smallest bend radius and inner diameter, but an increased tube thickness leads to the most mass-efficient design. A design with a minimum tube thickness and inner diameter but a higher bend radius leads to a lower factor of safety against yielding and a significant additional mass.

However, changing the bend radius might be a valuable option. In the study presented above, the bend radius SL defined the required fin height. However, if the fin height is higher than structurally required, be it due to manufacturing purposes or thermodynamic reasons, increasing the bend radius does not change the mass significantly. Furthermore, if unexpectedly higher stresses occur but the tube thickness and diameter are already fixed, the bend radius can be used to decrease the stresses by increasing the bend radius.

Whilst the findings above are explicitly related to the structural-mechanic characteristic of the TBHE, it is necessary to consider the impact of varying geometrical parameters on the flow behavior and thermodynamics of the TBHE as well. An optimal structural-mechanic design featuring a small bend radius and inner diameter with a larger thickness could lead to erosion inside the tubes due to a higher flow velocity as well as smaller fins and a thicker tube, which could hinder the heat transfer ability. A multidisciplinary approach is thus required to optimize a design.

6 Conclusion and Outlook

6.1 Conclusion

High performant heat exchangers are needed in novel aero engines. They can fail due to various factors such as corrosion, static stress, LCF, HCF, creep or interactions between different failure modes. In this thesis, simplified methods have been developed to assess the structural integrity of heat exchangers.

Most of the methods suited for Plate-Fin Heat Exchanger could be verified. Due to the lack of examples in literature and suitable FEM analyses, some assessment methods could not be verified. A plausibility check as well as sensitivity studies regarding these methods have been conducted. Overall, the derived methods capture pressure and gravitational stresses well, but they are unable to adequately assess all temperature stresses. On the other hand, the methods developed for Tube Bundle Heat Exchanger have been validated and show good agreement with FEM analyses. These methods cover both pressure and temperature stresses and provide a reliable means for stress and lifetime estimation in accordance with industry norms.

The design driving failure mode for Plate-Fin Heat Exchangers depends on operating conditions, lifetime, and assumed input variables such as transient overshoot factors or lump sum stress amplitudes for HCF. Generally, the structural-mechanic design driving failure mode for Plate-Fin Heat Exchanger is HCF, while LCF becomes more dominant for higher plate stresses. However, static strength is not considered design-driving for the investigated boundary conditions and material. For Tube Bundle Heat Exchangers, the design driving failure mode is creep for large lifetimes, high wall temperatures, and high pressure differences. LCF can become design-driving for large transient stresses, while HCF is significant for high stress amplitudes. Yielding is the dominant design driver for lower lifetimes, wall temperatures, and pressure differences.

The influence of various parameters on the behavior of the failure modes has been investigated. Corrosion is one of the most critical failure modes due to its significant impact on mass due to the additional required wall thickness. If one wants to avoid the additional wall thickness, protective coatings or other constructive measures can be developed.

In Plate-Fin Heat Exchanger, the stress in the plate can be reduced by increasing the plate thickness and/or fin density. Increasing the plate thickness is more mass-efficient while increasing the fin density offers thermodynamic benefits such as increased heat transfer area. The static stability, including buckling under compression and rupture under tension, can be improved by using thicker fins or a higher fin density.

In a Tube Bundle Heat Exchanger, the stress levels can generally be decreased by increasing the tube thickness, reducing the bend radius, and/or decreasing the inner diameter. Decreasing the inner diameter is the most mass-efficient option but is limited by manufacturing and fluid dynamic considerations. Increasing the tube thickness leads to lower resulting stresses while increasing mass. Changing the bend radius reduces stress concentrations in the tubes but increases the fin height, resulting in significant mass and overall dimension changes. However, if the overall fin height is predetermined and tube specifications are already set, changing the bend radius can be a viable solution to address higher-than-expected stresses.

Overall, this thesis provides valuable insights into the failure modes and design considerations for Plate-Fin Heat Exchanger and Tube Bundle Heat Exchanger. The developed methods and findings can serve as a foundation for further research and optimization in the design and structural integrity assessment of heat exchangers.

6.2 Outlook

Overall, the methodology presented in this thesis provides a solid assessment of the structural-mechanical aspects of heat exchangers. However, there are several areas that require further investigation and improvement.

Further work is required to accurately assess temperature stresses in the Plate-Fin Heat Exchanger. The effect of two-dimensional temperature fields on the resulting stresses needs to be assessed more thoroughly. The accuracy of the LCF calculation method needs to be further investigated, e.g., by using identical material data for the methods derived in this thesis and industry data. In addition, input parameters such as corrosion rates, transient stresses, and vibrational stresses should be investigated and determined more accurately. These parameters have a significant impact on the performance and lifespan of the heat exchanger and should be properly accounted for in the assessment.

To further verify the methods used in this thesis, FEM analyses can be utilized, potentially by employing the so-called homogenization method. This will also provide a more detailed and comprehensive understanding of the structural characteristics of the heat exchanger.

As corrosion is one of the most critical failure modes, the development of proper protective coatings, which can be used in heat exchangers, is required. If corrosion is expected in a certain area, this area could be made of a more corrosion-resistant material, like zirconium. Further research has to be conducted on the combination of different materials in one heat exchanger.

Erosion, which can lead to significant reductions in material thickness, was not assessed in this thesis. Developing proper assessment methods for erosion that can be used in the preliminary design stage is necessary to ensure the integrity over the whole lifetime of the heat exchanger.

Furthermore, while this thesis is focused on the major components, such as plates or tubes, it is important to investigate other components, such as headers or nozzles, separately. These components may experience higher stresses and require specific design considerations.

Interactions between different disciplines, including thermodynamics, structural mechanics, and fluid dynamics, play a significant role in heat exchanger design. This thesis primarily focused on the structural-mechanical aspects, but a multidisciplinary integration of all domains is crucial for a holistic assessment of heat exchanger geometry and further studies.

7 References

[1] O. Schmitz, H. Klingels, and P. Kufner, "Aero Engine Concepts Beyond 2030: Part 1 — The Steam Injecting and Recovering Aero Engine," in *Volume 5: Controls, Diagnostics, and Instrumentation; Cycle Innovations; Cycle Innovations: Energy Storage*. American Society of Mechanical Engineers, 2020.

[2] R. K. Shah and D. P. Sekulić, *Fundamentals of heat exchanger design*. Hoboken, NJ: Wiley-Interscience, 2003. [Online]. Available: http://onlinelibrary.wiley.com/book/10.1002/9780470172605

[3] M. Weisser, "Erstellung und Implementierung eines erweiterten regelbasierten Verfahrens zur Schaufelauslegung mit Kühlluftmengenbestimmung in der Triebwerksvorauslegung," Diploma thesis, Universität Stuttgart, Stuttgart, 2010. [Online]. Available: https://mtu.wissensbank.com/qlinkdb/cat/ID=498898000

[4] Sigmund, "Schematic appearance of round metal bars after tensile testing," 2008. [Online]. Available: https://en.wikipedia.org/wiki/Ductility#/media/File:Ductility.svg

[5] H. Schoenenborn, E. Ebert, B. Simon, and P. Storm, "Thermomechanical Design of a Heat Exchanger for a Recuperative Aeroengine," *Journal of Engineering for Gas Turbines and Power*, vol. 128, no. 4, pp. 736–744, 2006.

[6] S. Boggia and K. Rüd, "Intercooled Recuperated Gas Turbine Engine Concept," in *41st AIAA/ASME/SAE/ASEE Joint Propulsion Conference & Exhibit*. Reston, Virigina: American Institute of Aeronautics and Astronautics, 2005.

[7] R. Bürgel, *Handbuch Hochtemperatur-Werkstofftechnik: Grundlagen, Werkstoffbeanspruchungen, Hochtemperaturlegierungen*, ser. Springer eBook Collection Life Science and Basic Disciplines. Wiesbaden and s.l.: Vieweg +Teubner Verlag, 1998.

[8] G. L. Ferguson and S. R. Gullapalli, “Thermo-elastic finite element fatigue failure analysis,” *Engineering Failure Analysis*, vol. 2, no. 3, pp. 197–207, 1995.

[9] S. Kulkarni, “Coupling of peridynamics and the finite element method and Study of the damping property of polymer composites,” PhD Thesis, Pacific Northwest National Laboratory, Richland, 2019.

[10] M. Tsuda and N. Ohno, “Duplex model for homogenized elastic–viscoplastic behavior of plate–fin structures at high temperatures,” *International Journal of Plasticity*, vol. 27, no. 10, pp. 1560–1576, 2011.

[11] L. Ge, W. Jiang, Y. Zhang, and S.-T. Tu, “Analytical evaluation of the homogenized elastic constants of plate-fin structures,” *International Journal of Mechanical Sciences*, vol. 134, pp. 51–62, 2017.

[12] L. Ge, W. Jiang, Y. Wang, and S.-T. Tu, “Creep-fatigue strength design of plate-fin heat exchanger by a homogeneous method,” *International Journal of Mechanical Sciences*, vol. 146-147, pp. 221–233, 2018.

[13] A. Al-Turaihi, Q. H. Bader, and A. Basim, “Notch Effect on Aluminium Alloy Rod under Rotating Bend Fatigue Load,” *IOP Conference Series: Materials Science and Engineering*, vol. 1094, no. 1, 2021.

[14] P. Schaldenbrand, “The Goodman-Haigh Diagram for Infinite Life,” 2019. [Online]. Available: https://community.sw.siemens.com/s/article/the-goodman-haigh-diagram-for-infinite-life

[15] R. K. Singh and J. K. Sahu, “Influence of hold type and duration on cyclic deformation behaviour of IN740H,” *Materials Science and Technology*, vol. 35, no. 4, pp. 488–499, 2019.

[16] International Civil Aviation Organization, “States adopt net-zero 2050 global aspirational goal for international flight operations,” 2022. [Online]. Available: https://www.icao.int/Newsroom/Pages/

States-adopts-netzero-2050-aspirational-goal-for-international-flight-operations.aspx

[17] European Commission, Directorate-General for Climate Action, "Updated analysis of the non-CO2 climate impacts of aviation and potential policy measures pursuant to EU Emissions Trading System Directive Article 30(4)." [Online]. Available: https://eur-lex.europa.eu/legal-content/EN/TXT/PDF/?uri=CELEX:52020SC0277

[18] Air Transport Action Group, "Tracking Aviation Efficiency: Fact Sheet #3." [Online]. Available: https://aviationbenefits.org/media/167475/fact-sheet_3_tracking-aviation-efficiency-v2.pdf

[19] Airports Council International, "ACI World Airport Traffic Forecasts 2023-2052: Executive Summary," Montreal. [Online]. Available: https://store.aci.aero/wp-content/uploads/2024/02/WATF-Executive-Summary.pdf

[20] H. Grieb, *Projektierung von Turboflugtriebwerken*, ser. Technik der Turboflugtriebwerke. Basel and s.l.: Birkhäuser Basel, 2004.

[21] E. D. Larson and R. H. Williams, "Steam-Injected Gas Turbines: FU/CEES Report No. 200." [Online]. Available: https://acee.princeton.edu/wp-content/uploads/2022/08/Larson-Steam-Injected-Gas-Turbines-1985-1.pdf

[22] M. Jonsson and J. Yan, "Humidified gas turbines—a review of proposed and implemented cycles," *Energy*, vol. 30, no. 7, pp. 1013–1078, 2005.

[23] D. S. Boman and W. E. Mallett, "Investigation of thrust augmentation using water-alcohol injection on a 5200-pound-thrust axial-flow-type turbojet engine at static sea-level conditions." [Online]. Available: https://digital.library.unt.edu/ark:/67531/metadc64687/m2/1/high_res_d/19930090414.pdf

[24] R. Pouzolz, O. Schmitz, and H. Klingels, "Evaluation of the Climate Impact Reduction Potential of the Water-Enhanced Turbofan (WET)

Concept," *Aerospace*, vol. 8, no. 3, 2021. [Online]. Available: https://www.mdpi.com/2226-4310/8/3/59

[25] S. Kaiser, O. Schmitz, P. Ziegler, and H. Klingels, "The Water-Enhanced Turbofan as Enabler for Climate-Neutral Aviation," *Applied Sciences*, vol. 12, no. 23, 2022.

[26] P. Ziegler, S. Kaiser, and V. Gümmer, "Parametric Cycle Studies of the Water-Enhanced Turbofan Concept," in *Volume 5: Cycle Innovations*, ASME, Ed. American Society of Mechanical Engineers, 2023. [Online]. Available: https://asmedigitalcollection.asme.org/GT/proceedings/GT2023/86984/V005T06A001/1168010

[27] Merim Sakic and Michal Nitulescu, "Steam generation and exhaust water recovery for the Water Enhanced Turbofan (WET)," Master's Thesis, Chalmers University of Technology, Gothenburg, 2021. [Online]. Available: https://odr.chalmers.se/server/api/core/bitstreams/00867b2d-4d9c-4b6b-85cd-8fc5ffedddbd/content

[28] F. Herbertsson, "Modelling and simulation of the Water Enhanced Turbofan concept," Master's Thesis, Chalmers University of Technology, Gothenburg, 2024. [Online]. Available: https://odr.chalmers.se/server/api/core/bitstreams/0581e61a-b956-4335-8252-b4a026cf3fec/content

[29] G. Zhou, Y. Ye, J. Wang, W. Zuo, Y. Fu, and X. Zhou, "Modeling air-to-air plate-fin heat exchanger without dehumidification," *Applied Thermal Engineering*, vol. 143, pp. 137–148, 2018.

[30] M. Hajek, "Lecture: Safety and Certification of Aircraft: Safety assessment process," 2023. [Online]. Available: https://www.moodle.tum.de/pluginfile.php/4548971/mod_resource/content/1/4%20-%20Safety%20assessment%20process.pdf

[31] ASM International, *Properties and selection: Stainless steels, tool materials and special-purpose metals*, 9th ed., ser. Metals handbook / prepared under

the direction of the ASM Handbook Committee. Metals Park, Ohio: American Society for Metals, 1985, vol. Vol. 3.

[32] H.-C. Qua, C.-S. Tan, K.-C. Wong, J.-H. Ho, X. Wang, E.-H. Yap, J.-B. Ooi, and Y.-S. Wong, *Applied engineering failure analysis: Theory and practice*, 1st ed. Boca Raton, Florida: CRC Press, 2015. [Online]. Available: https://permalink.obvsg.at/

[33] H.-Y. Woo, G.-S. Lim, W.-B. Kim, W.-S. Choi, S.-H. Cho, K.-T. Park, and J.-H. Lee, "Isothermal and cyclic corrosion behaviour of Ni-based alloys in an electrochemical reduction process," *Corrosion Engineering, Science and Technology*, vol. 56, no. 6, pp. 513–521, 2021.

[34] CSNI, "Collection and Analysis of Common-cause Failures of Heat Exchangers: International Common-cause Failure Data Exchange (ICDE) Project Report April 2013."

[35] Marvin P. Schwartz, "Four Types of Heat Exchanger Failures," *Plant Engineering*, 1982. [Online]. Available: https://www.researchgate.net/profile/Dzevad-Hadzihafizovic-2/publication/374839345_Type's_Of_Heat_Exchanger_Failure'spdf/data/653139271d6e8a70703caa5f/Types-Of-Heat-Exchanger-Failures.pdf

[36] J. Boyer and J. Klimek, "Avoid Costly Failures Of Shell-And-Tube Heat Exchangers: Understand the most common causes and how to prevent them," 2020. [Online]. Available: https://www.chemicalprocessing.com/utilities-energy/heat-transfer-fluids/article/11298420/avoid-costly-failures-of-shell-and-tube-heat-exchangers-chemical-processing

[37] M. Ali, A. Ul-Hamid, L. M. Alhems, and A. Saeed, "Review of common failures in heat exchangers – Part I: Mechanical and elevated temperature failures," *Engineering Failure Analysis*, vol. 109, 2020.

[38] T. M. Ahmed, A. Alfantazi, J. Budac, and G. Freeman, "Failure analysis of 316L stainless steel tubing of the high-pressure still condenser," *Engineering*

Failure Analysis, vol. 16, no. 5, pp. 1432–1441, 2009.

[39] Deutsches Institut für Normung, “DIN EN 13445-3:2021-12, Unbefeuerte Druckbehälter - Teil 3: Konstruktion; Deutsche Fassung,” Berlin.

[40] W. Faes, S. Lecompte, Z. Y. Ahmed, J. van Bael, R. Salenbien, K. Verbeken, and M. de Paepe, “Corrosion and corrosion prevention in heat exchangers,” *Corrosion Reviews*, vol. 37, no. 2, pp. 131–155, 2019.

[41] A. Dwijayanti and K. Kolmetz, “Pressure Vessel Selection, Sizing And Troubleshooting,” *Kolmetz Handbook Of Process Equipment Design*, 2020.

[42] M. Stewart, “Mechanical Design of Pressure Vessels,” in *Gas-Liquid And Liquid-Liquid Separators*. Elsevier, 2008, pp. 175–203.

[43] W. Sölken, “Effects and Economic impact of Corrosion,” 2010. [Online]. Available: https://www.wermac.org/materials/corrosion_allowance.html

[44] Tubular Exchanger Manufacturers Association, Inc., “Standards of the Tubular Exchanger Manufacturers Association,” New York, 2007.

[45] Z. Ahmad, *Principles of corrosion engineering and corrosion control*, 1st ed., ser. IChemE series. Amsterdam and Heidelberg: Elsevier Butterworth-Heinemann, 2006.

[46] S. Kakaç, H. Liu, and A. Pramuanjaroenkij, *Heat Exchangers: Selection, Rating, and Thermal Design, Third Edition*, 3rd ed. Hoboken: CRC Press, 2012.

[47] S. Addepalli, D. Eiroa, S. Lieotrakool, A.-L. François, J. Guisset, D. Sanjaime, M. Kazarian, J. Duda, R. Roy, and P. Phillips, “Degradation Study of Heat Exchangers,” *Procedia CIRP*, vol. 38, pp. 137–142, 2015.

[48] K. Li, J. Wen, H. Yang, S. Wang, and Y. Li, “Sensitivity and stress analysis of serrated fin structure in plate-fin heat exchanger on cryogenic condition,” *International Journal of Thermal Sciences*, vol. 145, 2019.

[49] M. H. Saggu, N. A. Sheikh, U. M. Niazi, M. Irfan, and A. Glowacz, "Predicting the Structural Reliability of LNG Processing Plate-Fin Heat Exchanger for Energy Conservation," *Energies*, vol. 13, no. 9, 2020.

[50] H. Ma, W. Cai, W. Zheng, J. Chen, Y. Yao, and Y. Jiang, "Stress characteristics of plate-fin structures in the cool-down process of LNG heat exchanger," *Journal of Natural Gas Science and Engineering*, vol. 21, pp. 1113–1126, 2014.

[51] R. Hölzl, "Lifetime Estimation of Aluminum Plate Fin Heat Exchangers," in *Volume 3: Design and Analysis.* American Society of Mechanical Engineers, 2012, pp. 871–875.

[52] R. Hölzl and R. Flüggen, "Experimental Fatigue Evaluation of Aluminum Brazed Plate Fin Heat Exchangers," in *Volume 3: Design and Analysis.* American Society of Mechanical Engineers, 2013.

[53] P. Carter, T. J. Carter, and A. Viljoen, "Failure analysis and life prediction of a large, complex plate fin heat exchanger," *Engineering Failure Analysis*, vol. 3, no. 1, pp. 29–43, 1996. [Online]. Available: https://www.sciencedirect.com/science/article/pii/1350630795000313

[54] V. Nagarajan, Y. Chen, Q. Wang, and T. Ma, "Numerical analysis of steady state and transient analysis of high temperature ceramic plate-fin heat exchanger," *Nuclear Engineering and Design*, vol. 277, pp. 76–94, 2014.

[55] W. Huang, H. Zhao, and P. F. Peterson, "Multi-Scale Stress Analysis for Compact Plate-Type Heat Exchangers," in *Proceedings of the 2006 international congress on advances in nuclear power plants - ICAPP'06*, American Nuclear Society, Ed., 2006.

[56] L. Mörl and H. Gelbe, "Konstruktionselemente von Apparaten und Rohrleitungen," in *Dubbel*, K.-H. Grote, B. Bender, and D. Göhlich, Eds. Berlin, Heidelberg: Springer Berlin Heidelberg, 2018, pp. 752–773.

[57] H. Gonser, “Untersuchungen zum Einsatz von Warmetauschern in zivilen Turboflugtriebwerken,” Dissertation, Universität Stuttgart, Stuttgart, 2008. [Online]. Available: https://elib.uni-stuttgart.de/bitstream/11682/3801/1/diss_gonser.pdf

[58] S. Emam and W. Lacarbonara, “A review on buckling and postbuckling of thin elastic beams,” *European Journal of Mechanics - A/Solids*, vol. 92, 2022.

[59] F. M. H. Aliabadi, *Comprehensive Structural Integrity*, 2nd ed. San Diego: Elsevier Science & Technology, 2023. [Online]. Available: https://ebookcentral.proquest.com/lib/kxp/detail.action?docID=7238688

[60] A. Fissolo, S. Amiable, L. Vincent, S. Chapuliot, A. Constantinescu, and J. M. Stelmaszyk, “Thermal Fatigue Appears to be More Damaging Than Uniaxial Isothermal Fatigue: A Complete Analysis of the Results Obtained on the CEA Thermal Fatigue Device Splash,” in *Volume 3: Design and Analysis*. ASMEDC, 2006, pp. 535–544.

[61] R. Hölzl, T. Hecht, and P. Freko, “Damage Analysis and Fatigue Evaluation of an Aluminium Brazed Plate Fin Heat Exchanger,” in *Volume 3: Design and Analysis*. American Society of Mechanical Engineers, 2014.

[62] Y. Mizokami, T. Igari, F. Kawashima, N. Sakakibara, M. Tanihira, T. Yuhara, and T. Hiroe, “Development of structural design procedure of plate-fin heat exchanger for HTGR,” *Nuclear Engineering and Design*, vol. 255, pp. 248–262, 2013.

[63] L. Zhang, B. Jiang, P. Zhang, H. Yan, X. Xu, R. Liu, J. Tang, and C. Ren, “Methods for fatigue-life estimation: A review of the current status and future trends,” *Nanotechnology and Precision Engineering*, vol. 6, no. 2, 2023.

[64] G. T. Yahr, “Fatigue Design Curves for 6061-T6 Aluminum,” *Journal of Pressure Vessel Technology*, vol. 119, no. 2, pp. 211–215, 1997.

[65] M. E. Kassner, "Fundamentals of Creep in Materials," in *Fundamentals of Creep in Metals and Alloys.* Elsevier, 2015, pp. 1–6.

[66] Jun-Shan Zhang, "Prediction of Creep-Fatigue Life," in *High Temperature Deformation and Fracture of Materials*, Woodhead Publishing, Ed. Elsevier, 2010, pp. 319–329.

[67] J. K. Wright, L. J. Carroll, T.-L. Sham, N. J. Lybeck, and R. N. Wright, "Determination of the Creep-Fatigue Interaction Diagram for Alloy 617," in *Volume 5: High-Pressure Technology; Rudy Scavuzzo Student Paper Symposium and 24th Annual Student Paper Competition; ASME Nondestructive Evaluation, Diagnosis and Prognosis Division (NDPD); Electric Power Research Institute (EPRI) Creep Fatigue Workshop.* American Society of Mechanical Engineers, 2016.

[68] M. F. Saffiudeen, A. Syed, and F. T. Mohammed, "Failure Analysis of Heat Exchanger Using Eddy Current Testing (ECT)," *Journal of Failure Analysis and Prevention*, vol. 23, no. 5, pp. 1898–1906, 2023.

[69] S. Kim, H. Yu, K. Nam, and B. Choi, "Failure analysis and structural improvement for cracked circular finned tube," *Engineering Failure Analysis*, vol. 92, pp. 95–106, 2018.

[70] C. Azevedo and G. S. Alves, "Failure analysis of a heat-exchanger serpentine," *Engineering Failure Analysis*, vol. 12, no. 2, pp. 193–200, 2005.

[71] Z. Zhu, M. Wang, H. Zhang, X. Zhang, T. Yu, and Z. Wu, "A Finite Element Model to Simulate Defect Formation during Friction Stir Welding," *Metals*, vol. 7, no. 7, p. 256, 2017.

[72] MatWeb, "Aluminium 6061-T6; 6061-T651: Material Property Data," 2024. [Online]. Available: https://www.matweb.com/search/datasheet.aspx?MatGUID=b8d536e0b9b54bd7b69e4124d8f1d20a

[73] R. Rennert, Ed., *Rechnerischer Festigkeitsnachweis für Maschinenbauteile aus Stahl, Eisenguss- und Aluminiumwerkstoffen*, 7th ed., ser. FKM-Richtlinie. Frankfurt am Main: VDMA Verlag, 2020.

[74] Special Metals Corporation, "Inconel 625 Specification." [Online]. Available: https://www.specialmetals.com/documents/technical-bulletins/inconel/inconel-alloy-625.pdf

[75] VDM Metals, "VDM Alloy 625: Nicrofer 6020 hMo." [Online]. Available: https://www.vdm-metals.com/fileadmin/user_upload/Downloads/Data_Sheets/Data_Sheet_VDM_Alloy_625.pdf

[76] S. Bell, M. de Bruyn, T. Steinberg, and G. Will, "Corrosion resistance of 625 nickel superalloy exposed to isothermal and thermal cycling conditions in a chloride/carbonate salt," *Solar Energy*, vol. 249, pp. 278–287, 2023.

[77] S. Khan and K. G. Manjunatha, "Comparison of Pitting Corrosive Behaviour of as Casted and Heat Treated Al6061-SiC Metal Matrix Composite in Various Medium by Weight Loss Method," *Materials Today: Proceedings*, vol. 5, no. 10, pp. 22 517–22 525, 2018.

[78] D. Luo, F. Li, and G. Xing, "Corrosion resistance of 6061-T6 aluminium alloy and its feasibility of near-surface reinforcements in concrete structure," *REVIEWS ON ADVANCED MATERIALS SCIENCE*, vol. 61, no. 1, pp. 638–653, 2022.

[79] S. M. Mohammed and S. M. Mahdi, "Corrosion behavior of aluminum alloys 2024 and 6061 in rainwater," *Journal of Physics: Conference Series*, vol. 1973, no. 1, 2021.

[80] L. Jain, "Characterization of the exhaust gas condensate pH values of gasoline engines," Master Thesis, Massachusetts Institute of Technology, Boston, 2016. [Online]. Available: https://dspace.mit.edu/bitstream/handle/1721.1/106780/970344503-MIT.pdf?sequence=1&isAllowed=y

[81] N. Eliaz, G. Shemesh, and R. M. Latanision, “Hot corrosion in gas turbine components,” *Engineering Failure Analysis*, vol. 9, no. 1, pp. 31–43, 2002.

[82] I.-S. Forest, “The corrosion resistance of nickel-containing alloys in sulfuric acid and related compounds,” *INCO The International Nickel Company*, vol. 1, pp. 51–82, 1983.

[83] P. Ganesan, C.M. Renteria, and J. R. Crum, “Versatile Corrosion Resistance of INCONEL alloy 625 in Various Aqueous and Chemical Processing Environments,” in *Superalloys 718, 625 and various derivatives*. Warrendale, Pa.: TMS, 1991, pp. 663–680. [Online]. Available: https://www.tms.org/superalloys/10.7449/1991/Superalloys_1991_663_680.pdf

[84] L. Li, L. Li, G. Zhang, H. Xue, M. Cui, W. Wang, and D. Liu, “Hot Corrosion Behavior of Inconel 625 in Na2SO4 and V2O5 Molten Salt System,” *Metals*, vol. 13, no. 6, 2023.

[85] M. Oksa, J. Metsäjoki, and J. Kärki, “Thermal Spray Coatings for High-Temperature Corrosion Protection in Biomass Co-Fired Boilers,” *Journal of Thermal Spray Technology*, 2014.

[86] H. Sun and J. Liu, “Hot corrosion of Fe and Ni-based alloys in Wase-to-energy environment at 850 °C,” *Engineering Failure Analysis*, vol. 133, 2022.

[87] Y.-J. Ma, Y. Ding, J.-J. Liu, Y.-B. Gao, and D. Zhang, “Corrosion Behavior of Inconel 625 Alloy in Na2SO4–K2SO4 at High Temperature,” in *Physics and Engineering of Metallic Materials*, ser. Springer Proceedings in Physics, Y. Han, Ed. Singapore: Springer Singapore, 2019, vol. 217, pp. 153–166.

[88] Z. Ma, D. Xu, S. Guo, Y. Wang, S. Wang, Z. Jing, and Y. Guo, “Corrosion Properties and Mechanisms of Austenitic Stainless Steels and Ni-Base Alloys in Supercritical Water Containing Phosphate, Sulfate, Chloride and Oxygen,” *Oxidation of Metals*, vol. 90, no. 5-6, pp. 599–616, 2018.

[89] W. C. Young and R. G. Budynas, *Roark's formulas for stress and strain*, 7th ed. New York, NY: McGraw-Hill, 2002.

[90] N. Buannic, P. Cartraud, and T. Quesnel, "Homogenization of corrugated core sandwich panels," *Composite Structures*, vol. 59, no. 3, pp. 299–312, 2003.

[91] C. Affolter, G. Thorwarth, A. Arabi-Hashemi, U. Müller, and B. Weisse, "Ductile Compressive Behavior of Biomedical Alloys," *Metals*, vol. 10, no. 1, p. 60, 2020.

[92] H. B. Dinh, J. M. Yu, K. B. Yoon, C. Park, and S. Ryu, "Plugging criteria for thinned high-pressure feedwater heater tubes considering pressure and thermal loading," *Journal of Mechanical Science and Technology*, vol. 32, no. 12, pp. 5637–5645, 2018.

[93] Deutsches Institut für Normung, "Unbefeuerte Druckbehälter – Teil 8: Zusätzliche Anforderungen an Druckbehälter aus Aluminium und Aluminiumlegierungen; Deutsche Fassung EN 13445-8:2021," 2021.

[94] ——, "Metallische industrielle Rohrleitungen - Teil 3: Konstruktion und Berechnung; Deutsche Fassung EN 13480-3:2017," 2017.

[95] K.-H. Raunig, "Die zerstörungsfreie Prüfung in Zusammenhang mit der Anwendung der Druckgeräterichtlinie (97/23/EG)," in *Jahrestagung 2004 Zerströrungsfreie Materialprüfung*, ser. Berichtsband / Deutsche Gesellschaft für Zerstörungsfreie Prüfung e. V. Berlin: DGZfP, 2004. [Online]. Available: https://www.ndt.net/search/docs.php3?id=2628

[96] A. Cunha, Y. Yanik, C. Olivieri, and S. Da Silva, "Tresca vs. von Mises: Which failure criterion is more conservative in a probabilistic context?" *Journal of Applied Mechanics*, pp. 1–8, 2023.

[97] D. Gross, W. Hauger, J. Schröder, and W. A. Wall, *Technische Mechanik*, 15th ed. Berlin: Springer Vieweg, 2024. [Online]. Available: https://link.springer.com/978-3-662-68422-1

[98] C. Spura, B. Fleischer, H. Wittel, and D. Jannasch, *Roloff/Matek Maschinenelemente*, 26th ed. Wiesbaden: Springer Vieweg, 2023. [Online]. Available: https://link.springer.com/978-3-658-40913-5

[99] R. K. Giridhar, P. V. Ramaiah, G. Krishnaiah, and S. G. Barad, "Gas Turbine Blade Damper Optimization Methodology," *Advances in Acoustics and Vibration*, vol. 2012, pp. 1–13, 2012.

[100] J. Rösler, H. Harders, and M. Bäker, *Mechanisches Verhalten der Werkstoffe*, 5th ed., ser. Lehrbuch. Wiesbaden: Springer Vieweg, 2016. [Online]. Available: http://www.springer.com/de/book/978-3-658-13794-6

[101] A. Pavan, R. L. Narayan, M. Swamy, K. Singh, and U. Ramamurty, "Stress rupture embrittlement in cast Ni-based superalloy 625," *Materials Science and Engineering: A*, vol. 793, 2020.

[102] Abu Dhabi National Oil Company, "SHELL AND TUBE HEAT EXCHANGER SPECIFICATION."

[103] H. Ma, C. Hou, R. Yang, C. Li, B. Ma, J. Ren, and Y. Liu, "The influence of structure parameters on stress of plate-fin structures in LNG heat exchanger," *Journal of Natural Gas Science and Engineering*, vol. 34, pp. 85–99, 2016.

[104] H. X. Cao, X. Q. Qiu, and W. C. Jiang, "Analysis of Thermal Stresses in 304 Stainless Steel Plate-Fin Structure," *Advanced Materials Research*, vol. 681, pp. 286–290, 2013.

[105] Y. Rui, A. Subic, M. Takla, C. H. Wang, A. Niehoff, N. Hamann, and G. P. Brueggemann, "Biomimetic Design of Lightweight Vehicle Structures Based on Animal Bone Properties," *Advanced Materials Research*, vol. 633, pp. 3–14, 2013.

[106] S. P. Timošenko and J. M. Gere, *Theory of elastic stability*, 2nd ed. Mineola, New York: Dover Publications, 2009. [Online]. Available: http://www.loc.gov/catdir/enhancements/fy0905/2009003597-d.html

[107] K. Krisdiyanto, R. K. Adi, S. Sudarisman, and S. B. Hamdan, “An analysis of tube thickness effect on shell and tube heat exchanger,” *Eastern-European Journal of Enterprise Technologies*, vol. 1, no. 8 (109), pp. 25–35, 2021.

[108] M. M. Patel, “Shell & tube heat exchangers: Thermal design and optimization,” 2023. [Online]. Available: https://heat-exchanger-world.com/shell-tube-heat-exchangers-thermal-design-and-optimization/